ANALYSIS OF TIRE-PAVEMENT INTERACTION AND PAVEMENT RESPONSES USING A DECOUPLED MODELING APPROACH

BY

HAO WANG

DISSERTATION

Submitted in partial fulfillment of the requirements
for the degree of Doctor of Philosophy in Civil Engineering
in the Graduate College of the
University of Illinois at Urbana-Champaign 2011

Urbana, Illinois

Doctoral Committee:

Professor Imad L. Al-Qadi, Chair
Professor Erol Tutumluer
Professor William G. Buttlar
Professor Eyad Masad, Texas A&M University
Assistant Professor Ilinca Stanciulescu, Rice University

ABSTRACT

The proper understanding of tire-pavement interaction is important for the accurate analysis of load-induced stresses and strains in the pavement structure. This dissertation focuses on the analysis of the mechanism of tire-pavement interaction and the effect of tire-pavement interaction on pavement responses using a decoupled modeling approach. First, an air-inflated three-dimensional (3-D) finite element (FE) tire model was built and the interaction between a tire and a non-deformable pavement surface was simulated. The tire is modeled as a composite structure including rubber and reinforcement. The steady-state tire rolling process was simulated using an Arbitrary Lagrangian Eulerian (ALE) formulation. The developed tire-pavement interaction model is used to evaluate the mechanism of load distribution at the tire-pavement interface under various tire loading and rolling conditions. After that, a 3-D FE model of flexible pavement was developed to analyze pavement responses under various loading scenarios. This model utilizes the implicit dynamic analysis, simulates vehicular loading as a continuous moving load, and incorporates 3-D contact stresses at the tire-pavement interface. In the pavement model, the asphalt layer is modeled as a linear viscoelastic material and the granular base layer is modeled as a nonlinear anisotropic material. The FE pavement model was used to analyze critical pavement responses in thin and thick asphalt pavements considering different damage mechanisms.

This dissertation concludes that knowledge of tire-pavement contact stress distributions is critical for pavement response prediction. Most importantly, the non-uniform distribution of vertical contact stresses and the localized tangential contact stresses should be considered in the mechanistic-empirical pavement design. The contact stress distributions at the tire-pavement interface are affected by vehicle loading (wheel load and tire inflation pressure), tire configuration (dual-tire assembly and wide-base tire), vehicle maneuvering (braking/acceleration and cornering), and pavement surface friction. Therefore, pavement damage should be quantified using accurate loading inputs that are represented by realistic tire-pavement contact stress distributions.

Thin and thick asphalt pavements fail in different ways. Multiple distress modes could occur in thin asphalt pavements, including bottom-up fatigue cracking and rutting in each pavement layer. It was found that the interaction between the viscoelastic asphalt layer and the nonlinear anisotropic granular base layer plays an important role for the stress distribution within a thin asphalt pavement structure under moving vehicular loading. In thick asphalt pavements, near-surface cracking is a critical failure mechanism, which is affected by the localized stress states and pavement structure characteristics. Particularly, the effect of shear stress on the formation of near-surface cracking at multi-axial stress states is important and can not be neglected, especially at high temperatures.

ACKNOWLEDGEMENT

I would like to express my most sincere gratitude to my advisor, Professor Imad Al-Qadi, for his continuous guidance and support during my entire Ph.D. study. I am inspired by the high standards that he sets for himself and those around him, his attention to detail, and his dedication to the profession. I have thoroughly enjoyed working with him and I have learned a lot.

I am also grateful to the members of my graduate committee: Professor Erol Tutumluer, Professor William Buttlar, Professor Eyad Masad, and Professor Ilinca Stanciulescu for their encouragement and valuable suggestions during the course of my study.

I want to thank my colleagues and friends at the Advanced Transportation Research and Engineering Laboratory (ATREL) for their friendly and continuous support during my study. They will always be remembered for the wonderful times we spent together during my stay at the University of Illinois at Urbana-Champaign.

Finally, I am deeply indebted to my parents and family for their endless patience, comprehension, and love, and especially acknowledge the endless support and encouragement of my wife, Ming Zhou.

TABLE OF CONTENTS

CHAPTER 1 INTRODUCTION

1.1 Introduction

Heavy trucks can cause rapid deterioration of flexible pavements. The exact impact of truck loading on a pavement structure is controlled by the magnitude and frequency of the applied wheel loads. These loads are transferred to the pavement structure through truck tires. Thus, a proper understanding of the interaction between tires and pavements is required to analyze the resulting stresses and strains in the pavement.

Real traffic consists of vehicles with different axle configurations, wheel loads, and tire inflation pressures. Two main approaches are currently available to account for the traffic load effect on pavement. The first approach converts the traffic axle configuration and wheel loads into equivalent single axle loads (ESALs) using the load equivalence factors (LEFs). The LEFs can be derived from field tests, such as the American Association of State Highway Officials *(*AASHO) road test, or the mechanistic-empirical analysis of pavement damage. The second approach, as defined in the recent Mechanistic-Empirical Pavement Design Guide (MEPDG), considers actual axle load spectra in the calculation of pavement responses and prediction of pavement performance (ARA 2004). However, in both approaches, the tire loading is usually modeled as having a uniform contact stress equal to tire inflation pressure within an assumed circular contact area. As the wheel load increases, the contact stress is assumed to increase uniformly while the contact area remains constant, or the contact stress is assumed to remain constant while the contact area is proportionally increased.

Experimental measurements have documented that when a tire load is applied on a pavement surface, three contact stress components (vertical, transverse, and longitudinal) are generated under each tire rib. These contact stresses do not change uniformly throughout the tire imprint area as the load or tire inflation pressure changes (De Beer et al. 1997). In addition, tire-pavement contact stresses may also change during vehicle maneuvering, such as acceleration/traction, deceleration/braking, and cornering. Therefore, traditional methodologies can not differentiate contact stress distributions at the tire-pavement interface under various tire loading and rolling conditions. The magnitude of error in predicting pavement responses using the conventional loading assumption may be minimal when considering the responses at deeper pavement depth. On the other hand, the resulting errors could be very high when considering the responses in thin asphalt pavements or the responses at near-surface of thick asphalt pavements.

1.2 Problem Statement

Recently, researchers have begun analyzing pavement responses using measured three-dimensional (3-D) tire-pavement contact stresses (Al-Qadi and Yoo 2007; Al-Qadi et al. 2008). However, the interaction mechanism between tires and pavements is still not clear. Limited data on tire-pavement contact stresses under various tire loading conditions are available. An efficient method to account for tire contact stress variability in practical pavement design and analysis procedure has yet to be developed. Thus, an urgent need exists to investigate the contact stress distribution at the tire-pavement interface and its impact on asphalt pavement responses and damage.

The typical pavement structure of a low- or medium-volume road consists of a relatively thin asphalt surface layer and an unbound base layer constructed on subgrade. The conventional pavement design method treats the granular base layer as linear elastic material with a constant Poisson’s ratio. However, the nonlinear anisotropic behavior of the unbound base layer has been well documented (Tutumluer and Thompson 1997). The modulus of the base layer varies depending on the stress transmitted into the base layer and the modulus is different in vertical and horizontal directions. Hence, it is necessary to consider the anisotropic stress-dependent modulus of the base layer when evaluating the effect of various tire loading conditions on thin asphalt pavement responses.

Thick asphalt pavements (including full-depth pavements) are usually designed for major roads or interstate highways to prevent fatigue cracking due to high-volume traffic. However, the premature failure at the pavement near-surface is more concerned with thick asphalt pavements or overlays. The near-surface failure could be surface- or near-surface-initiated wheel-path cracking or instable rutting within the upper asphalt layer. It is a complex phenomenon which is affected by various factors such as vehicular loading, asphalt mixture characteristics, pavement structure design, and environmental conditions. In particular, the truck tire causes a complex 3-D stress state close to the pavement surface. Therefore, rather than only considering one-dimensional tensile or shear stresses, the multi-axial stress state (normal and shear) needs to be considered together when analyzing the material failure potential at the pavement near-surface.

1.3 Objective and Approach

The main objective of this research is to investigate the contact stress distribution at the tire-pavement interface and its impact on flexible pavement responses. In order to achieve this objective, the following research tasks are conducted:

1) Develop a tire-pavement interaction model to predict the contact stress distributions at the tire-pavement interface under various tire loading and rolling conditions. The model is validated through the comparison between the predicted and measured tire contact stresses.

2) Build a 3-D finite element (FE) model of flexible pavement structure under vehicular loading. The model incorporates realistic tire loading conditions and appropriate material characterizations for each pavement layer. The model results are compared to field response measurements obtained from accelerated pavement testing (APT).

3) Analyze critical pavement responses of thin asphalt pavements under various tire loading and rolling conditions, utilizing cross-anisotropic stress-dependent modulus for the granular base layer.

4) Analyze the mechanisms of near-surface failure in thick asphalt pavements under multi-axial stress states. The factors affecting the near-surface failure potential are investigated.

To take into account the complex nature of tire-pavement interaction and achieve better computation efficiency and stability, the effects of tire-pavement interaction on pavement responses are studied using a decoupled approach. First, a rolling tire model on a non-deformable pavement surface is developed to predict the contact stress distributions at the tire-pavement interface. This assumption is considered reasonable because the tire deformation is much greater than the pavement deflection when wheel load is applied on the tire and transmitted to the pavement surface. Second, the pavement responses under the tire contact stresses are calculated and the effects of tire-pavement interaction on different pavement damage mechanisms are analyzed. Figure 1.1 shows a flowchart of the analysis approach.

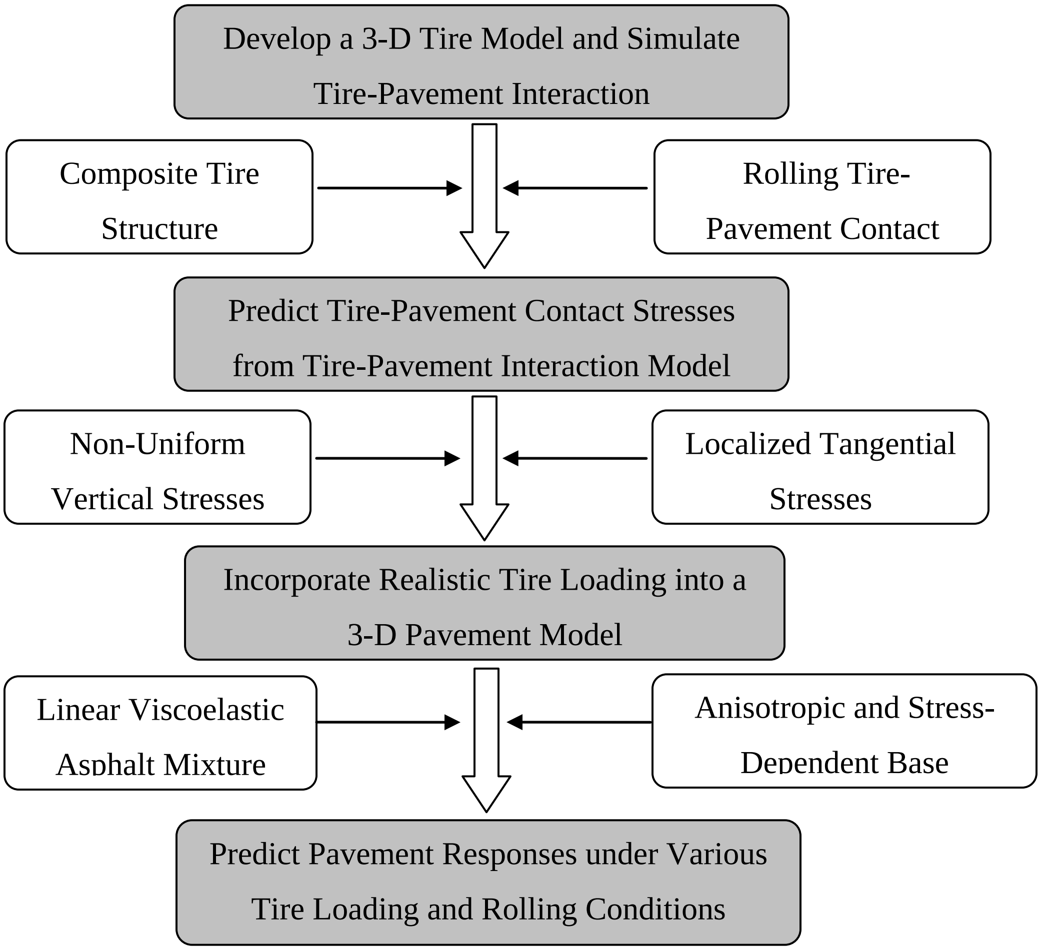

Figure 1.1 Flowchart of analysis approach

1.4 Scope

This dissertation is divided into seven chapters. The first chapter introduces the problem statement, objective, and methodology. The second chapter summarizes previous research on mechanistic analysis of pavement responses, pavement failure mechanisms, and tire-pavement interaction. The third chapter describes the developed tire-pavement interaction model and analyzes the contact stress distributions at various tire loading and rolling conditions. The fourth chapter describes the developed 3-D FE pavement model, incorporating realistic tire loading conditions and appropriate material characterizations. The fifth chapter presents an analysis of thin asphalt pavement responses utilizing nonlinear anisotropic modulus of the base layer. The sixth chapter analyzes the near-surface failure potential of thick asphalt pavements under multi-axial stress states. The final chapter presents analysis findings, conclusions and future study recommendations.

CHAPTER 2 RESEARCH BACKGROUND

2.1 Mechanistic Analysis of Pavement Responses

2.1.1 Multilayer Elastic Theory versus Finite Element Method

The layered elastic theory is the tool used most often to calculate flexible pavement responses to truck loading since 1940s. This is mainly due to its simplicity. The major assumptions made in the layered elastic theory are as follows (Huang 1993):

- Each layer is assumed homogeneous, isotropic, and linear elastic;
- All materials are weightless (i.e., no inertia effect);
- Pavement systems are loaded statically over a uniform circular area;
- The subgrade is assumed to be a semi-infinite layer with a constant modulus;
- The compatibility of strains and stresses is assumed to be satisfied at all layer interfaces.

In 1943, Burmister developed a closed-form solution for a two-layered, linearly elastic, half-space problem, which was later extended to a three-layer system. Since then, and with advances in computer technology, the theory has been extended to deal with multilayer systems. Accordingly, a large number of computer programs have been developed, including BISAR, KENLAYER, ELSYM, EVERSTRESS, WESLEA, and JULEA (Huang 1993). Some of these computer programs introduced modifications to the original layered theory to cover viscoelastic material constitutive models (VESYS), to allow for horizontal loading (CIRCLY), and to adjust the bonding conditions at the layer interfaces (BISAR 3.0). However, these modifications are only accurate based upon the validity of other assumptions.

Two-Dimensional (2-D) FE models (axisymmetric or plain strain models) were the first successful examples of the application of the FE method in pavement analysis. The axisymmetric modeling approach assumes that the pavement system has constant material and geometric properties in horizontal planes, and the traffic loading is circular load applied on the pavement surface. The plain strain model assumes a zero strain in the z direction that is perpendicular to the xy plane of the model, when the long-bodied structure is subjected to line loads that act in the x and/or y directions and do not vary in the z direction. ILLI_PAVE is one of the most common software using an axisymmetric

FE model. In the ILLI_PAVE software, the modulus can be stress-dependent and the Mohr-Coulomb failure criterion is used for granular materials and fine-grained soils (Thompson and Elliott 1985).

With the advance of fast computers and algorithmic improvements, the use of 3-D FE analysis has become widespread in pavement structural analysis (Zaghloul and White 1993). In comparison to the relatively simple layered elastic theory or 2-D axisymmetric model, the 3-D FE model can consider many analysis scenarios, such as non-uniform tire-pavement contact stress, irregular tire imprint area, discontinuities in pavement (cracks or joints), viscoelastic and nonlinear material properties, infinite foundation, material damping, quasi-static or dynamic analysis, crack propagation, coupled temperature effect, bonded or de-bonded interface, and so forth.

2.1.2 Viscoelastic Pavement Responses under Moving Load

It is well known that the mechanical response of asphalt pavement under moving vehicular loading is dependent on time, loading rate, and the entire loading history, due to the viscoelastic nature of asphalt material. A number of studies since the early 1970s have evaluated the viscoelastic responses of flexible pavements under moving loads using different approaches.

Analytical models of viscoelastic pavement structure under a moving load vary in complexity according to the structure analyzed (finite beam, infinite plate on Winkler foundation, or multi-layers) and the loading (constant, harmonic, or random). The solutions vary from analytical closed-form solutions using the corresponding principle to semi-analytical solutions using numerical techniques. However, for complex geometries and loading conditions, it is often impossible to get the closed-form solution from the inverse transform.

Chou and Larew (1969) studied the multilayered pavement responses to a moving point load based on linear viscoelastic theory. Elliot and Moavenzadeh (1971) conducted a similar study for a circular load using an approximate approach. Huang (1973) solved the viscoelastic pavement problem by using the approximate collocation method and assuming a Dirichlet series for viscoelastic modulus. The influence of moving load was assumed equivalent to that of a stationary load, with changing magnitudes depending on time. A computer program (SAPSI) was developed by Sousa and coworkers (Sousa et al., 1988) and used to compute the dynamic responses of a viscoelastic layered structure subjected to a circular load. The total response from the moving load was obtained by the superposition of all responses to stationary loads at a given time.

Hardy and Cebon (1993) and Papagiannakis et al. (1996) used an influence function approach to study pavement responses to a moving load at constant speed if the pavement response under an impulsive loading was known *a priori*. Hopman (1996) developed the viscoelastic multilayer computer program (VEROAD) to calculate pavement responses subject to moving circular loads by using the correspondence principle. In this model, Burger's model was used to describe the viscoelastic behavior of the asphalt material. Siddharthan et al. (1998) used a continuum, finite-layer model (3D-MOVE) to evaluate pavement responses under a moving surface load. The load was decomposed into multiple single harmonic pressure distributions and the viscoelastic layer properties are defined by the dynamic shear modulus and the internal damping ratio. Chambot et al. (2005) developed the ViscoRoute software based on Duhamel's semi-analytical multilayer model to calculate pavement responses under a moving load within rectangular or elliptic contact area. The viscoelastic behavior of the asphalt material was defined through the Huet-Sayegh model that consists of two springs for elastic modulus and two parabolic dampers for delayed response.

Numerical methods, such as FEM and boundary element method (BEM), have been used to simulate pavement responses under moving vehicular loads. Pan et al. (1995) coupled BEM with the FEM approach by modeling the elastic pavement using FE and the underlying elastoplastic half-space using boundary elements. Yang and Hung (2001) used 2.5-D finite/infinite elements to calculate the steady state responses of pavement under a moving load. Gonz´alez and Abascal (2004) used BEM approach and implemented the correspondence principle to convert a viscoelastic problem to an elastic problem. Shen and Kirkner (2001) developed a 3-D FE model based on moving coordinate system to predict pavement residual deformation subject to moving loads. Recently, Al-Qadi and co-workers, as well as other researchers, have used general-purpose FE software programs to analyze viscoelastic pavement responses. In these programs, relaxation moduli are usually required as the input parameters (Elseifi et al. 2006; Yoo and Al-Qadi 2008; Kim et al. 2009).

Although the 3-D FE model can be a complex and costly analysis tool, it provides the needed versatility and flexibility to accurately simulate the nonlinear material behavior, the complex layer interface condition, and the non-uniform distribution of tire loading. Compared to BEM/FEM, the main advantage of analytical/semi-analytical methods is the relatively short computational time. However, in the analytical/semi-analytical methods, material linearity, isotropy, and no-slip interface between layers are usually assumed in order to solve the equations.

2.1.3 Nonlinear Cross-Anisotropic Aggregate Behavior

Previous research studies have found that unbound aggregate layers exhibit stress- and direction- (anisotropic) dependent behavior due to the nature of granular medium and the orientation of aggregate (Uzan 1992; Tutumluer 1995). The orientation of aggregate is controlled by its shape, compaction methods, and loading conditions. A special type of anisotropy, known as cross-anisotropy, is commonly observed in pavement granular base layer due to compaction and the applied wheel loading in the vertical direction.

Tutumluer and Thompson (1997) found that for a certain set of aggregate the horizontal stiffness in the granular layer is only 3 to 21% of the vertical stiffness, and the shear stiffness is 18 to 35% of the vertical stiffness. The nonlinear-anisotropic approach is shown to account effectively for the dilative behavior observed under the wheel load and the effects of compaction-induced residual stresses. The research project conducted at the International Center for Aggregate Research (ICAR) developed a resilient modulus testing protocol and a Systems Identification (SID) approach to determine the stress sensitivity and cross-anisotropy of granular material (Adu-Osei et al. 2001).

Tutumluer and Seyhan (1999) used an advanced triaxial testing machine, referred as UI-FastCell, to simulate dynamic stresses on the sample and study the effects of anisotropic, stress-dependent aggregate behavior. Further, Seyhan et al. (2005) presented a new methodology for determining cross-anisotropic aggregate base behavior considering effects of moving wheel loading. The proposed testing protocol requires conducting repeated load triaxial tests using variable confining pressure (VCP), also known as the stress path tests. They found that higher vertical moduli than the horizontal values and higher out-of-plane Poisson’s ratios than the in-plane values were typically obtained at all stress states. In addition, the vertical moduli obtained from the negative stress path tests were often found lower than those from the positive stress path tests, whereas the negative stress path tests gave the highest Poisson’s ratios for both the in-plane and the out-of-plane Poisson’s ratios.

As the pavement design method shifts from an empirical procedure to a mechanistic-empirical (M-E) method, it is critical to consider the nonlinear anisotropic granular behavior in the pavement response model. Tutumluer et al. (2003) and Park and Lytton (2004) found that the nonlinear anisotropic modulus of the unbound base layer significantly affects the stress distributions in the base layer and reduces the horizontal tension in the bottom half of the base layer. Oh et al. (2006) and Masad et al. (2006) showed that the FE predictions based on anisotropic models for the unbound base and sub-base layers provide better agreements with field performance measurements. Kwon et al. (2009) used an axisymmetric FE program (GT_PAVE) and found that the model predictions using the nonlinear and anisotropic characterizations of the granular base layer better capture the magnitudes and the trend in the measured response data for both geogrid-reinforced and control low-volume flexible pavement test sections.

2.1.4 Pavement Dynamic Analysis

It is documented that structural dynamic responses or dynamic amplifications depend on the ratio of external loading frequency to natural frequency of the structure. Although a few researchers have studied the natural frequency of pavement structure, the range of natural frequency was found to be 6-14 Hz for flexible pavements and 20-58 Hz for rigid pavements (Darestani et al. 2006; Uddin and Garza 2003). Gillespie et al. (1993) found that truck loading frequency was about 4.6Hz at a speed of 58km/h and 6.5Hz at 82km/h, respectively. Thus, a dynamic analysis may be needed to determine pavement responses under some loading conditions.

Researchers have used two analytical approaches to analyze transient pavement structure response under vehicular loading. The first is using the ordinary differential equations (ODE) developed from Newton’s second law of motion with parameters characterizing the stiffness, damping, and mass of the pavement materials (Chopra 2001). The displacements are used together with the constitutive equations to calculate the stresses and strains in the pavement structure. The second approach is based on the governing equations for elastodynamic wave equations (Mamlouk and Davies 1984). These equations are used to develop the Helmholtz partial differential equation (PDE), which is the governing equation for steady-state (harmonic) elastodynamics. In this approach, usually, material linearity, isotropy, and no-slip between layers are assumed and the equation can be solved with analytical and numerical techniques.

Mamlouk and Davies (1984) concluded that dynamic deflections under falling weight deflectometer (FWD) tests were greater than the corresponding static displacements at some locations due to local amplifications in the layered pavement structure. Lourens (1992) showed that the stresses and deflections in the pavement differed substantially between static and dynamic loads. They indicated that the magnitude of pavement stress after the load passing is dependent on the loading speed. Hardy and Cebon (1994) found that the effects of loading frequency on pavement strains are relatively minor compared with the effect of loading speed. Zaghloul and White (1993) studied the dynamic responses of flexible pavements and found close agreements between the results from ABAQUS and field measurements at three different speeds.

Siddharthan et al. (1998) concluded that the dynamic effects of moving loads on pavement strain responses are important and should not be ignored. Jooster and Lourens (1998) found that the effect of transient pavement analysis is equally important as the effect of non-uniform tire pressure and viscoelastic material behavior. The relative differences between the responses from the static and dynamic models depend on the evaluation position and material stiffness. Sadd et al. (2005) analyzed the dynamic pavement response using an elastoplastic base and subgrade properties, and found that the deflection under the dynamic load condition is less than its corresponding value obtained from the static analysis. They concluded that this result was expected, since in the dynamic analysis, inertial, dissipative, and internal forces absorbed the work done by externally applied forces. Yoo and Al-Qadi (2007) found that compared to quasi-static analysis, the dynamic transient analysis induces greater strain responses and residual strains after load passing.

2.1.5 Effect of Tire Contact Stresses on Pavement Responses

Research has shown that the assumed distribution of tire-pavement contact stresses significantly affects pavement responses. Most researchers analyzed the effect of contact stress distributions on pavement responses using an elastic approach. Prozzi and Luo (2005) found that the tensile strains in the asphalt layer under actual contact stresses were quite different from those under uniform contact stresses, depending on the combination of load and tire inflation pressure. Similarly, Machemehl et al. (2005) reported that the conventional uniform load assumption underestimated pavement responses at low tire inflation pressures and overestimated pavement responses at high tire pressures. De Beer et al. (2002) observed that pavement responses of thin flexible pavements were sensitive to vertical load shape and distribution. Soon et al. (2004) found that the tangential tire stresses caused tensile stresses outside the tire treads and their locations and magnitudes depended on the pavement thickness. Park et al. (2005) concluded that the predicted pavement fatigue life under the modified uniform load assumption (using measured tire contact area) showed better agreement with the predicted fatigue life under measured tire contact stresses, compared to the conventional uniform load assumption. Thyagarajan et al. (2009) also noted that the load-strain linear proportionality assumption in the MEPDG led to significant error in the predicted permanent deformation in the upper pavement layer.

Recently, some researchers analyzed the effect of contact stress distributions on viscoelastic pavement responses under moving loads. Siddharthan et al. (2002) showed that the difference between the responses computed with the uniform and non-uniform tire-pavement contact stress distributions is in the range of 6-30%. In this study, the effect of tangential contact stresses was not considered. Al-Qadi and Yoo (2007) reported that the effect of surface tangential contact stresses cannot be neglected because it may greatly affect pavement responses near the asphalt surface layer, and this effect diminishes as the depth increases. Wang and Al-Qadi (2009) found that the non-uniform distribution of vertical contact stresses and transverse tangential stresses induce outward shear flow from tire center and the shear strain concentration under tire ribs at the near-surface of thick asphalt pavements.

In summary, the literature review revealed important differences between the critical pavement responses when the assumptions of contact stress distributions change. The actual tire-pavement contact stresses induce greater or smaller pavement responses, compared to the conventional uniform contact stress distribution, depending on tire load and pressure, material stiffness, pavement thickness, and the type of response for comparison. These differences can only be accurately accounted for by utilizing a modeling approach that can simulate realistic contact stress distributions at the tire-pavement interface and predict viscoelastic pavement responses under moving vehicular loading.

2.1.6 Impact of New Generation of Wide-Base Tires

Various combinations of tire sizes and types are currently used on trucks. These truck tires have widths from 285mm to 495mm. Normally, tires with widths of less than 315mm are used as dual-tire assembly (except on steering axles) while those with widths of more than 315mm can be used as single tires. The nomenclature of tires usually includes three tire dimensions and types of tire in the form of AAA/BBXCC.C. The first number (AAA) is the tire width from wall-to-wall in mm or inch, the second number (BB) is the sidewall height given as a percentage of the tire width. The letter (X) indicates the type of tire (radial or bias ply). The third number (CC.C) is the tire rim diameter in inches. For example, a tire designation 455/55R22.5 is a radial tire (indicated with the "R"), with a wall-to-wall width of 455mm, a wall height of 250mm, and a rim diameter of 22.5in (571.5mm) (Figure 2.1).

Figure 2.1 Comparisons of different tire configurations (after Michelin product bulletin, 2006)

Traditionally, dual-tire assembly has been used to provide an adequate footprint to carry heavy loads and to distribute axle load over a large area on the pavement surface. Compared to the conventional dual-tire assembly, it is reported that wide-base tires can improve fuel efficiency, reduce emissions, increase payload, exhibit superior braking and comfort, and reduce tire repair, maintenance, and recycling cost (Al-Qadi and Elsefi 2007). However, the first generation of wide-base tires (385/65R22.5 and 425/65R22.5) produced in the early 1980s were found to cause 1.5 to 2.0 times more rut depth and 2.0 to 4.0 times more fatigue cracking than a dual-tire assembly when carrying the same load. This has led many transportation agencies to discourage their use.

The new generation of wide-base tires (445/50R22.5 and 455/55R22.5) came to market in the 2000's in order to reduce pavement damage and provide other safety and cost-saving advantages. The new generation of wide-base tires are 15 to 18% wider than the first generation and do not require high tire inflation pressure due to their special wall designs (Al-Qadi et al. 2005). Figure 2.2 shows the evolution of wide-base tire technology. Over the years, wide-base tires have become increasingly wider than their predecessors.

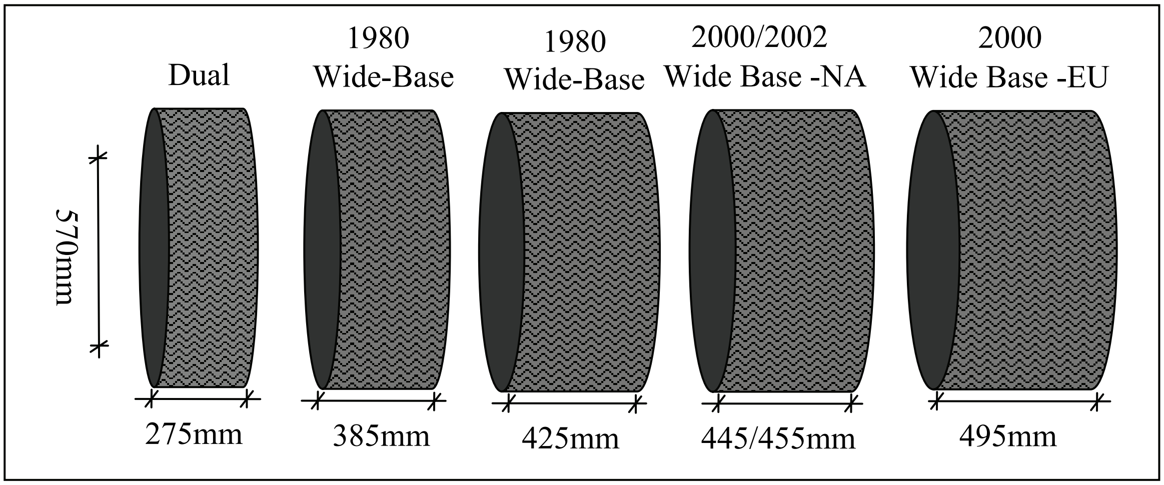

NA: Designed for North America, EU: Designed for the European Union

Figure 2.2 Evolution of wide-base tires (after Al-Qadi et al. 2005)

The impact of the new generation of wide-base tires on pavement damage was investigated by Al-Qadi and co-workers first in 2000. A comprehensive study was conducted to compare the pavement responses under wide-base tires and the dual-tire assembly on the heavily instrumented Virginia Smart Road. The study considered several pavement designs, truck speeds, loads, as well as tire pressure levels. Studies were also conducted by Al-Qadi and co-workers to investigate the pavement damage mechanisms induced by different tire configurations using a 3-D FE model. They concluded that the new wide-base 455 tire could cause greater or less pavement damage potential than the dual-tire assembly, depending on the pavement structure and failure mechanism (Al-Qadi et al. 2002; Al-Qadi et al. 2005, Yoo and Al-Qadi 2008; Al-Qadi and Wang 2009).

The COST Action 334 study conducted in Europe (2001) indicated that the new generation of wide-base tires would cause approximately the same primary rutting damage as a dual-tire assembly on primary roads and 44 to 52% more combined damage (20% primary rutting, 40% secondary rutting, and 40% fatigue cracking) on secondary roads. The COST study was mainly based on the field monitoring of pavement responses and performance. Pierre et al. (2003) conducted field measurements and found that the wide-base 455 tire caused more distortions at the pavement base in the spring but similar distortions in the summer, as compared to the dual tires. The wide-base 455 tire was also found to cause less primary rutting than the dual-tire assembly. Priest and Timm (2006) found from field measurements that the new wide-base 445 tire resulted in a similar pavement fatigue life as the standard dual-tire assembly (275/80R22.5); while the contrary conclusion was obtained when using the linear elastic analysis. This indicates that the layered elastic theory may not be appropriate to accurately compare pavement responses caused by different tire configurations. Greene et al. (2010) evaluated the pavement damage caused by various tire configurations using the accelerated pavement testing. The investigation revealed that the wide-base 455 tire performed as well as the dual tire assembly. The wide-base 445 tire was shown to create more rut damage on a dense-graded pavement surface and was predicted to create more bottom-up cracking than a dual-tire assembly.

The aforementioned studies indicate that the impact of wide-base tires on pavement damage depends on the pavement structures, pavement failure mechanisms considered, and environmental conditions. Generally, the damage caused by wide-base tires decreases as the tire width increases.

2.2 Pavement Failure Mechanisms

2.2.1 Conventional Asphalt Pavement Failures

Pavement failure may occur as a result of the environment, repeated traffic loading, deficient construction, and/or poor maintenance strategies. The two main load-associated distresses with flexible pavements are rutting and fatigue cracking.

Bottom-Up Fatigue Cracking

Fatigue cracking is caused by repeated relatively heavy load applications, usually lower than the strength of the paving material. Bottom-up fatigue cracking usually starts at the bottom of the asphalt layers of relatively thin flexible pavements (less than 150mm) or at the bottom of the individual asphalt layer if poor bonding conditions exist (Yoo and Al-Qadi 2008). The proposed AASHTO MEPDG determines the number of allowable load applications for fatigue cracking using Equation 2-1 (ARA 2004). This method utilizes the initial pavement response and ignores the evolution of strains with damage. However, the introduced error is considered acceptable within the empirical design framework.

$$N_f = 0.00432 \cdot k \cdot C \cdot (\frac{1}{\varepsilon_t})^{3.9492} \left(\frac{1}{E}\right)^{1.281} \qquad (2\text{-}1)$$

where N_f is the number of allowed load applications; E is the resilient modulus of asphalt mixture (in psi); ε_t is the tensile strain at the bottom of asphalt layer; C is a parameter related to asphalt mixture volumetric properties; and k is a parameter related to asphalt layer thickness.

Recently, more advanced fatigue models have been proposed based on viscoelastic continuum damage theory, dissipated energy concept, and viscoelastic fracture mechanics (Daniel and Kim 2002; Shen and Carpenter 2007; Kuai et al. 2009). These approaches are inherently more complex and offer more fundamental explanations than the empirical fatigue approach. Thus, they are applicable to predict fatigue damage growth in asphalt mixtures under a broader range of loading and environmental conditions and consider the effects of viscoelastic properties and fracture characteristics, such as binder aging and healing effects.

Primary Rutting

Rutting is the permanent deformation occurring in the pavement structure, including rutting in asphalt layers (primary rutting), rutting in unbound base layers, and subgrade (secondary) rutting. Primary rutting in asphalt layers includes two types of deformation: volume reduction caused by traffic densification, and permanent movement at a constant volume or dilation caused by shear flow. The general form of primary rutting models is usually derived from statistical analysis of the relationship between plastic and elastic compressive strains measured from repeated-load uniaxial/triaxial tests. The following transfer function is suggested by the AASHTO 2002 MEPDG, Equation 2-2 (ARA 2004).

$$\log(\frac{\varepsilon_p}{\varepsilon_r}) = -3.7498 + 0.4262\log(N) + 2.02755\log(T) \tag{2-2}$$

where ε_p is the accumulative permanent strain; ε_r is the recoverable strain; N is the allowed number of load repetitions corresponding to ε_p ; and T is the pavement temperature (°C).

Monismith et al. (1994) demonstrated that the accumulation of permanent deformation in the asphalt layer is very sensitive to the layer’s resistance to shape distortion (i.e., shear) and relatively insensitive to volume change. Their study indicates that the rutting in asphalt layers is caused principally by shear flow rather than volumetric densification; especially under loading of slow moving vehicles at high temperature. Deacon et al. (2002) and Monismith et al. (2006) correlated the rutting in asphalt layers to shear stresses and shear strains in the asphalt layer instead of compressive strains, as shown in Equation 2-3. This model was originally developed for Westrack mixes based on repeated simple shear test at constant height (RSST-CH).

$$\gamma = a \cdot \exp(b\tau_s)\gamma^e n^c \tag{2-3}$$

where γ is the permanent (inelastic) shear strain; γ^e is the elastic shear strain; τ_s is the corresponding shear stress; n is the number of axle load applications; and a , b , and c are experimentally determined coefficients.

Rutting in Unbound Base Layers

For a low-volume road with a thin asphalt layer, the permanent deformation of the granular base layer needs to be considered. The permanent deformation of the base layer can be caused by the granular material having insufficient stability due to heavy loading or poor drainage conditions. This may result in loss of particle-to-particle interlock forces and thus the bearing capacity (shear failure). This can ultimately result in permanent deformation by rutting or shoving at the pavement surface (Theyse et al. 1996). Figure 2.3 shows that a significant amount of permanent deformation in the base layer and subgrade caused shear failure in the asphalt layer after repeated loading on a thin-surfaced pavement section (Al-Qadi et al. 2007).

Figure 2.3 Observed shear failure in asphalt layer caused by rutting in granular base layer and subgrade (after Al-Qadi et al. 2007)

The MEPDG uses the following equation to predict rutting in the unbound layer. The parameters related to material properties can be estimated from the water content and the resilient modulus of the unbound layer.

$$\delta(N) = \beta_1 \left(\frac{\varepsilon_0}{\varepsilon_r} \right) e^{-\left(\frac{\rho}{N} \right)^{\beta}} \varepsilon_v h \qquad (2\text{-}4)$$

where $\delta(N)$ is the permanent deformation of the layer/sub-layer after N loading cycles; ε_0, β, and ρ are parameters related to material properties; ε_r is the resilient strain imposed at laboratory test to obtain material properties; ε_v is the average vertical resilient strain calculated from the primary response model; h is the thickness of the layer/sub-layer; and β_1 is the calibration factor.

The South African Mechanistic Design Method (SA-MDM) takes into account the permanent deformation of the base layer, as shown in Equations 2-5 and 2-6 (Theyse et al. 1996). The permanent deformation is related to the ratio of the working stress to the yield strength of the material, considering that high shear stress can extend into the base layer in thin-surfaced pavements for normal traffic loading.

$$F = \frac{\sigma_3[k(\tan^2(45+\frac{\phi}{2})-1]+2kc\tan(45+\frac{\phi}{2})}{\sigma_1-\sigma_3} \tag{2-5}$$

$$N = 10^{(2.605122F+3.480098)} \tag{2-6}$$

where F is the calculated safety factor; σ_1 and σ_3 are the major and minor principal stresses (compressive stress positive and tensile stress negative); k is a constant depending on the moisture condition; c is the cohesion coefficient; ϕ is the angle of internal friction; and N is the number of allowed load applications until failure.

Recently, Kim and Tutumluer (2005) developed a permanent deformation model of unbound aggregate considering the static and dynamic stress states and the slope of stress path loading. They found that multiple stress path tests could simulate the extension–compression–extension type of rotating stress states under a moving wheel pass and give much higher permanent strains than those of the compression-only single path tests.

Subgrade Rutting

Subgrade rutting is a longitudinal wheel-path depression that occurs when the subgrade exhibits permanent deformation or lateral migration due to loading. In this case, the pavement settles into the subgrade ruts, causing surface depressions in the wheel path. Usually, the vertical compressive strain on top of the subgrade is related to subgrade rutting for the case that the shear capacity of subgrade soil is not exceeded by the applied load. The Asphalt Institute (1982) proposed a rutting damage model, based on roadbed soil strain with a maximum threshold of 12.5mm rutting on subgrade (Equation 2-7).

$$N = 1.365\times10^{-9}(\varepsilon_v)^{-4.477} \tag{2-7}$$

where N is the number of allowed load repetitions until failure, and ε_v is the maximum vertical compressive strain on top of the subgrade.

Subgrade soil can also fail in shear when its shear capacity is exceeded by the applied heavy load. Thompson (2006) used a parameter called subgrade stress ratio (SSR) to estimate the rutting potential of a pavement system. The SSR is defined by Equation 2-8. The subgrade damage potential limits are SSR = 0.5, 0.6, 0.6-0.75, and >0.75 for low, acceptable, limited, and high ratios, respectively.

$$SSR = \sigma_{dev} / q_u \tag{2-8}$$

where SSR is the subgrade stress ratio; σ_{dev} is the deviatoric stress at the top of the subgrade; and q_u is the unconfined compressive strength of the subgrade soil.

2.2.2 Near-surface Cracking in Thick Asphalt Pavement

Many recent field studies found that surface or near-surface cracking is the major cracking mechanism in thick asphalt pavements or overlays (Figure 2.4). The cracking may initiate at the pavement surface and propagate downward (top-down cracking [TDC]), or initiate at some distance below the pavement surface and propagate upward or downward or both (near-surface cracking). These surface cracks were observed usually less than 10 years after construction as a premature failure. The cracks could be longitudinal or transverse at the vicinity of wheel-path areas. The depth of cracking is generally contained in the wearing course and does not extend into lower asphalt base layers. However, these surface cracks could allow water to penetrate into the pavement structure, and accelerate the pavement deterioration (Hugo and Kennedy 1985; Matsuno and Nishizawa (1992); Myers et al. (1998); Uhlmeyer et al. 2000).

Figure 2.4 Observed top-down cracking in field (after Uhlmeyer et al., 2000)

Several factors have been proposed as the causes of TDC or near-surface cracking. These include load-induced factors (tension, shear), material factors (low fracture energies, aging), construction factors (longitudinal construction joints, segregation); and temperature-induced factors (thermal stress) (Baladi et al. 2002). Among these factors, the high tensile or shear stress induced by tires at the pavement surface or near-surface is the most well-recognized load factor that contributes to the surface cracking mechanism. The repetitive load-induced tensile/shear stress could initiate the material damage process, while the thermal stress during daily thermal cycles accelerates the damage evolution and the asphalt aging reduces its fracture energy and fatigue life.

Myers et al. (1998) concluded that tensile stresses under the ribs of the loaded tire at the pavement surface induced by the shear stress of radial tires were responsible for causing TDC. It was found that the pavement structure has little effect on the reduction of tensile stresses around the tire-pavement contact area. Groenendijk (1998) found that the combined influence of the non-uniform contact stress and the aging of the asphalt surface layer could result in critical tensile stress at the surface rather than the bottom of the asphalt layer. Thom (2003) found that the value of the maximum principal tensile strain at 10mm below the pavement surface (at approximate 45° to surface) can be of a similar magnitude to the horizontal tensile strain at the bottom of asphalt layer, particularly for a thick pavement structure.

Wang et al. (2003) analyzed the cause of top-down cracking from the micromechanics point of view and found that the secondary tensile stress could be induced by the shear loading due to dilation. They suggested that the aggregate particle skeleton structure and the strength of the mastics are two important factors that may affect top-down cracking. Wang et al. (2006) found that the load-induced viscoelastic residual stress may be another potential mechanism for TDC using viscoelastic boundary element method. Yoo and Al-Qadi (2008) and Al-Qadi et al. (2008) showed that the vertical shear strain at the tire edge is more critical than the tensile strain at the bottom of asphalt layer for thick asphalt pavement and could be responsible for the development of near-surface cracking.

The literature survey shows that few fatigue models consider the combined effect of tensile and shear stress/strain on the prediction of surface or near-surface cracking. The MEPDG uses the elastic layer theory and the static uniform circular loading assumption to compute the tensile strains near the pavement surface for predicting the surface-initiated fatigue cracks (ARA 2004). The proposed fatigue equation for surface cracking is similar to the one for bottom-up fatigue cracking (Equation 2-1), while it has a different definition of the correction factor (k). However, the rationality and accuracy of this method is still not verified.

Lytton (1993) developed a cracking initiation model in the Strategic Highways Research Program (SHRP) research and found that the number of load cycles to reach failure could be predicted with excellent accuracy by taking into account the original stiffness, the state of stress expressed in terms of the mean principal stress and the octahedral shear stress at the bottom of the beam, and the percent air void and asphalt binder in the mix. Sousa el al. (2005) proposed the concept of “von Mises strain” to consider the normal and shear strain together and calculated the overlay fatigue life from flexural fatigue test with controlled strain (Equation 2-9).

$$\varepsilon_{VM} = \sqrt{\frac{1}{2}\left[(\varepsilon_1 - \varepsilon_3)^2 + (\varepsilon_1 - \varepsilon_2)^2 + (\varepsilon_2 - \varepsilon_3)^2\right]} \tag{2-9}$$

where $\varepsilon_{VM} = \varepsilon_1(1+v)$ for beam fatigue test conditions subjected to a four-point bending.

The researchers at the University of Florida proposed an Energy Ratio (ER) concept to calculate the optimum pavement thickness for resisting TDC. The ER is a dimensionless parameter defined as the dissipated creep strain energy ($DSCE_f$) threshold of the mixture divided by the minimum required dissipated creep strain energy ($DSCE_{\min}$) (Equation 2-10). The DSCE is the total energy under the stress-strain curve minus the elastic energy. The minimum required DCSE was derived from the material properties and structure design effect and calibrated with the observed cracking performance in the field (as shown in Equations 2-11 and 2-12). It is assumed that when ER is greater than one, a macro-crack will initiate and the process is not reversible.

$$ER = DCSE_f \,/\, DCSE_{\min} \tag{2-10}$$

$$DCSE_{\min} = \frac{m^{2.98} \cdot D_1}{f(S_t, \sigma_{\max})} \tag{2-11}$$

$$f(S_t, \sigma_{\max}) = \frac{6.36 - S_t}{33.44 \cdot \sigma_{\max}^{3.1}} + 2.46 \times 10^{-8} \tag{2-12}$$

where S_t is the tensile strength (in MPa); $\sigma_{\max}$ is the maximum tensile stress (in psi); and D_0 and D_1 are the creep parameters in the expression $D(t) = D_0 + D_1 t^m$.

The recent completed National Cooperative Highway Research Program (NCHRP) study (Roque et al. 2010) recognizes the top-down cracking could be caused by bending-induced surface tension away from the tire in asphalt layers of thin to medium thickness, or shear-induced near-surface tension at the tire edge in thicker asphalt layers. In this study, a viscoelastic continuum damage model and a fracture mechanics model are used to predict crack initiation and propagation, respectively. However, the developed model is still not suitable for integration and development of a top-down cracking performance prediction model for the mechanistic-empirical design.

2.3 Tire-Pavement Interaction

2.3.1 Measured Tire-Pavement Contact Area and Stresses

Tires serve many important purposes for a traveling vehicle including cushioning the vehicle against road roughness, controlling stability, generating maneuvering forces, and providing safety, among others (Gillespie 1993). Tire-pavement interaction is important for pavement design because the tire imprint area is the only contact area between the vehicle and the pavement at which the actual distribution of contact stresses is transferred to the pavement surface.

There are two important factors in the tire-pavement interaction mechanism: the contact area and the contact stresses. Many researchers have used a circular or equivalent rectangular contact area in pavement loading analysis (Huang 1993). The contact area of a truck tire is actually closer to a rectangular than a circular shape. Figure 2.5 shows an example of measured tire imprint for one tire in a dual-tire assembly (Al-Qadi et al. 2005). The rectangular contact area of each rib can be clearly observed. Thus, both the circular and equivalent rectangular contact areas overestimate the net contact area without considering either the tread pattern of the tire or the localized stress distribution under each tire rib. Tielking and Roberts (1987) found that the gross contact area increases as the tire load increases, while the effect of the inflation pressure on the contact area is not significant. Weissman (1999) reported that the length of the contact area depends primarily on the applied load, while the contact width remains almost constant as load increases, due to the rigidity of the tire wall.

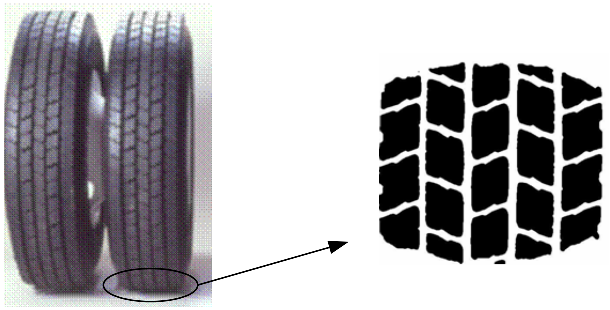

Figure 2.5 Measured tire imprint for one tire of dual-tire assembly (after Al-Qadi et al. 2005)

The tire-pavement contact stress can be measured using different devices, including diaphragm or hydraulic pressure cells, triaxial load pins, piezoelectric sensors, pressure-sensitive films, ultrasonic waves, etc. The accuracy of the measurement depends on the interface friction between the tire and measurement sensors, the size, resolution, and space interval of measurement sensors in the contact area, the loaded surface characteristics, the rolling speed, and the applied driving force.

Marshek et al. (1986) first attempted to measure the distribution of the vertical contact stresses of a bias-ply tire using pressure-sensitive films. They found that the stress distributions are not uniform, and that the vertical pressures exceed the inflation pressure in some areas. Ford and Yap (1990) measured the contact stresses for a slow-rolling tire over a strain gauge transducer embedded in the flat road bed with the use of a specially instrumented flat bed device. They found that, at a constant load, the tire inflation pressure variation primarily affects the contact stresses in the central region of the contact area. In contrast, at a constant inflation pressure, the tire load variation explicitly influences the contact stresses in the outer regions of the contact area.

Tielking and Abraham (1994) used an MTS servo-hydraulic system and triaxial load pins to measure the vertical contact stresses under tires and emphasized the cantilever effect caused by the usual offset flange wheel in heavy trucks. De Beer et al. (1997) performed a comprehensive measurement of tire contact stresses using the Vehicle-Road Surface Pressure Transducer Array (VRSPTA), that is further developed as Stress-in-Motion System (SIM). Their data have been used by many researchers to predict pavement responses. The VPSPTA consists mainly of an array of tri-axial strain gauge steel pins fixed to a steel base plate, together with additional non-instrumented supporting pins, fixed flush with the road surface. This system is designed to take measurements at wheel speeds from 1km/h up to 25km/h, and loads up to 200kN (vertical) and 20kN (horizontal). It was observed that the ratio of maximum stresses in the vertical, transverse, and longitudinal directions is 10: 3.6: 1.4 for a smooth bias ply tire.

Myers et al. (1999) reported that the radial tire causes higher transverse stresses than the bias ply tire, and the wide-base Bridgestone M844 tire has the highest vertical and transverse stresses. They also found that the bias ply tire has the maximum vertical stress at the shoulders of the tire, while the radial tire has the maximum vertical stress at the center of the tire which could be as high as 2.3 times the tire inflation pressure. The transverse shear stresses under the tire are affected by both the pneumatic effect and the Poisson's effect. Poisson's effect was more significant for radial tires, which have more flexible sidewalls and rigid treads than bias ply tires. Douglas et al. (2000) developed a steel bed transducer array device to measure vertical and tangential contact stresses for use in the evaluation of surface chip damage. They found that vertical contact stresses under the tire are extremely non-uniform under heavy loads with low inflation pressure, and that longitudinal contact stresses at the trailing edge of the tire contact patch are significantly greater when the inflation pressure was low.

2.3.2 Background on Tire Models

The two main types of tires are bias-ply and radial-ply tires. The radial-ply tire has become more popular because it causes less rolling resistance and heat generation compared to the bias-ply tire. Figure 2.6 shows the typical structure of a radial-ply tire. The radial-ply tire has one or more layers of radial plies in the rubber carcass with a crown angle of 90°. The crown angle is defined as the angle between the ply and the circumferential line of the tire. The radial plies are anchored around the beads that are located in the inner edge of the sidewall and serve as the “boundary” for the carcass to secure the tire casing on the rim. In addition, several layers of steel belts are laid under the tread rubber at a low crown angle. The radial plies and belt layers enhance the rigidity of the tire and stabilize it in the radial and lateral directions. The tread layer of the tire is usually patterned with longitudinal or transverse grooves and serves as a wear-resistance layer that provides sufficient frictional contact with the pavement and minimizes hydroplaning through good drainage of water in wet conditions (Wong 2002).

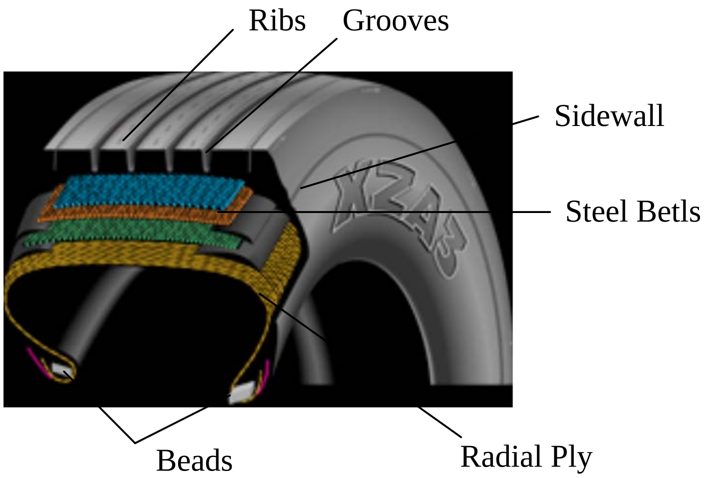

Figure 2.6 Schematic illustration of a radial-ply tire (after Michelin website on July 27, 2010)

Simplified 2-D tire models have been used in vehicle dynamics to predict tire performance in traction and stability control (Knothe et al. 2001). The common 2-D tire models can be divided into three main groups. The first group consists of the classical spring-damper models with single contact point with the road surface. The second group is the tire-ring models, which have an outer contour in contact with the ground. The third group consists of parametric mathematic models, such as the Pacjeka model. These models are derived from measurements of testing tires under various conditions. However, they are usually unsuitable for quantitative prediction of tire-pavement contact stresses in the tire imprint area.

General-purpose FE commercial software, such as ABAQUS, ANSYS, and ADINA, provide more tools to simulate 3-D tire behavior with rolling contact. The FE method is preferred because it can simulate the complex tire structure (tread, sidewall, radial ply, belt, bead, etc.) and consider representative material properties of each tire component. A survey of existing literature reveals many published works on FE simulations of tires. The complexity of tire models varies, depending on the features built into the model, including the types of FE formulation (Lagrangian, Eulerian, or Arbitrary Lagrangian Eulerian), material models (linear elastic, hyperelastic, or viscoelastic), type of analysis (transient or steady state), and treatment of coupling (isothermal, non-isothermal, or thermo-mechanical). Such tire models can be used to analyze the energy loss (rolling resistance), tire-terrain interaction, vibration and noise, and tire failure and stability.

The contact stresses developed at the tire-pavement interface are usually studied by assuming a deformable tire on a rigid surface. Tielking and Robert (1987) developed a FE model of a bias-ply tire to analyze the effect of inflation pressure and load on tire-pavement contact stresses. The pavement was modeled as a rigid flat surface and the tire was modeled as an assembly of axisymmetric shell elements positioned along the carcass mid-ply surface. Roque et al. (2000) used a simple strip model to simulate the cross-section of a tire and concluded that the measurement of contact stresses using devices with rigid foundation was suitable for the prediction of pavement responses. Zhang (2001) built a truck tire model using ANSYS and analyzed the inter-ply shear stresses between the belt and carcass layers as a function of normal loads and pressures.

Meng (2002) modeled a low profile radial smooth tire on rigid pavement surface using ABAQUS, and analyzed the vertical contact stress distributions under various tire loading conditions. Ghoreishy et al. (2007) developed a 3-D FE model for a 155/65R13 steel-belted tire and carried out a series of parametric analyses. They found that the belt angle was the most important constructional variable for tire behavior and the change of friction coefficient had great influence on the pressure field and relative shear between tire treads and road.

On the other hand, the assumption of a fully rigid wheel has been employed extensively in soil-wheel (or vehicle-terrain interaction) in the field of terramechanics. The geometry of a wheel is simplified to a rigid cylinder and the soil beneath the rolling wheel is usually assumed to be plastic. In these applications, the main objective is to predict the relationship between the wheel penetration or traction and the applied vertical force, torque, wheel geometry, material properties, and interface friction at the soil-wheel interface. Shoop (2001) simulated the coupled tire-terrain interaction and analyzed the plastic deformation of soft soil/snow using an Arbitrary Lagrangian Eulerian (ALE) adaptive mesh formulation. He suggested that the assumption of a rigid tire may be suitable for soft terrain analysis.

Hambleton and Drescher (2007) predicted the load-penetration relationships for indentation and steady-state rolling of rigid cylindrical wheels on cohesive soils and found good agreement between the theoretical predictions and experimental measurements. Hambleton and Drescher (2009) further studied the inclined rolling force and wheel sinkage using a three-dimensional model. They found that sinkage is inversely proportional to the width of the wheel and the wheel diameter. These findings are particularly useful for evaluating the “test rolling” procedure used for assessing the quality of subgrade compaction and optimizing the traction performance (or tire mobility) of off-road vehicles on unpaved roads.

2.3.3 Rolling Tire-Pavement Contact Problem

The tire-pavement interaction is essentially a rolling contact problem. Several challenges exist when modeling the tire-pavement interaction via a two-solid contact mechanics approach, such as nonlinear material properties, transient contact conditions, intricate structure of the tire, and nonlinear frictional interface (Laursen and Stanciulescu 2006). Due to the complexity of the problem, it is difficult to solve the tire-pavement contact problem analytically. Numerical methods are necessary and FEM is usually an appropriate choice.

In computational mechanics, two classical descriptions of motion are available: the Lagrangian formulation and the Eulerian formulation. The Eulerian formulation is widely used in fluid mechanics; the computational mesh is fixed and the continuum moves with respect to the mesh. The Lagrangian formulation is mainly used in solid mechanics; in this description each individual node of the computational mesh follows the associated material particle during the motion. However, it is cumbersome to model rolling contact problem using a traditional Lagrange formulation since the frame of reference is attached to the material. In this reference frame, a steady-state tire rolling is viewed as a time-dependent process and each point undergoes a repeated process of deformation. Such an analysis is computationally expensive because a transient analysis must be performed for each point and fine meshing is required along the entire tire surface (Faria et al. 1992).

An Arbitrary Lagrangian Eulerian (ALE) formulation combines the advantages of the Lagrangian and Eulerian formulations for solving the steady-state tire rolling problem (Hughes et al. 1981; Nackenhorst 2004). The general idea of ALE is the decomposition of motion ϕ into a pure rigid body motion, denoted by the mapping χ , and the superimposed deformation, denoted by $\hat{\phi}$, as shown in Figure 2.7. This kinematic description converts the steady moving contact problem into a pure spatially dependent simulation. Thus, the mesh needs to be refined only in the contact region and the computational time can be significantly reduced.

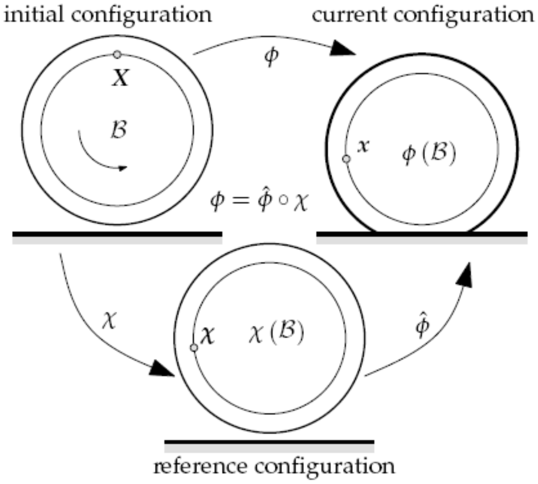

Figure 2.7 Arbitrary Lagrangian Eulerian decomposition of motion (after Nackenhorst 2004)

Another crucial point in the solution of the rolling contact problem is a sound mathematical description of the contact conditions. Contact problems are nonlinear problems and they are further complicated by the fact that the contact forces and contact patches are not known a *priori*. A solution to contact problems must satisfy general basic equations, equilibrium equations and boundary conditions, like solutions for a solid mechanics problem.

The popular approach to solve the contact problem is to impose contact constraint conditions using nonlinear optimization theory. Several approaches are used to enforce non-penetration in the normal direction, amongst which the most used are the penalty method, the Lagrange multipliers method or the augmented Lagrangian method (Wriggers 2002). If there is friction between two contacting surfaces, the tangential forces due to friction and the relative stick-slip behavior needs to be considered. The frequently used constitutive relationship in the tangential direction is the classical Coulomb friction law. This model assumes that the resistance to movement is proportional to the normal stress at an interface. In this case, the interface may resist movement up to a certain level; then the two contacting surfaces at the interface start to slide relative to each another. If the relative motion occurs, the frictional stress remains constant and the stress magnitude is equal to the normal stress at the interface multiplied by the friction coefficient.

2.3.4 Friction at Tire-Pavement Interface

The development of friction force between tire rubber and a rough hard surface has two contributions that were commonly described as the adhesion and hysteretic deformation, respectively. The adhesion component is the result of interface shear and more important for a clean and smooth surface. The magnitude of adhesion component is related to the product of actual contact area and the interface shear strength. The hysteresis component is the result of damping losses and energy dissipation of the rubber excited by the surface asperities (Kummer and Meyer 1969).

Because the mechanics of rubber friction are very complex as a consequence of many interacting phenomena, the friction behavior between the tire and pavement is usually determined experimentally. Pavement friction is defined as the retarding tangential force developed at the tire-pavement interface that resists longitudinal sliding when braking forces are applied to the vehicle tires or sideways sliding when a vehicle steers around a curve. The sliding friction coefficient is computed using Equation 2-13.

$$\mu = F_h / F_v \tag{2-13}$$

where μ is sliding friction coefficient; F_h is tangential friction force at the tire-pavement surface; and F_v is vertical load on tire.

The type of equipment used for testing tire-pavement friction varies among transportation agencies. Common techniques include the locked wheel tester using a smooth or ribbed tire, fixed slip device, variable slip device, and side force device. Experimental measurements have shown that the friction force at tire-pavement interface is influenced by many factors, including vehicle factors (load, speed, slip ratio, slip angle, camber angle), tire factors (tire type, inflation pressure, tread design, rubber composition), surface conditions (micro- and macro-texture, dryness and wetness), and environmental factors (temperature and contamination) (Henry 2000; Hall et al. 2006).

A number of friction models have been developed to characterize the tire pavement friction behavior in vehicle dynamics and stability control. The “Magic Formula” is a well-known empirical model used in vehicle handling simulations, as shown in Equation 2-14 (Pacejka 2006). The “Magic Formula” can be used for characterizing the relationships between the cornering force and slip angle, between the self-aligning torque and slip angle, or between the friction force and slip ratio. This model has been shown to suitably match experimental data obtained under various testing conditions, although the model parameters do not have physical meanings.

$$F(s) = c_1 \sin(c_2 \arctan(c_3 s - c_4 (c_3 s - \arctan(c_3 s)))) \qquad (2\text{-}14)$$

where $F(s)$ is the friction force due to braking or the lateral force or the self-aligning torque due to cornering; c_1, c_2, c_3,and c_4 are fitted model parameters; and s is the slip ratio or slip angle.

Savkoor (1986) found that friction of rubber polymers was closely related to its viscoelastic behavior due to the flexibility of polymer chains. He proposed a formulation that incorporated the effect of the sliding velocity on the friction coefficient, as shown in Equation 2-15. In this equation, the friction coefficient increases with sliding velocity until a maximum value is reached at a certain speed, followed by a decrease of the friction coefficient.

$$\mu_s = \mu_0 + (\mu_m - \mu_0)\exp[-h^2 \log^2 (v_s / v_m)] \qquad (2\text{-}15)$$

where μ_0 is static friction coefficient; μ_s is sliding friction coefficient; μ_m is maximum value of μ_s at the slip speed of v_m; v_s is slip speed; and h is a dimensionless parameter reflecting the width of the speed range in which friction varies significantly.

Dorsch et al. (2002) found that the friction coefficient between rubber tire and road surface is a non-linear function of pressure, sliding velocity, and temperature. The function can be formulated as a power law or as a quadratic formula, Equations 2-16 and 2-17.

$$\mu = c_0 p^{c_1} {v_s}^{c_2} \qquad (2\text{-}16)$$

$$\mu = c_0 p + c_1 p^2 + c_2 v_s + c_3 {v_s}^2 + c_4 p v_s \qquad (2\text{-}17)$$

where μ is friction coefficient, c_0, c_1, c_2, c_3,and c_4 are fitted model parameters, v_s is slip speed, and p is normal pressure.

Extensive measurements have been conducted in the pavement field to measure the friction between the tire and pavement, and the Penn State model is widely used (Henry 2000). It relates the friction to slip speed by testing a fully locked tire on pavement surface, as shown in Equation 2-18. It provides a good estimate of the friction when the locked wheel condition is reached (slip ratio =100%).

$$\mu = \mu_0 e^{-v_s / s_p} \tag{2-18}$$

where μ is friction coefficient at slip speed of v_s; μ_0 is friction coefficient at zero speed that is related to pavement surface micro-texture; and s_p is speed number that is highly correlated with pavement surface macro-texture.

The Rado model, known also as the logarithmic friction model, is used to model the friction taking place while a tire proceeds from the free rolling to the locked wheel condition, as shown in Equation 2-19. This model describes the two phases that occur in the braking process. During the first phase, the tire rotation is gradually reduced from free rolling to a locked state. During the second phase, the tire reduces its speed under locked state until a complete stop. In the two phases, the corresponding friction coefficient is first increased to the peak friction at the critical slip ratio and then decreases with the increase of the slip ratio.

$$\mu = \mu_{peak} \cdot e^{-\left[\frac{\ln(v_s / s_{peak})}{C}\right]^2} \tag{2-19}$$

where v_s is slip speed; s_{peak} is slip speed at peak friction; μ_{peak} is peak friction coefficient; and C is shape factor mainly dependent on surface texture.

2.4 Summary

A review of the mechanistic analysis of pavement responses and pavement failure mechanisms was presented in this chapter. The review indicates that in order to accurately predict pavement responses under vehicular loading, the model needs to consider realistic tire-pavement interaction and appropriate material properties for each pavement layer. The pavement responses responsible for failure and critical failure locations vary with pavement structure; thin and thick asphalt pavements fail in different mechanisms. Various and multiple distress modes could occur in different structural layers of thin asphalt pavements, while the failure close to the pavement surface is more critical for thick asphalt pavements.

The contact stress distribution at the tire-pavement interface that represents vehicular loading can be obtained from experimental measurements or theoretical models. A literature review of the developed tire models indicates that the complexity of tire models varies depending on the features built into the model and the purpose of analysis. For predicting the tire-pavement contact stresses, deformable tire structure and the frictional contact between the rolling tire and pavement surface need to be considered in the model.

CHAPTER 3 MODELING OF TIRE-PAVEMENT INTERACTION

3.1 Measured Tire-Pavement Contact Stresses

Experimental measurements have shown that when a tire loading is applied to a pavement surface, three contact traction components are generated: vertical, transverse, and longitudinal. Figure 3.1 shows an example of normalized contact stresses beneath the center rib of one tire in a dual-tire assembly (275/80R22.5) at a very slow rolling speed (close to static) (Al-Qadi et al. 2008). These contact stresses were measured by the tire manufacturer using three-dimensional load pins at the tire-pavement interface. In this case, longitudinal and transverse tangential contact stresses ranged from 11-34% of the maximum vertical stress. Both the vertical compression stresses and transverse tangential stresses have a convex shape along the longitudinal contact length, while the longitudinal tangential stresses vary significantly between entrance and exit parts of a tire imprint, having backward stresses in the front half and forward stresses in the rear half.

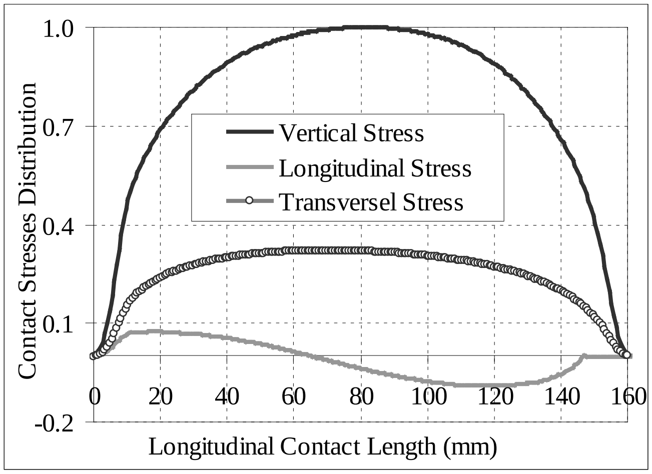

Figure 3.1 Normalized tire contact stress distributions (after Al-Qadi et al. 2008)

The normalized vertical and transverse contact stresses under each tire rib are shown in Figures 3.2 and 3.3, respectively, for one tire in a dual-tire assembly (275/80R22.5) and a wide-base tire (455/55R22.5). It is clear that the vertical stresses are higher underneath the inner tire ribs (crown) than the outer tire ribs (shoulder). This indicates the significant non-uniform distribution of vertical contact stresses. Due to the fact that the transverse contact stresses are mainly associated with the Poisson effect of rubber material for radial ply tires, the transverse tangential stresses show the asymmetric distribution beneath each rib approximately. If averaged over the entire tire width, the total average transverse contact stress is near zero. However, the transverse contact stresses may be either tension or compression at two sides of each tire rib, while the smallest stress was found at the center of each rib. In addition, the transverse tangential stresses were found ranging from about 24% of the vertical stress at the center rib to 35-52% of the vertical contact stress at edge ribs. Thus, the localized transverse contact stresses under each rib cannot be ignored when predicting the pavement responses at surface or near-surface.

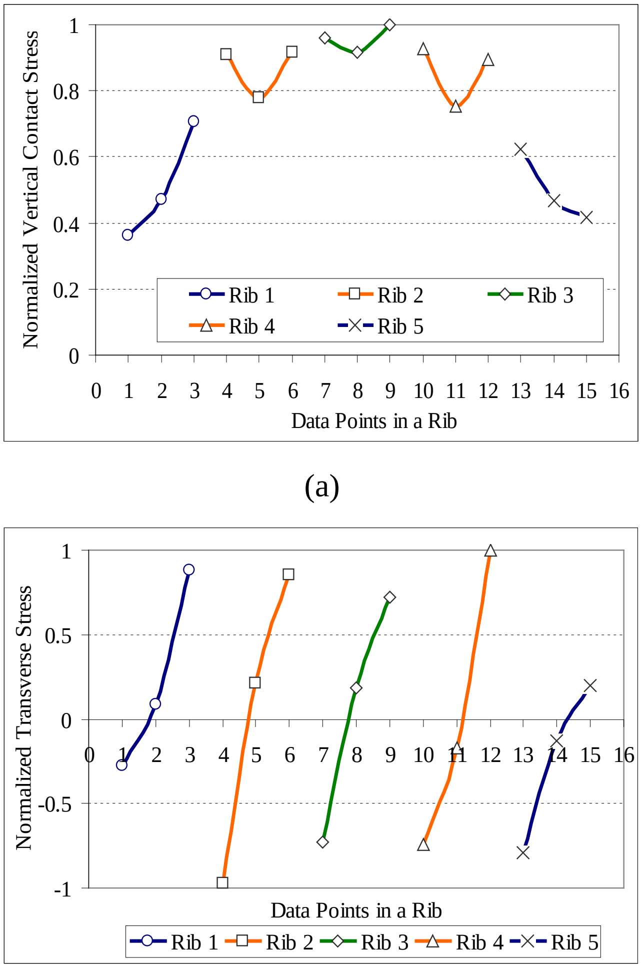

(a)

(b)

Figure 3.2 Normalized distributions of (a) vertical contact stresses; and (b) transverse contact stresses under each rib of one tire in a dual-tire assembly

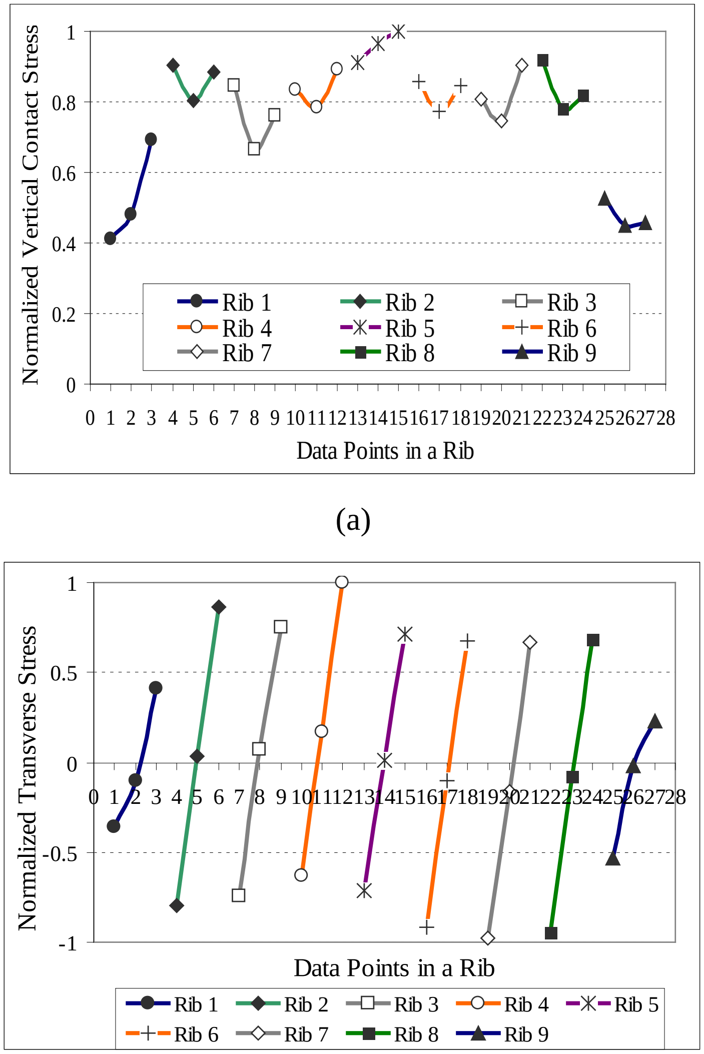

(a)

(b)

Figure 3.3 Normalized distributions of (a) vertical contact stresses; and (b) transverse contact stresses under each rib of a wide-base 455 tire

It is expected that even when the magnitude of wheel load is similar, tire-pavement contact stresses will vary considerably depending upon the type of tire (radial versus bias-ply, dual versus wide-base) and the configuration of treads. Figures 3.4 (a) and (b) compare the maximum vertical and transverse contact stresses under each rib of a dual-tire assembly and the new generation of wide-base 455 tire (35.5kN and 724kPa). The vertical contact stresses under the center ribs of the wide-base tire are smaller than those of a dual-tire assembly. Thus, the wide-base tire has a relatively more uniform vertical stress distribution within the contact width. The maximum transverse contact stresses located at two sides of each rib vary along the tire width for both the dual-tire assembly and the wide-base tire. The wide-base tire has smaller transverse contact stresses than the dual-tire assembly, especially at tire edge ribs.

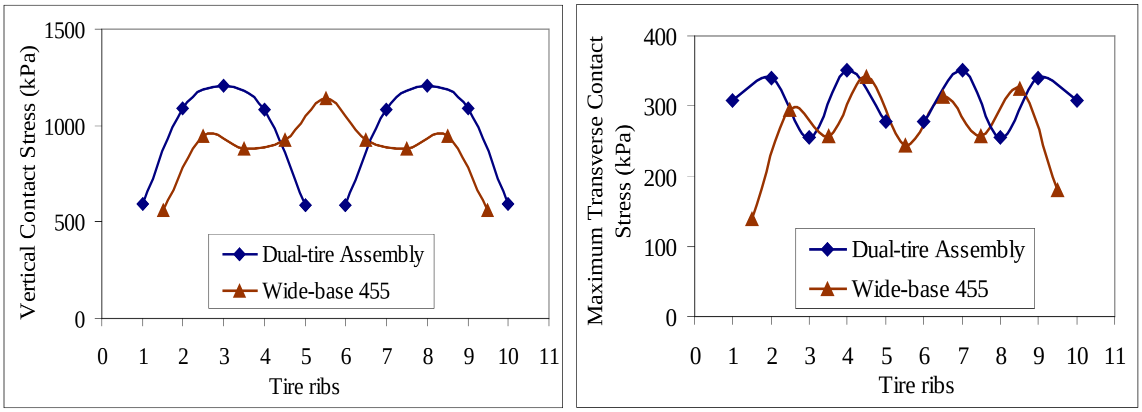

(a) (b)

Figure 3.4 Comparisons between a dual-tire assembly and a wide-base tire for (a) vertical and (b) transverse contact stresses

3.2 Hertz Contact Pressure Distribution

Contact mechanics is the study of the stresses and deformation which arise when the surfaces of two solid bodies are brought into contact. The original work on contact mechanics between two elastic solids was conducted by Hertz (1882). In the Hertz contact theory, the localized stresses that develop as two curved surfaces come in contact are dependent on the normal contact force, the radius of curvature of both bodies, and the elastic modulus of both bodies. Based on the classical Hertz contact theory, the contact radius and pressure between two spheres can be calculated using Equations 3-1 and 3-2, respectively; the contact width and pressure between two parallel cylinders can be calculated using Equations 3-3 and 3-4, respectively (Figure 3.5).

$$p(r) = \frac{3P}{2\pi a^2}\sqrt{1-(r/a)^2} \tag{3-1}$$

$$a = \left(\frac{3PR}{4E^*}\right)^{1/3} \tag{3-2}$$

$$p(x) = \frac{2P}{\pi bL}\sqrt{1-(x/b)^2} \tag{3-3}$$

$$b = \left(\frac{2PR}{\pi L E^*} \right)^{1/2} \tag{3-4}$$

$$\text{with } \frac{1}{R} = \frac{1}{R_1} + \frac{1}{R_2} \text{ and } \frac{1}{E^*} = \frac{1-\nu^2}{E_1} + \frac{1-\nu^2}{E_2}$$

where P is the applied load; a is the radius of contact area between two spheres; b is the contact width between two cylinders; $p(r)$ is the pressure at radius distance of r; $p(b)$ is the pressure at distance of x from center; R is relative radius of contact surfaces; R_1 and R_2 are radius of two contact surfaces; E^* is the contact modulus; and E_1 and E_2 are the elastic moduli of two objects in contact.

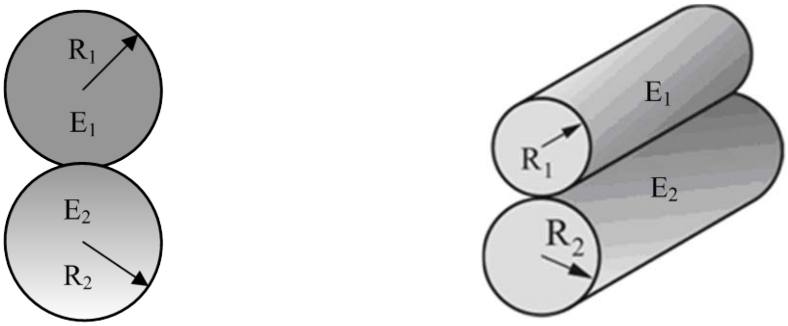

(a) (b)

Figure 3.5 Contact between (a) two spheres; and (b) two parallel cylinders

The Hertz contact theory has been actively used in tribology (such as the design of gears and bearing) and the wheel-rail contact problem. The application of Hertz contact theory is based on the following limiting conditions: 1) the two contact bodies are perfectly elastic material; 2) no tangential force is transmitted between contact surfaces; 3) no spin or sliding of the contact body is considered; 4) the contact surfaces are smooth; and 5) the contact area is small compared to the sizes and the radius of curvature of the contact bodies (non-conforming contact).

For the tire in contact with pavement, the tire can be considered as a sphere or cylinder with a wheel radius (R_1) and the pavement as an infinite surface ($R_2 = \infty$). The Poisson's ratio of the tire is assumed as 0.499 and the pavement is as 0.3. The equivalent elastic modulus of the whole tire structure is assumed as 50MPa and the pavement modulus is assumed in the range of 1000 to 8000MPa. Using the Hertz contact theory, the calculated peak contact stress under a wheel load of 17.8kN is shown in Figure 3.6. The results show that the calculated peak contact stress is much greater than the measured vertical contact stress at the tire-pavement interface. This is because the Hertz contact theory is only suitable for the contact between two rigid bodies and cannot take into account the large deformation of the tire body, which significantly reduces the contact pressure. Interestingly, it was found that the peak contact stress is not affected by the variation of pavement modulus. This indicates that the contact pressure is mainly dependent on the modulus of tire when the tire (soft body) is in contact with the pavement (stiff body). However, this is not the case for the contact between two bodies with similar modulus such as the wheel-rail contact. As shown in Figure 3.7, the contact pressure increases significantly as the modulus ratio of two stiff contact bodies (E2/E1) increases.

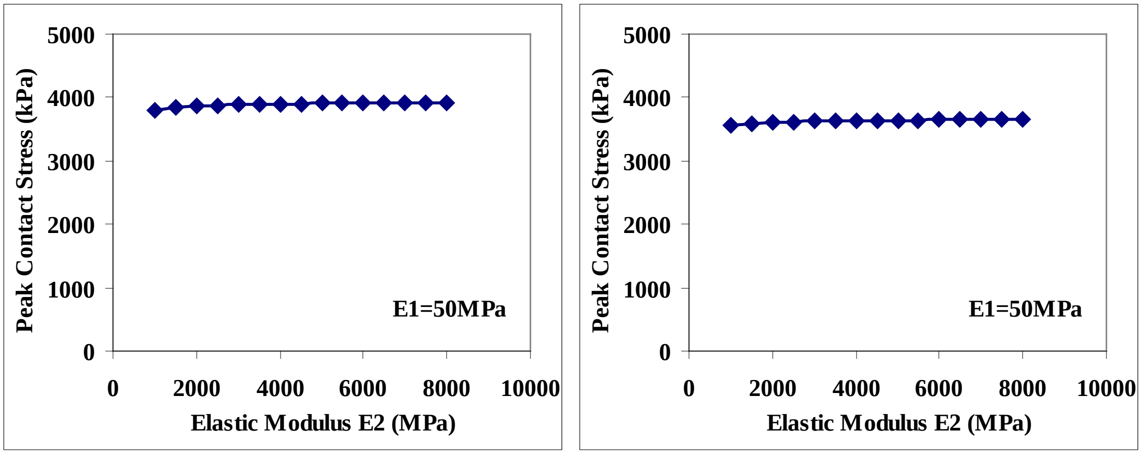

Figure 3.6 Peak contact stress between a soft body (tire) and a stiff body (pavement) for (a) spherical contact; and (b) cylindrical contact

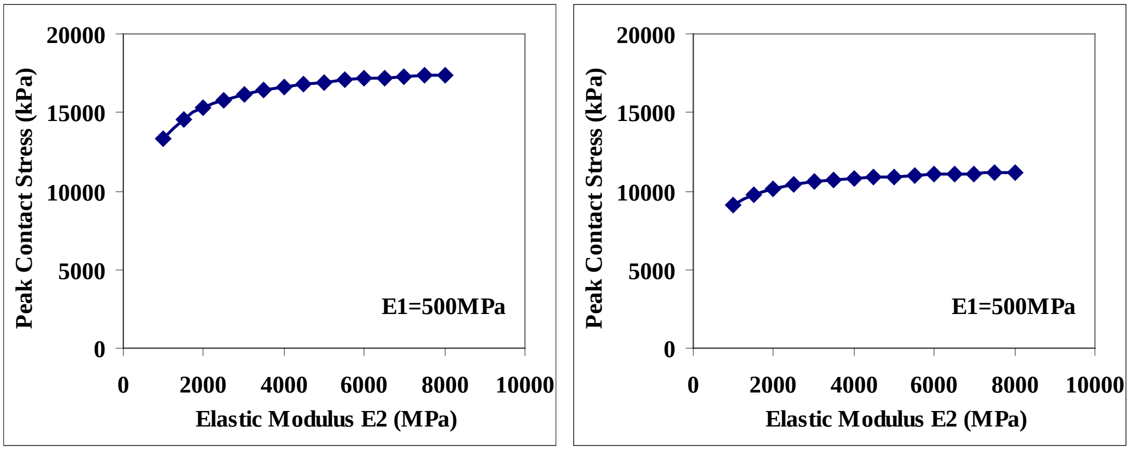

Figure 3.7 Peak contact stress between two stiff contact bodies for (a) spherical contact; and (b) cylindrical contact

In addition, several differences exist between the assumptions of Hertz contact theory and the real tire-pavement contact. These differences include: 1) tire is pneumatic (hollow) with pressurized inner surface rather than solid; 2) tire is a composite structure that consists of soft rubber and stiff reinforcement; 3) tire-pavement contact surface is not frictionless and tire tread (that consists of ribs and grooves) is not continuous. Therefore, it is difficult to obtain accurate contact stress distributions at the tire-pavement interface using the classical Hertz contact theory.

3.3 Development of Tire-Pavement Interaction Model

3.3.1 Descriptions and Assumptions of Tire Model

Contact stress measurements at the tire-pavement interface are expensive and time-consuming. During experiments, it is generally difficult to consider all the tire loading and operating variables because of the extensively large testing matrix and measurement difficulties associated with a rolling tire. Therefore, development of an approach to simulate tire-pavement interaction would be of significant benefits. A 3-D FE air-inflated tire model is developed in this study using ABAQUS software in order to simulate the interaction between a truck tire and a non-deformable pavement surface.

Theoretically, a tire model should consider three main characteristics: 1) the composite structure and the anisotropy due to the significant difference in stiffness between rubber and reinforcement; 2) the relatively large deformation due to flexibility of tire carcass during contact with pavement surface; and 3) the near-incompressibility and the nonlinearity of rubber material (Wong 2002). The tire models commonly used for tire design purposes must accurately predict the deformation of the whole tire and the interaction of internal components as well. This study focuses on tire deformation with respect to the contact region and the resultant contact stress distributions at the tire-pavement interface. This focus allows for the development of relatively simple tire models to ensure high computational efficiency.

Figure 3.8 shows cross-sectional views of the modeled radial ply tire having five straight longitudinal ribs. The outer radius of the tire is 506mm and the tire height is 220mm. The wall-to-wall tire width is 275mm and the width of tread area is approximately 200mm. The thickness in the tread area is 18mm, with 13-mm groove depth. The widths of the ribs are 30-40mm with 10-mm grooves between adjacent ribs. The tire model comprises one radial ply, two steel belts, and a rubbery carcass (sidewall and tread). The two steel belts were oriented at +20° and −20° with respect to the hoop (circumferential) direction, while the radial ply is perpendicular to the circumferential direction of the tire. The two steel belts are located approximately 15 and 17mm above the outer surface of the tread, respectively. The rim was modeled as rigid body and in contact with the bead at the end of sidewall. To optimize computation speed and resolution, a finer mesh was chosen around the tread zone, and a coarse mesh was used in the sidewall.

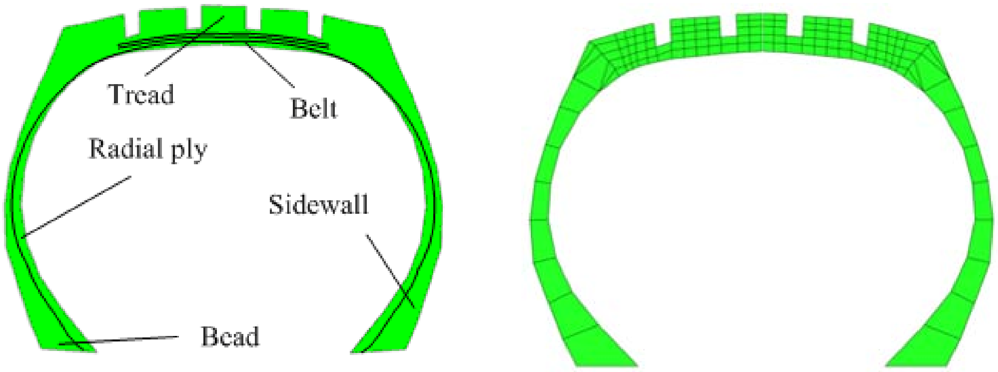

(a) (b)

Figure 3.8 Cross-section views of (a) modeled tire and (b) tire mesh

The FE tire model was built in two steps. First, a 2-D axisymmetric tire model was built with four-node axisymmetric continuum elements for rubber. These bi-linear elements allow for the consideration of twisting the rubber-cord composite that generally takes place in tires during loading. The radial ply and layered steel belts were modeled as surface membrane elements with rebar layers. These reinforced surface membrane elements were embedded in “host” continuum elements (Figure 3.9[a]). Then, the 3-D tire model was generated by revolving the 2-D mesh around its symmetric axis (Figure 3.9[b]).

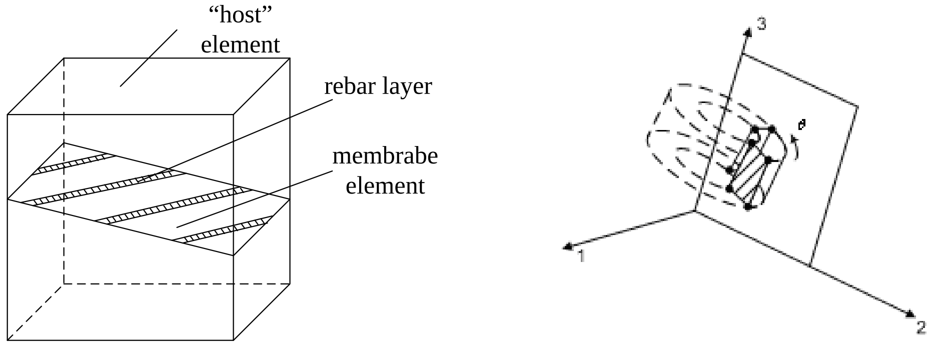

(a) (b)

Figure 3.9 Schematic illustration of (a) embedded element (b) 3-D model generation

3.3.2 Modeling of Tire-Pavement Interaction

The tire-pavement interaction is a complicated problem, because it involves three nonlinear factors (material, geometry, and contact). First, pavement is a multi-layer structure with nonlinear material properties for each layer and the tire is a composite structure including rubber and reinforcement. Second, when a tire is in contact with a pavement surface under a wheel load, the tire exhibits large nonlinear deformation. Third, the contact condition between the tire and the pavement surface is complex. Contact area and stress vary with wheel load, tire inflation pressure, tire rolling condition, and interface friction condition. In this study, the pavement was modeled as a non-deformable flat surface to achieve better computation efficiency and stability. This assumption is considered reasonable because the tire deformation is much greater than the pavement deflection when wheel load is applied on the tire and transmitted to the pavement surface.

The large deformation of the tire was taken into account by using a large-displacement formulation for the consideration of geometric nonlinearity in ABAQUS.

The tire-pavement interaction was simulated in three load steps, shown in Figure 3.10. First, the axisymmetric tire model was loaded with uniform tire inflation pressure at its inner surface. Second, the 3-D tire model was generated and placed in contact with pavement under the applied load. Finally, the tire was rolled on a rigid flat surface with different angular (spinning) velocities and transport velocities. The tire rolling process was modeled using "steady-state transport analysis" in ABAQUS/Standard. Steady-state transport analysis utilizes implicit dynamic analysis and can consider the effect of tire inertia and the frictional effects at the tire-pavement interface.

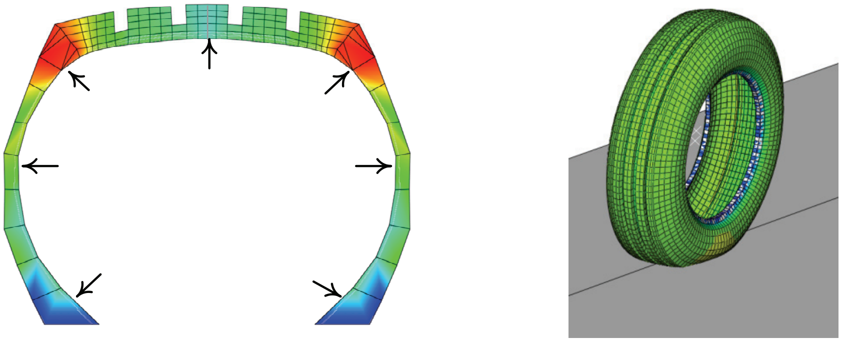

(a) (b)

Figure 3.10 Simulation of tire-pavement interaction: (a) inflating tire with internal pressure; and (b) applying load on tire and rolling

In the steady-state transport analysis, the Arbitrary Lagrangian Eulerian (ALE) formulation was used rather than traditional Lagrange or Eulerian formulations. The ALE uses a moving reference frame, in which rigid body rotation is described in an Eulerian formulation and the deformation is described in a Lagrange formulation (Nackenhorst 2004). This kinematic description converts the steady-state moving contact problem into a pure spatially dependent simulation. Thus, the mesh needs to be refined only in the contact area. A mesh convergence analysis was performed with a series of progressively finer FE meshes in the contact area. The predicted contact stress results were compared for each mesh until changes in numerical results were less than 5% (Figure 3.11).

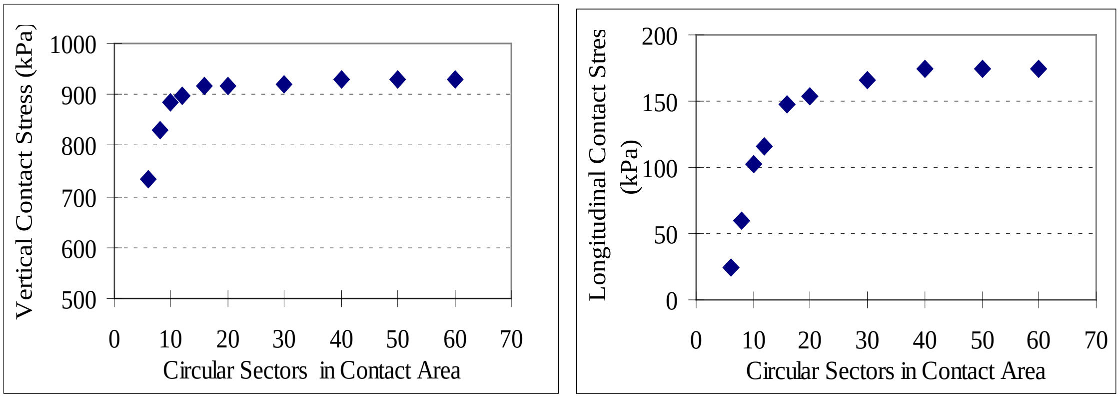

(a) (b)

Figure 3.11 Mesh convergences of (a) vertical and (b) longitudinal contact stresses

A crucial point in the simulation of the tire-pavement interaction is the appropriate modeling of tire-pavement contact. The contact between the tire and the pavement surface consists of two components: one normal to the pavement surface and one tangential to the pavement surface. The contact status is determined by nonlinear equilibrium (solved through iterative procedures) and governed by the transmission of contact forces (normal and tangential) and the relative separation/sliding between two nodes on the surfaces in contact. There are three possible conditions for the nodes at the interface: stick, slip and separation (Equations 3-5, 3-6, and 3-7). In the first two cases, nodes are in contact and both normal and tangential forces are transmitted between contacting surfaces. The maximum tangential force is limited by the frictional resistance determined by the Coulomb's law of friction. The non-penetration in the normal direction and the stick contact constraints in the tangential direction are enforced using the penalty method. In modeling, finite-sliding is allowed to account for the relative motion (separation or sliding) of two contacting surfaces when tire rolling is simulated.

$$\text{Stick condition: } g = 0;\ p < 0;\ \text{and } \left[\tau_1^2 + \tau_2^2\right]^{0.5} < \mu \cdot p \tag{3-5}$$

$$\text{Slip condition: } g = 0;\ p < 0;\ \text{and } \left[\tau_1^2 + \tau_2^2\right]^{0.5} = \mu \cdot p \tag{3-6}$$

$$\text{Separation condition: } g > 0;\ p = 0;\ \text{and } \tau = 0 \tag{3-7}$$

where p is the normal force (compression is negative); g is the gap between two contact nodes; τ_1 and τ_2 are tangential forces; and μ is sliding friction coefficient.

ABAQUS/Standard requires the definition of the contact pair (e.g. the master and slave surfaces). The master surface is usually the more rigid surface between two contact surfaces. As default, the slave surface has finer meshes and the nodes of the slave surface are prohibited from penetrating the element boundaries of the master surface. Two discretization approaches are available in contact modeling: node-to-surface and surface-to-surface. The node-to-surface contact prevents any penetration of slave nodes into the master surface. The surface-to-surface contact enforces the constraints in an average sense over finite regions of the slave surface. As the mesh is refined, the discrepancies between the two methods decrease. For a given mesh refinement, the surface-to-surface approach tends to provide more accurate stresses. In addition, node-to-surface contact tends to be less costly per iteration than surface-to-surface contact; while finite-sliding contact tends to converge easily with surface-to-surface contact. Thus, the surface-to-surface contact is used in this study and the non-deformable pavement surface is defined as the master surface.

3.3.3 Material Properties

Rubber is a near-incompressible and hyperelastic material with slight viscoelastic behavior. However, tire manufacturers usually do not reveal information on material properties of the tire structure. This study focuses on the contact patch shape and stress distribution at the tire-pavement interface rather than the internal stresses in the tire structure. Hence, the rubber was assumed as linear elastic material with a Poisson’s ratio close to 0.5. Different parts of rubber elements (sidewall, shoulder, belt rubber, and tread) were modeled having variable elastic stiffness. The reinforcements (radial ply and steel belts) were modeled as a linear elastic material.

Tire load-deflection curves from experimental measurements were used to calibrate the tire model parameters in this study. The initial elastic modulus of each tire component was based on tire models in the literature (Zhang 2001; Ghoreishy et al. 2007). The elastic properties of rubber and reinforcements were then adjusted to obtain deflection values close to experimental measurements provided by tire manufacturers. Sensitivity analysis showed that tire deflection is primarily affected by sidewall stiffness and the orientation of steel belts (crown angles). Good agreements were achieved between the predicted and measured deflections under various load and tire inflation pressure levels as shown in Figure 3.12. The final selected elastic material properties of each tire component are presented in Table 3.1.

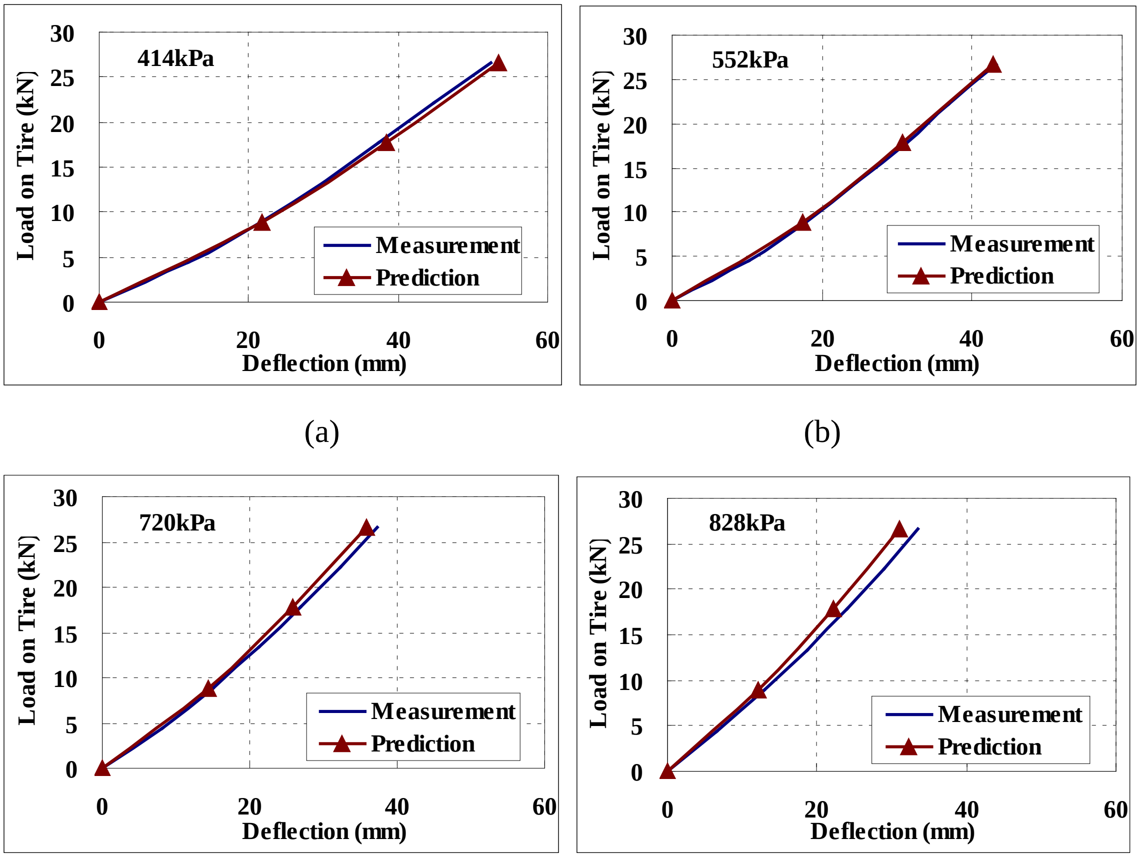

(a) (b)

(c) (d)

Figure 3.12 Comparisons between measured and calculated tire deflections at (a) 414kPa; (b) 552kPa; (c) 690kPa; and (d) 828kPa

Table 3.1 Elastic Material Properties of Tire Components

Tire components	Material	Elastic modulus (MPa)	Poisson's ratio	Density (kg/m^3)
Tread	Rubber	4	0.49	1100
Belt rubber	Rubber	12	0.49	1100
Sidewall	Rubber	0.5	0.49	1100
Shoulder	Rubber	8	0.49	1100
Radial ply	Polyester	9000	0.3	1500
Belt 1	Steel	170000	0.3	5900
Belt 2	Steel	170000	0.3	5900

3.3.4 Comparison between Measured and Predicted Contact Stresses

To examine the accuracy of the developed model, the predicted contact stresses at the tire-pavement interface were compared to the experimental measurements provided by the tire manufacturer. Measurements were collected as the tire rolled over the instrumentation at a very low speed (close to static). Therefore, the static loading condition of the tire was simulated in the comparison. It is noted that the friction between the tire and instrumentation depends on the geometry and interval of sensors used in the measurements. A friction coefficient of 0.3 was selected through a sensitivity analysis because it provides the best match between the predicted and measured contact stresses.

Figure 3.13 compares the transverse distributions of contact stresses from model predictions and experimental measurements (17.8kN and 724kPa) for the vertical and transverse contact stresses, respectively. In general, the predicted contact stresses agree fairly well with those measured by experiments. Although some variations were observed, the tire model captured the non-uniform distribution of vertical contact stresses and the localized asymmetric distribution of transverse contact stresses under each individual tire rib. The differences between the predicted and measured contact stresses could be due to two reasons: 1) the hyperelasticity of rubber was not considered in the tire model; 2) the geometry and composite structure of the modeled tire may differ slightly from that of the experimental tire.

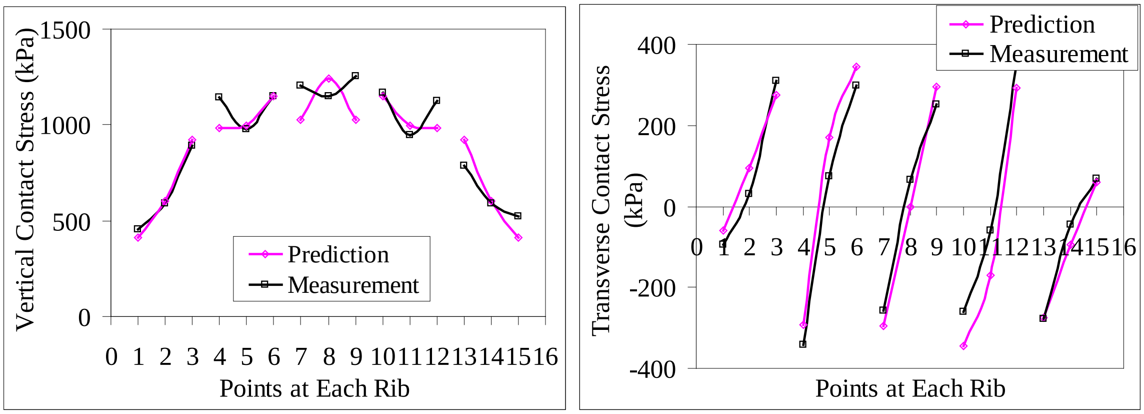

(a) (b)

Figure 3.13 Predicted and measured (a) vertical contact stresses; and (b) transverse contact stresses

Table 3.2 compares the contact stresses from model predictions and experimental measurements under various load and pressure levels. It was found that the stress ratios for the maximum contact stresses in three directions (vertical, transverse, and longitudinal) were approximately 1:0.3:0.15 from both measurements and FE model results. The maximum vertical stress is relatively constant as the load increases, while it increases as the tire pressure increases. More detailed analyses of contact stress distributions under various load and tire pressure levels are described in the following parts.

Table 3.2 Comparisons of Predicted and Measured Contact Stresses

Load (kN)	Pressure (kPa)	Maximum vertical contact stress (MPa)		Ratio of maximum contact stresses in three directions (vertical: transverse: longitudinal)	
		Predicted	Measured	Predicted	Measured
17.8	724	1234	1257	1:0.28:0.12	1:0.28:0.12
22.3		1252	1271	1:0.27:0.14	1:0.29:0.15
26.8		1262	1271	1:0.27:0.15	1:0.30:0.18
22.3	690	1214	1230	1:0.27:0.15	1:0.29:0.18
	724	1252	1271	1:0.27:0.14	1:0.29:0.17
	760	1303	1343	1:0.28:0.14	1:0.29:0.15

Figure 3.14 compares the predicted and measured contact lengths and contact areas as the tire is loaded at 17.8, 22.3, and 26.8kN at 724-kPa inflation pressure. At each load level, the contact lengths are different for the middle, intermediate and edge rib. The results show that the predicted contact lengths and contact areas are slightly greater than the measured values. A linear regression relationship is presented between predicted and measured contact lengths and contact areas; as shown in Figure 3.14(a) and (b), respectively.

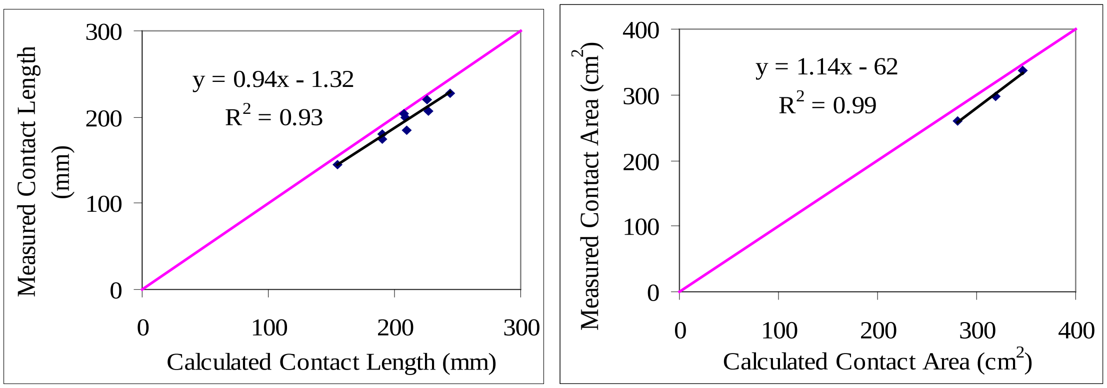

Figure 3.14 Comparisons of predicted and measured contact (a) lengths; and (b) areas

3.4 Distribution Patterns of Tire-Pavement Contact Stresses

Figure 3.15 shows the 3-D contact stresses predicted from the tire-pavement interaction model at static loading condition (17.8kN and 724kPa). In these plots, zero values were assigned to the groove areas between adjacent ribs. As the tire is pressed against a flat surface, the tread rubber is compressed in the flattened contact patch and the sidewall of the tire is in tension. The bending stress in the sidewall causes the non-uniform distribution of vertical contact stresses in the contact patch, particularly at the edge of the contact patch. At the same time, the Poisson’s effect and the restricted outward movement of each tire rib causes tangential stresses to develop. The plots clearly show that the vertical and transverse contact stresses have a convex shape along the contact length, while the longitudinal contact stresses have a reversed pattern with backward stresses in the front half and forward stresses in the rear half. The distribution patterns of the predicted contact stresses are consistent with the distribution patterns of the measured contact stresses (as shown in Figure 3.1).

Figure 3.16 shows plots of the predicted contact stress distributions along tire contact length, respectively, for vertical, transverse, and longitudinal contact stress under each rib. The plots show that the maximum vertical and longitudinal contact stresses are under the center rib of the tire, while the maximum transverse contact stress is under the intermediate rib of the tire. It is noted that the transverse contact stress increases in magnitude with lateral distance from the center of each rib and reaches its maximum at the edge of each rib (as shown in Figure 3.15(b)). Figure 3.16(b) only shows the transverse contact stresses beneath one side of the tire rib; it is approximately asymmetric distribution.

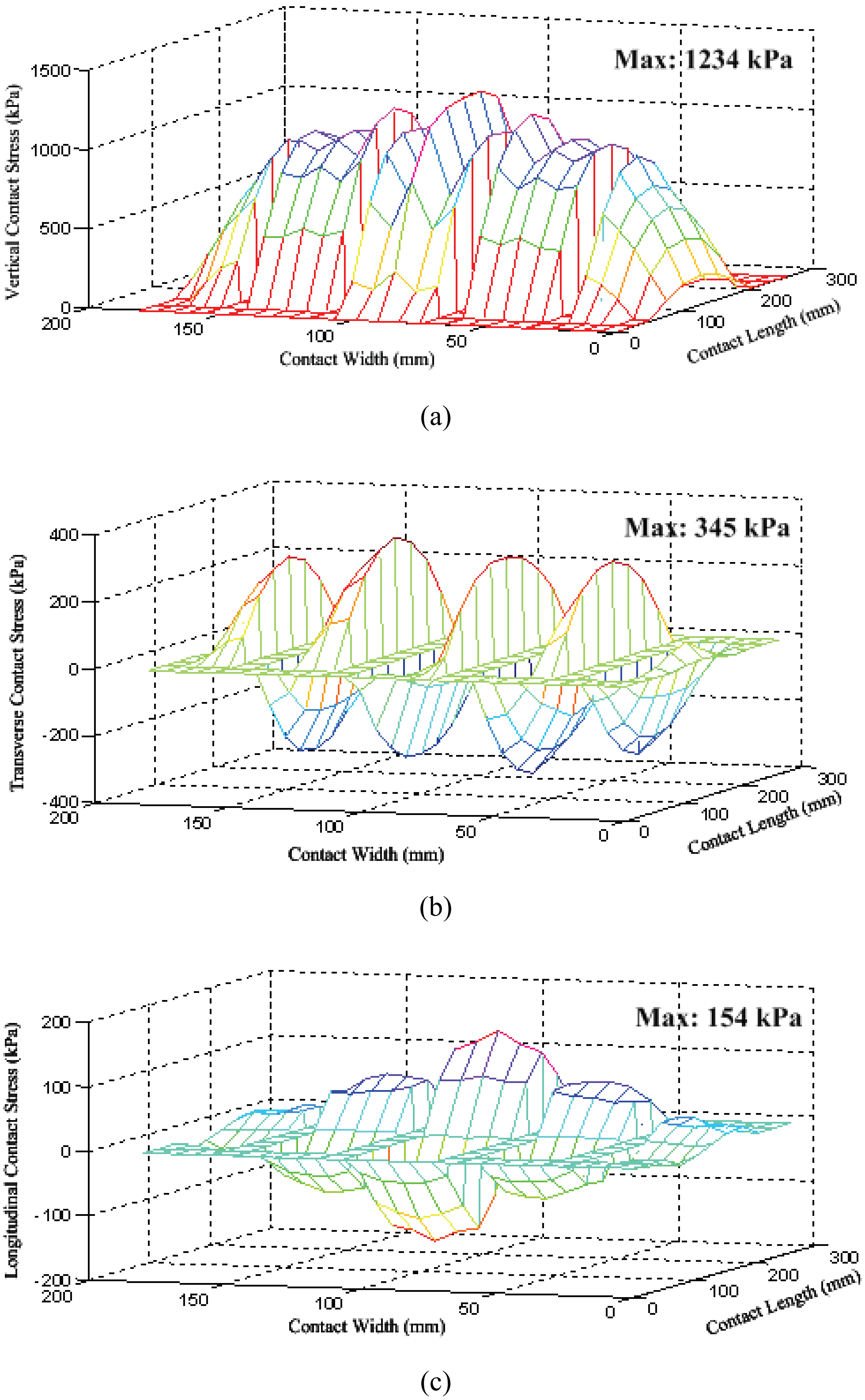

Figure 3.15 Predicted (a) vertical; (b) transverse; and (c) longitudinal contact stresses at static loading condition

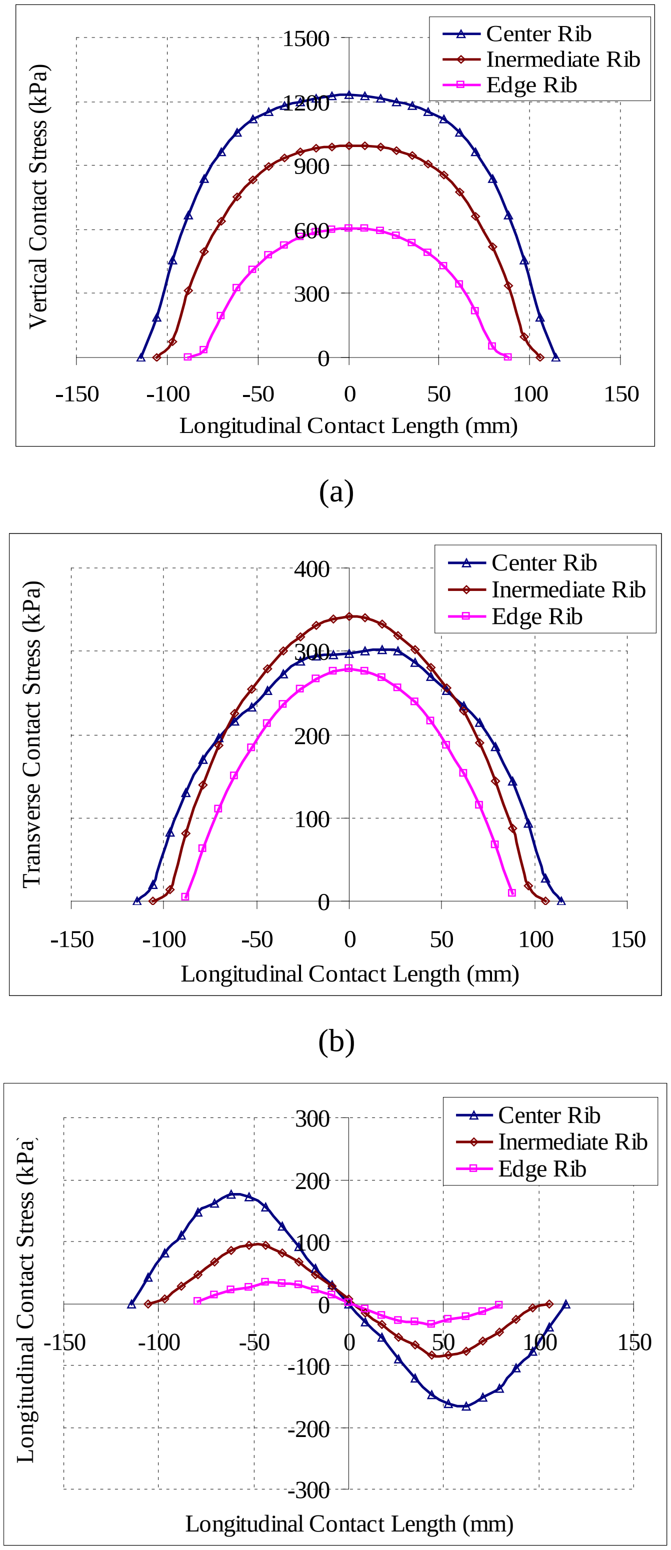

(a)

(b)

(c)

Figure 3.16 Predicted (a) vertical, (b) transverse, and (c) longitudinal contact stress distributions along contact length at static loading condition

Curve fitting techniques were applied to derive a polynomial function to estimate the interface contact stress distribution as a function of location and peak contact stress. It was discovered that the convex shape of vertical and transverse contact stress along the contact patch could be simulated using the elliptic function (Equation 3-8), while the reverse distribution of longitudinal contact stress from the entrance to the exit along the contact patch could be simulated using the sinusoid function (Equation 3-9).

$$q = q_{peak} \cdot \sqrt{1-(x/L)^2} \tag{3-8}$$

$$q = -q_{peak} \cdot \sin(\pi \cdot x/L) \tag{3-9}$$

where q is contact stress at location x ($-L \le x \le L$); q_{peak} is peak contact stress at each rib along contact length; and L is longitudinal contact length.

3.5 Tire Contact Stresses at Various Load and Tire Inflation Pressure Levels

Figures 3.17 and 3.18 show the distributions of 3-D tire contact stresses, respectively under high load (40.2kN) and high tire inflation pressure (966kPa). The results show that as the load increases, the peak contact stress tends to shift towards outer ribs and the convex shape of the vertical stress tends to flatten in the middle section. This trend likely occurs due to bending deformation of the sidewall caused by heavy load. This mainly affects the contact stresses under the outside ribs. As the tire inflation pressure increases, the stiffness of the whole tire structure increases, especially the central part of the tread area. Therefore, the vertical contact stress increases the most in the center of the tire contact area and the stress non-uniformity along the tire contact width becomes more significant.

The contact length and contact area increases as the load increases but decreases as the tire inflation pressure increases. It was found that the increase in contact length is more significant than the increase in contact width due to the relatively high lateral tire stiffness. The changing trends of tire contact stresses and contact areas as the load or inflation pressure increases are consistent with the observations from experimental measurements (De Beer et al. 1997; Douglas et al. 2000; Wang and Al-Qadi 2009).

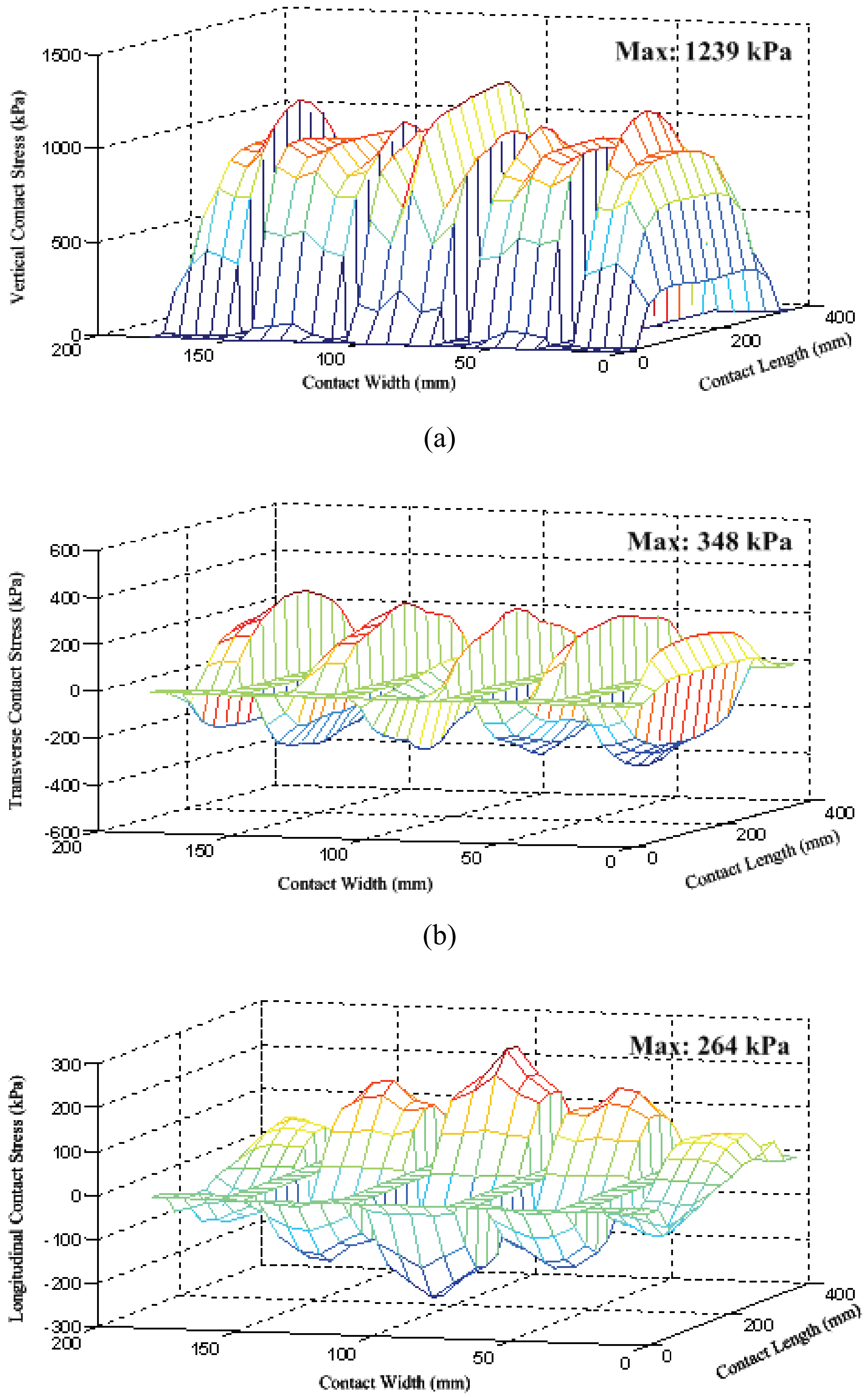

(a)

(b)

(c)

Figure 3.17 Predicted (a) vertical; (b) transverse; and (c) longitudinal contact stresses under heavy load (40.2kN) at static loading condition

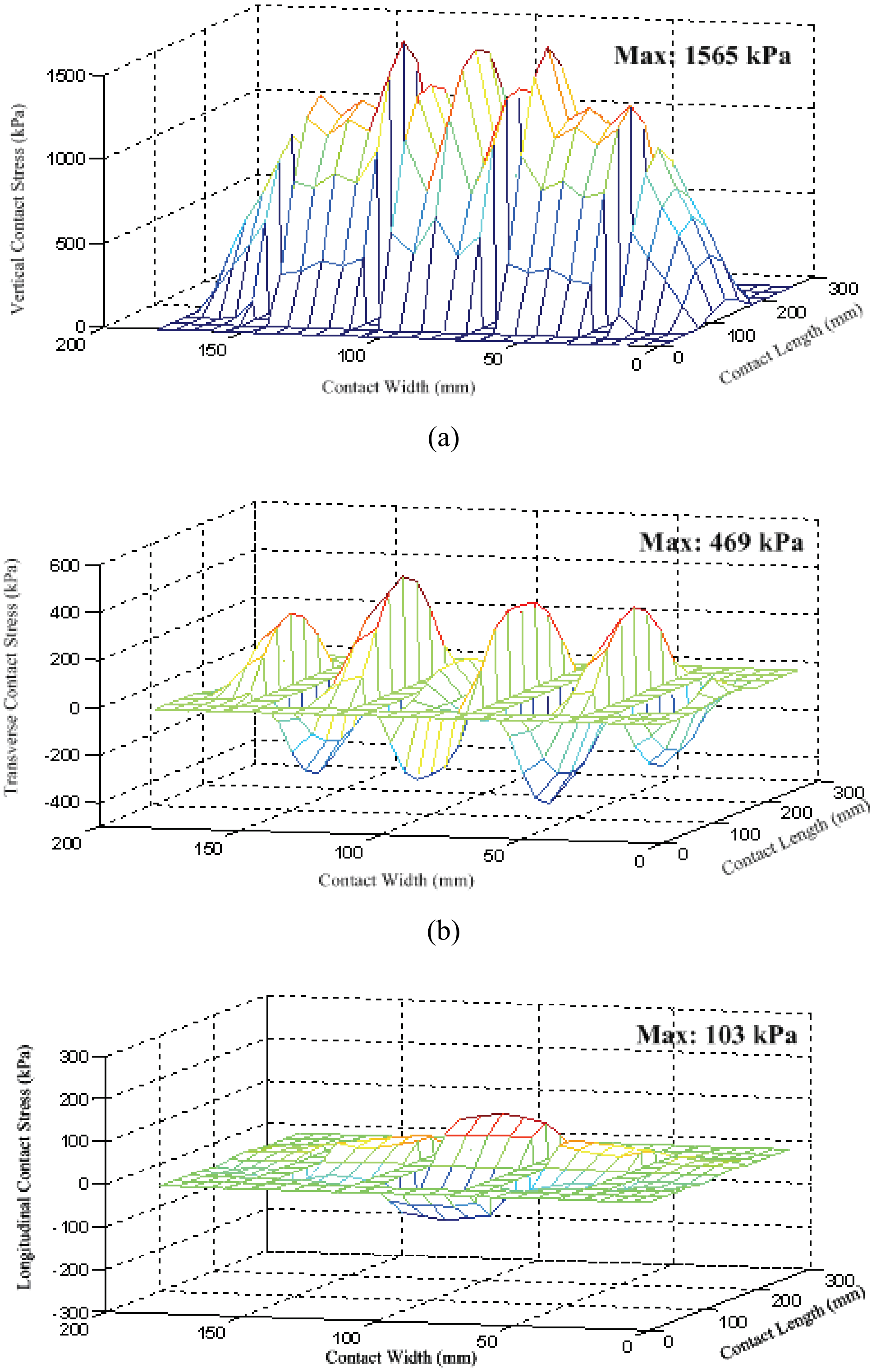

(a)

(b)

(c)

Figure 3.18 Predicted (a) vertical; (b) transverse; and (c) longitudinal contact stresses at high inflation pressure (966kPa) at static loading condition

To study the relationship between the contact stresses and the levels of load and tire inflation pressure, 30 loading cases were run using the developed tire-pavement interaction model with various combinations of load and tire inflation pressure. The applied wheel load on one tire varied between 17.8kN and 40.2kN, and the tire inflation pressure varied from 414kPa to 966kPa. This range was selected based on the distribution of axle load and tire inflation pressure for normal traffic. It is noted that after AASHO road test, bias-ply tires have largely been replaced by radial-ply tires on heavy trucks and the average inflation pressure has increased from 550kPa to 690 to 760kPa.

The statistical summary of the maximum contact stresses in three directions under various loads and tire inflation pressures is presented in Table 3.3. The wide range of contact stresses in three directions indicates that the contact stresses are significantly affected by the applied load and tire inflation pressures. On average, the stress ratio of the maximum contact stresses at three directions (vertical, transverse, longitudinal) is approximately 1:0.28:0.17. These observations indicate that, instead of the conventional uniform contact stress assumption within circular contact area, the realistic tire-pavement contact stress distributions should be considered when evaluating the pavement responses under truck loading at various loads or tire inflation pressures.

Table 3.3 Summary of Contact Stresses under Various Loads and Tire Inflation Pressures

Load (kN)	Pressure (kPa)	Maximum contact stress	Range (kPa)	Average (kPa)	Standard deviation (kPa)
17.8-40.2	414-966	Vertical	854-1633	1220	264
		Transverse	194-490	339	100
		Longitudinal	103-306	214	50
		Stress ratio at three directions (vertical: transverse: longitudinal)	1:0.23:0.07-1:0.31:0.30	1:0.28:0.17	N/A

Figure 3.19 shows the peak vertical contact stresses under various loads and tire inflation pressures under center, intermediate, and edge ribs, respectively. The results show that the vertical contact stresses under the center and intermediate ribs are mainly affected by the tire inflation pressure and relatively independent of the load. The vertical contact stress under the edge rib is mainly affected by the load but the effect of tire

inflation pressure becomes more significant as the load increases. Figure 3.20 shows the peak transverse contact stresses under various loads and tire inflation pressures under center, intermediate, and edge ribs, respectively. The changing trend of transverse contact stress is similar to the vertical contact stresses as the load or tire inflation pressure increases. However, this is not the case for the longitudinal contact stresses. As shown in Figure 3.21, the longitudinal contact stresses increase as the load increases; but decreases slightly as the tire inflation pressure increases (except for the longitudinal contact stresses at center and intermediate ribs when the tire inflation pressure is 414kPa).

A bilinear function was used to quantify the relationship between the peak contact stresses at each rib and the tire inflation pressures and loads, as shown in Equation 3-10. The detailed regression equations and their R-squares are presented in Table 3.4. Therefore, the contact stress distribution at each rib under various loads and tire inflation pressures can be estimated using Equations 3-8, 3-9, and 3-10 together.

$$q_{peak} = k_0 + k_1 \cdot p + k_2 \cdot P \tag{3-10}$$

where q_{peak} is the peak contact stress at each rib along contact length; p is tire inflation pressure; P is the applied load on tire; and k_0, k_1, and k_2 are parameters generated by least-square regression.

Table 3.4 Regression Equations between Peak Contact Stresses and Loads and Tire Inflation Pressures

Peak contact stress	Rib	Regression equation	R-square
Vertical	Center	$q_{peak} = 317 + 1.23p + 1.35P$	0.99
	Intermediate	$q_{peak} = 100 + 1.20p + 1.27P$	0.99
	Edge	$q_{peak} = 12 + 0.48p + 14.84P$	0.88
Transverse	Center	$q_{peak} = 58 + 0.31p + 0.69P$	0.99
	Intermediate	$q_{peak} = -32 + 0.56p + 0.82P$	0.99
	Edge	$q_{peak} = -121 + 0.10p + 6.71P$	0.95
Longitudinal	Center	$q_{peak} = 224 - 0.018p + 3.87P$	0.87
	Intermediate	$q_{peak} = 124 - 0.12p + 3.33P$	0.95
	Edge	$q_{peak} = 56 - 0.11p + 2.98P$	0.97

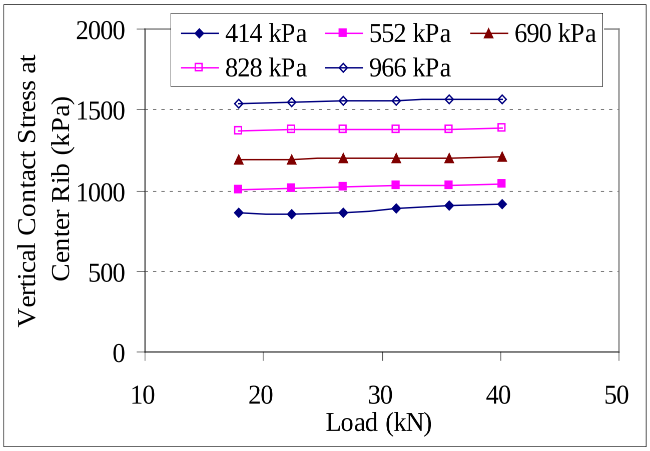

(a)

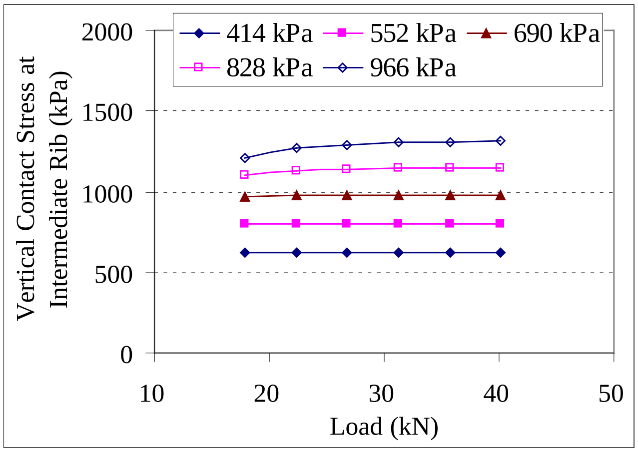

(b)

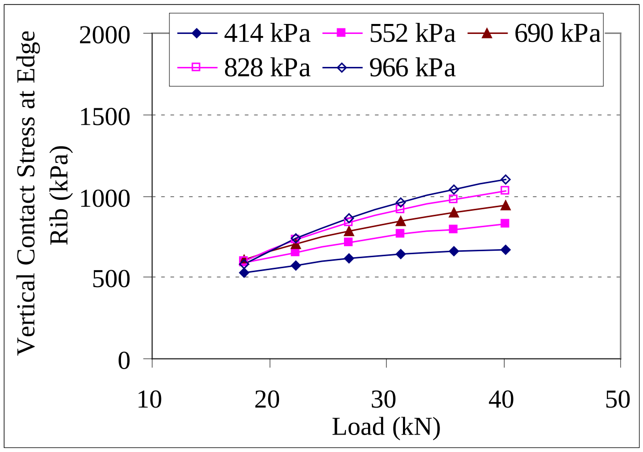

(c)

Figure 3.19 Peak vertical contact stresses under various loads and tire inflation pressures at the (a) center, (b) intermediate, and (c) edge ribs

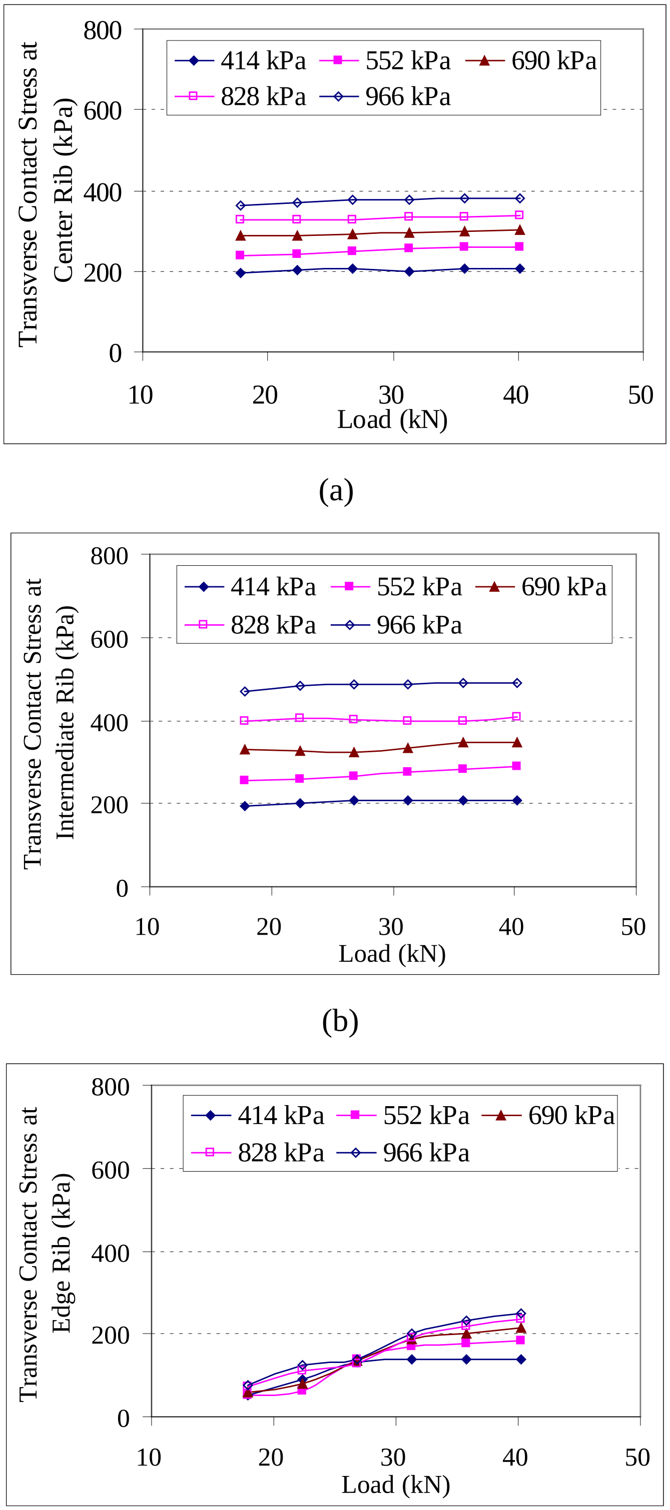

(a)

(b)

(c)

Figure 3.20 Peak transverse contact stresses under various loads and tire inflation pressures at the (a) center, (b) intermediate, and (c) edge ribs

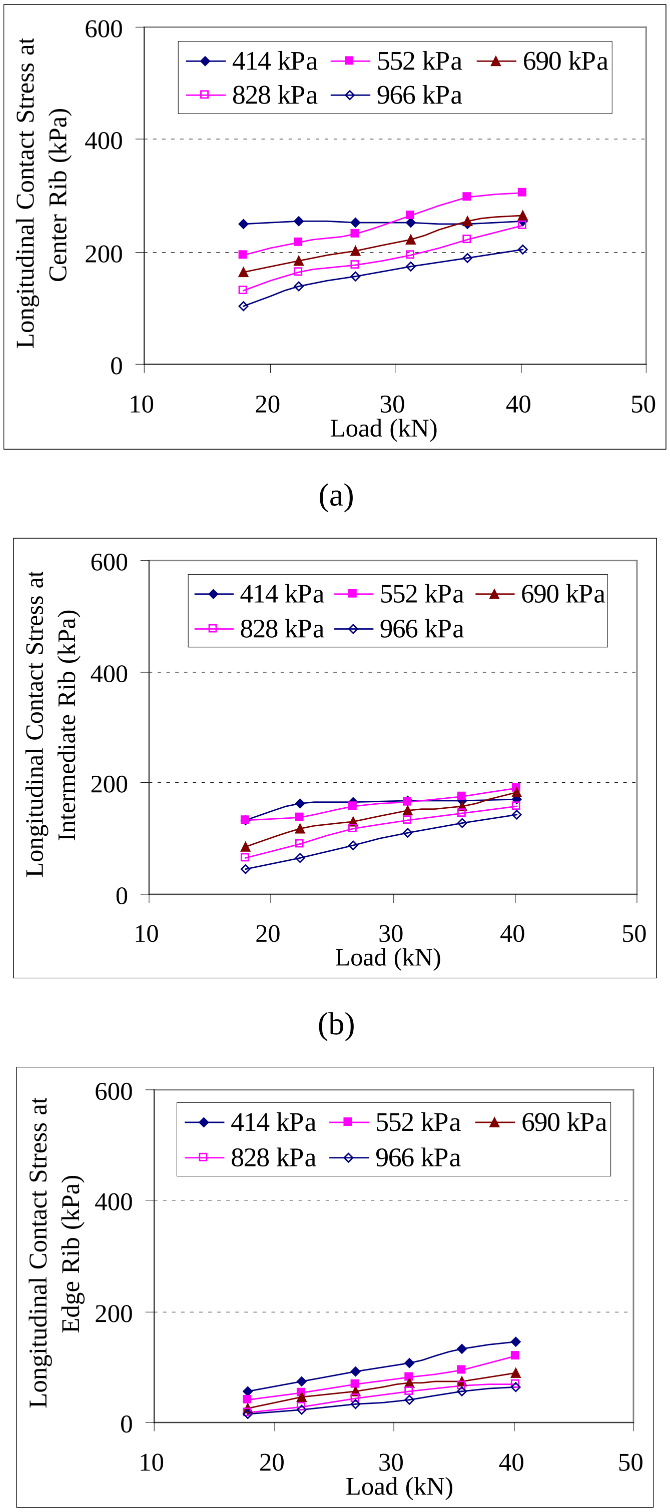

(a)

(b)

(c)

Figure 3.21 Peak longitudinal contact stresses under various loads and tire inflation pressures at the (a) center, (b) intermediate, and (c) edge ribs

In general, the calculation results indicate that the interaction of load and pressure on the contact stress distributions is significant and different combinations of tire load and inflation pressure may result in comparable peak stresses and similar stress distributions. This implies that different combinations of tire load and inflation pressure may cause the similar pavement damage and the pavement deterioration due to vehicle loading can be minimized through the optimized selection of tire load and inflation pressure.

3.6 Tire-Pavement Contact Stresses at Various Rolling Conditions

The tire-pavement contact stresses are affected by the tire rolling conditions (free rolling, acceleration, braking, or cornering). To simulate various tire rolling conditions, the steady-state transport analysis requires the transport velocity (v) and angular velocity (ω) to be specified separately. In all the analysis of contact stresses at various rolling conditions, the load on tire is 17.8kN and the tire inflation pressure is 724kPa.

3.6.1 Contact Stresses at Free Rolling Condition

At the free rolling condition, no additional driving/braking torque is applied on the tire, and the angular velocity is equal to the transport velocity divided by the free rolling radius. For a specific transport velocity, the angular velocity at the free rolling condition can be found through trials until the state that the longitudinal reaction forces (RF) acting on the tire from the pavement surface becomes zero. As shown in Figure 3.22, the free rolling angular velocity for the vehicle speed of 10km/h was found equal to 5.6rad/s. Consistent with the experimental findings reported by Tielking and Roberts (1987), the analysis results show that the effect of rolling speed on the contact stress distributions in the contact patch is insignificant.

Figures 3.23 (a), (b), and (c) show the predicted 3-D contact stresses at the tire-pavement interface at the free rolling condition (v=10km/h, w=5.6rad/s). It is expected that a rolling tire could induce local stress fields that differ from those at a static loading condition. Compared to static condition, free rolling conditions result in 10 to 20% less vertical contact stress except at the outermost edge of the contact area. Static and rolling tires experience different loading histories for a given contact point at the tire-pavement interface. Centrifugal forces of a rolling tire could result in tire diameter increase, which is restricted by the pavement surface. This could cause a vertical “axle lift” and a decrease in tire-pavement contact stresses. The transverse contact stresses at the free rolling condition are found to be much lower than those at static condition. As expected, when a tire is in free rolling condition, the longitudinal contact stresses (frictional forces) are negligible and therefore the tire has low rolling resistance at the free rolling condition.

This variation in contact stresses due to changes from static to rolling conditions is similar to the measurements reported by Pottinger (1992). Figure 3.24 shows the measured vertical, transverse, and longitudinal contact stresses of a static and slow rolling (75mm/sec) radial tire under 4.9-kN load and 200-kPa inflation pressure. Generally, the stress distributions at the static and free rolling conditions are similar. As the tire goes from static to rolling state, the stresses decrease in the middle of the footprint and increase at the boundaries of the footprint for both the vertical and longitudinal stresses; while the onset of tire rolling leads to a significant reduction in the transverse contact stresses.

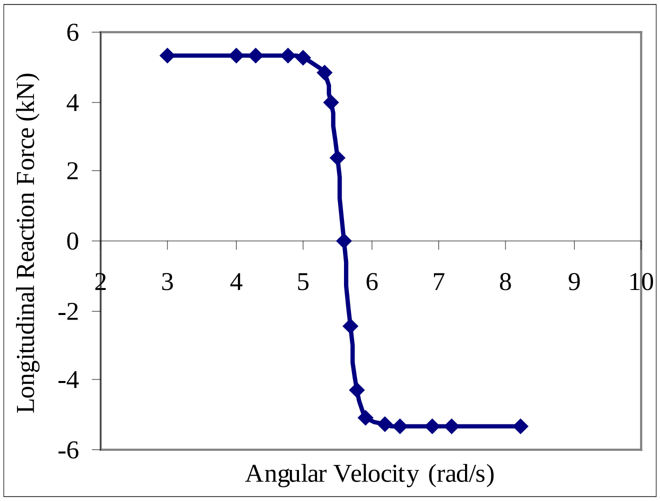

Figure 3.22 Longitudinal reaction force at various angular velocities for a specific transport velocity (10km/h)

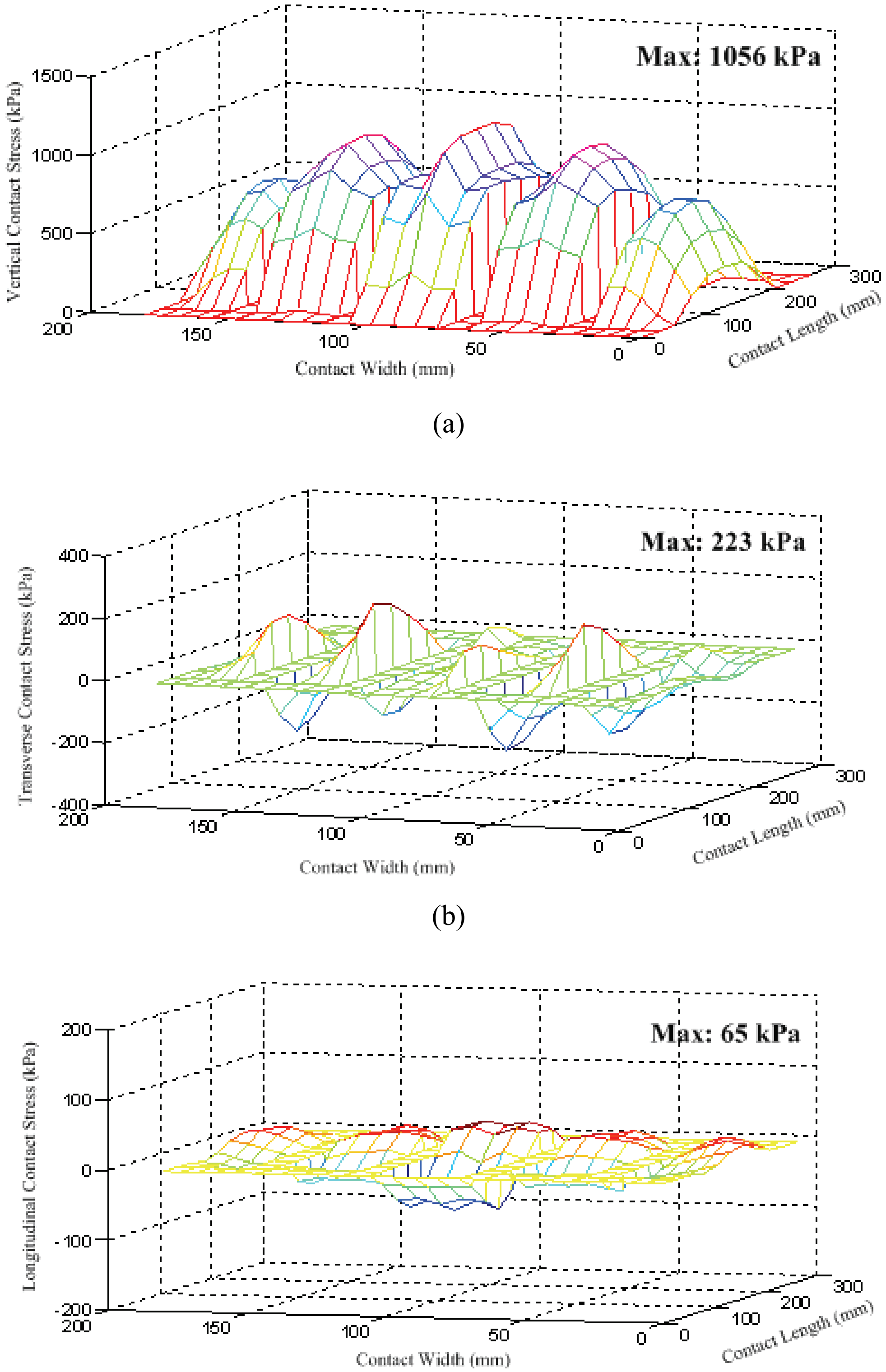

Figure 3.23 Predicted (a) vertical; (b) transverse; and (c) longitudinal contact stresses at the free rolling condition

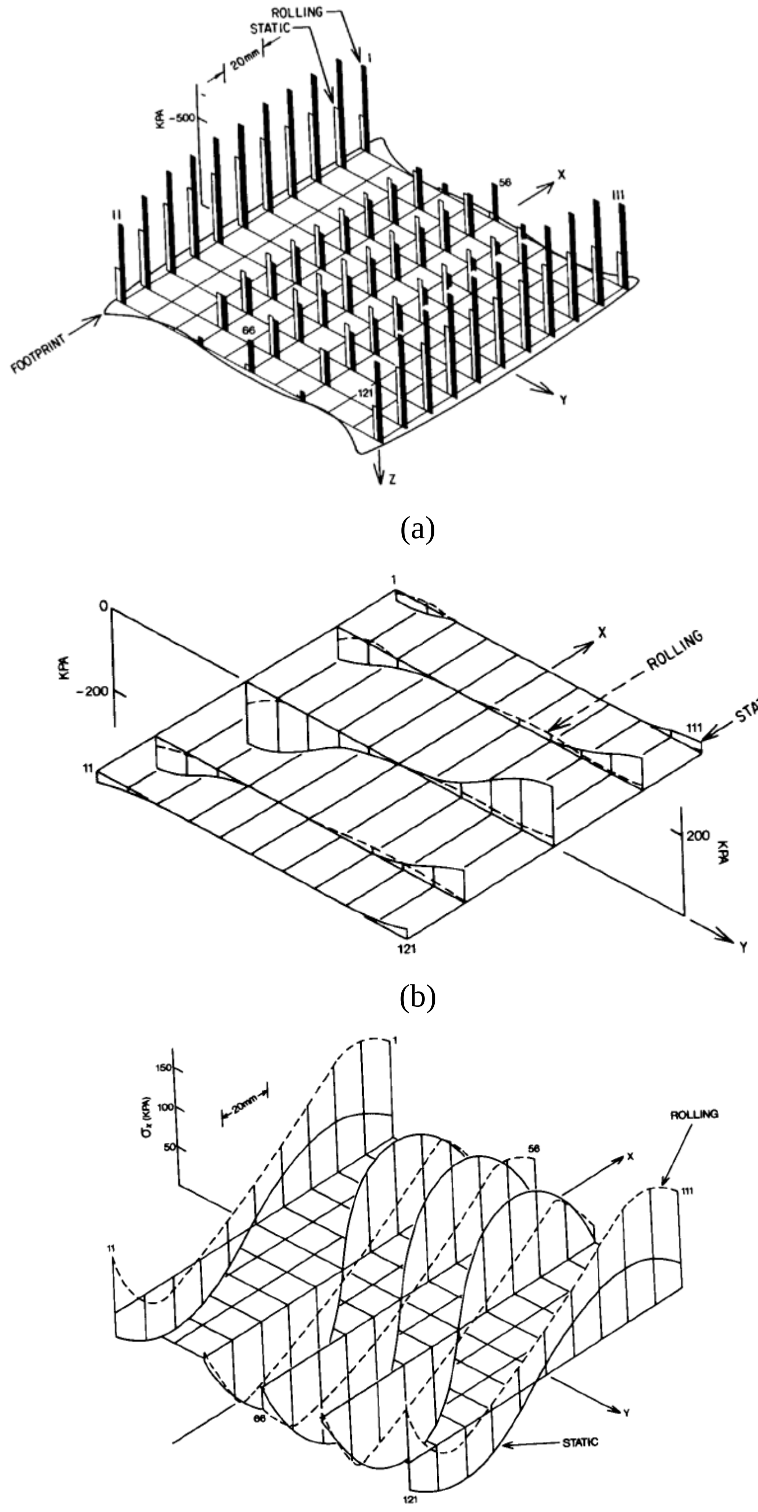

(a)

(b)

(c)

Figure 3.24 Measured (a) vertical; (b) transverse; and (c) longitudinal contact stresses at free rolling condition compared to static condition (after Pottinger 1992)

3.6.2 Contact Stresses at Braking Condition

During tire braking or acceleration, the angular velocity of a tire is slower or faster than the angular velocity at the free rolling condition due to the applied braking or driving torque on the tire (Figure 3.25). Partial braking occurs when the angular velocity of the tire is less than the angular velocity at the free rolling condition such that some of the contact points between the tire and the pavement are sliding. On the other hand, partial acceleration occurs when the angular velocity is greater than the angular velocity at the free rolling condition. Full braking or acceleration occurs at a very slow or fast angular velocity when all the contact points between the tire and the pavement are completely sliding in the backward or forward directions.

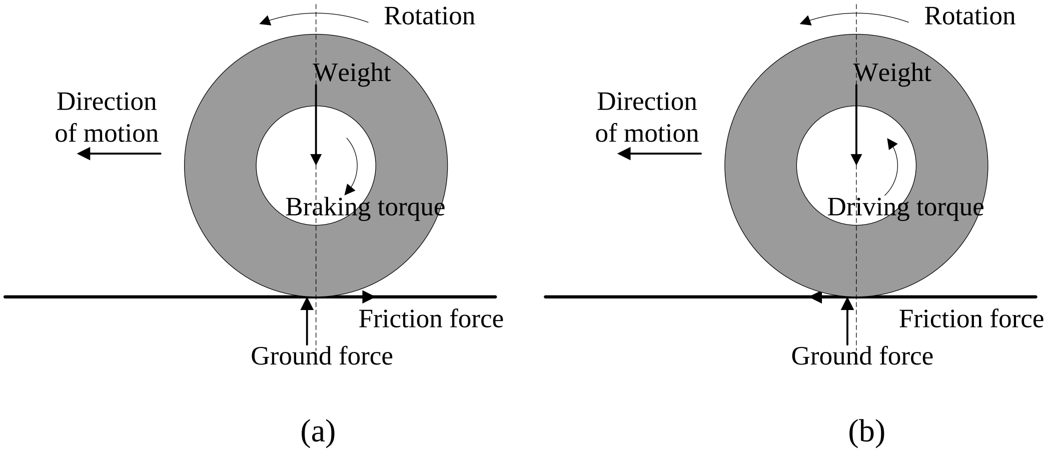

Figure 3.25 Illustrations of torques and forces at tire (a) braking and (b) accelerating

Figures 3.26 (a), (b), and (c) plot the predicted 3-D contact stresses at the tire-pavement interface at the full braking condition (v=10km/h, w=3rad/s). The effect of weight redistribution between different truck axles due to braking was not considered in the simulation at this point. Compared to the free rolling condition, tire braking causes negligible transverse contact stresses but similar vertical contact stresses and significant longitudinal contact stresses at the tire-pavement interface. Figure 3-26(c) clearly shows that tire braking induces one-directional longitudinal contact stresses when a tire is sliding on a pavement surface, and these stresses are much greater than the longitudinal contact stresses at the free rolling condition. The longitudinal contact stresses on a pavement surface during braking and acceleration have similar magnitudes but opposite directions with forward stresses at braking and backward stresses at acceleration. These longitudinal contact stresses may lead to severe pavement deterioration, such as shoving/corrugation and slippage cracking; especially at pavement intersections or longitudinal sloped pavements.

The level of braking/acceleration can be defined using the slip ratio, as shown in Equation 3-11 (Henry 2000). The slip ratio represents the locking status of a tire. For example, the slip ratio is zero when the tire is free rolling and the slip ratio is 100% when the tire is full braking. Figure 3.27 shows the longitudinal contact stress distributions along tire contact length due to tire braking at different slip ratios. It shows that the longitudinal contact stress increases as the slip ratio increases until the peak friction force is achieved at the full braking condition. For partial braking, the contact patch can be divided into two regions: a forward “stick” region in the entrance part and an aft “slide” region in the exit part. In the “slide” region, the longitudinal contact stresses on pavement surface are approximately equal to the vertical contact stresses multiplied by the friction coefficient. It indicates that as the tire is sliding at high slip ratios, the longitudinal contact stresses can be estimated from the vertical contact stresses and the pavement surface friction coefficient.

$$\text{Slip ratio} = \frac{v - \omega \cdot r}{v} \qquad (3\text{-}11)$$

where v is the vehicle travel speed ; ω is the angular velocity of the tire; and r is the rolling radius at the free rolling condition.

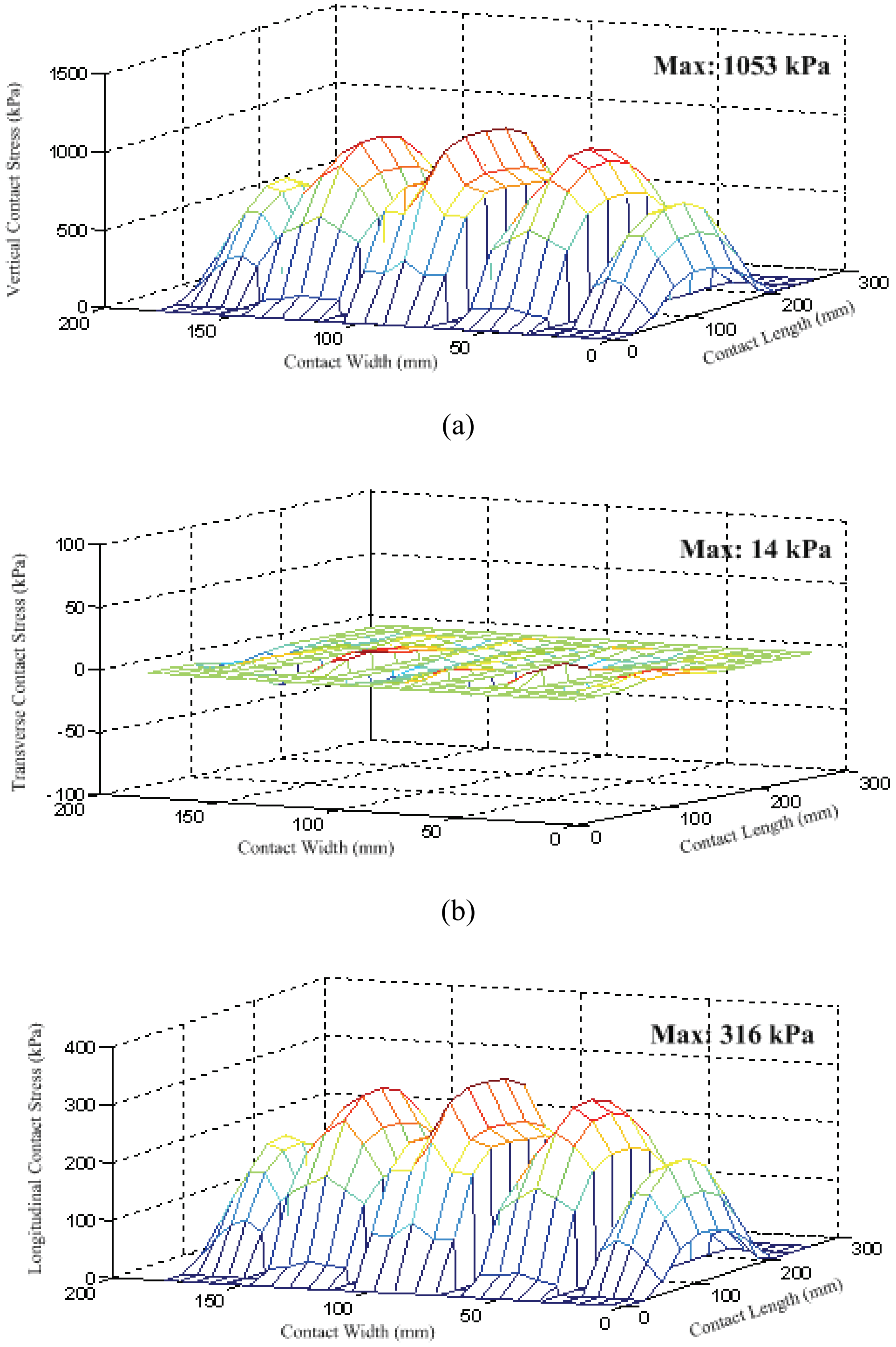

(a)

(b)

(c)

Figure 3.26 Predicted (a) vertical, (b) transverse, and (c) longitudinal tire-pavement contact stresses at the full braking condition

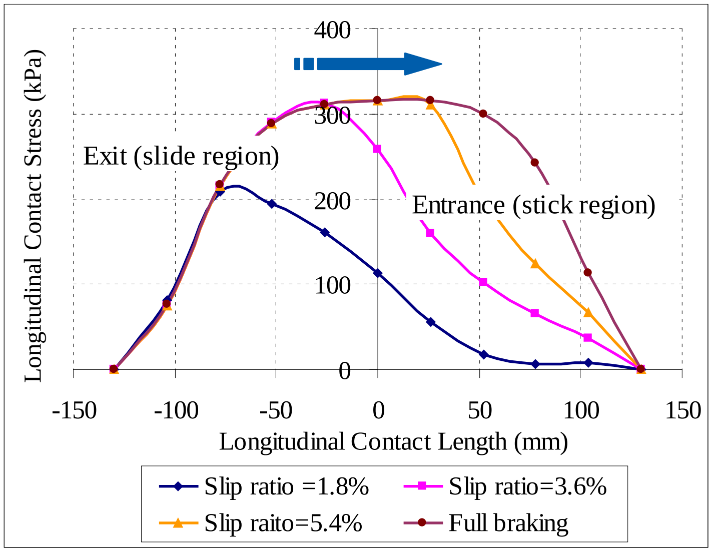

Figure 3.27 Longitudinal contact stress distributions at different slip ratios

3.6.3 Contact Stresses at Cornering Condition

As the tire is cornering, the friction between the tire and road surface restricts the lateral movement of the tire and results in lateral deformation of the tire tread elements within the contact patch while the wheel is steering away from the straight-ahead direction. Therefore, a slip angle is induced between a rolling tire's actual direction of motion and the pointing direction (Figure 3.28). The slip angle is a measurement of the extent the tire's contact patch has twisted (steered) in relation to the wheel.

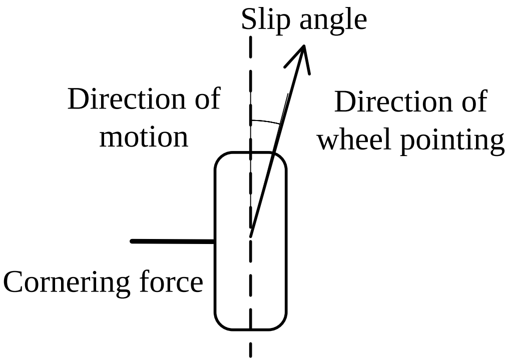

Figure 3.28 Illustrations of slip angle at tire cornering

Figures 3.29 (a), (b), and (c) show the predicted 3-D contact stress fields at the tire-pavement interface at the cornering condition (v=10km/h, free rolling, slip angle =1°). The results show that tire cornering causes concentration of contact stresses shifting toward to the right side of the contact patch, which lies on the inner side of the right turn. This indicates that the right tire shoulder is more compressed to the road surface than the left one during cornering. Hence, the contact stress distribution is no longer symmetric with respect to the center plane and the contact patch at the right side is longer than the one at the left side. Similar to the free rolling condition, the longitudinal contact stresses at the tire cornering condition are negligible. However, tire cornering causes greater vertical and transverse contact stresses compared to the free rolling condition; the peak contact stresses are concentrated locally at the edge of tire ribs. Localized contact stress concentration at tire cornering could be affected by the tread pattern of the tire (such as tread depth, tread profile, arrangement of ribs and grooves, etc).

Figures 3.30 (a) and (b) show the variation of maximum contact stresses with the slip angle at the cornering condition, respectively, for the vertical and transverse contact stresses. As the slip angle increases, the maximum contact stresses increase until the slip angle reaches 5° and then becomes relatively constant. It was found that the localized stress concentration became more significant as the slip angle increased. The relatively high vertical and transverse contact stresses at tire cornering could explain the accelerated pavement deterioration at the curved road sections where frequent vehicle turns occur. In addition, the high tangential contact stresses generated during vehicle turns would accelerate the polishing of surface aggregate and reduce surface friction.

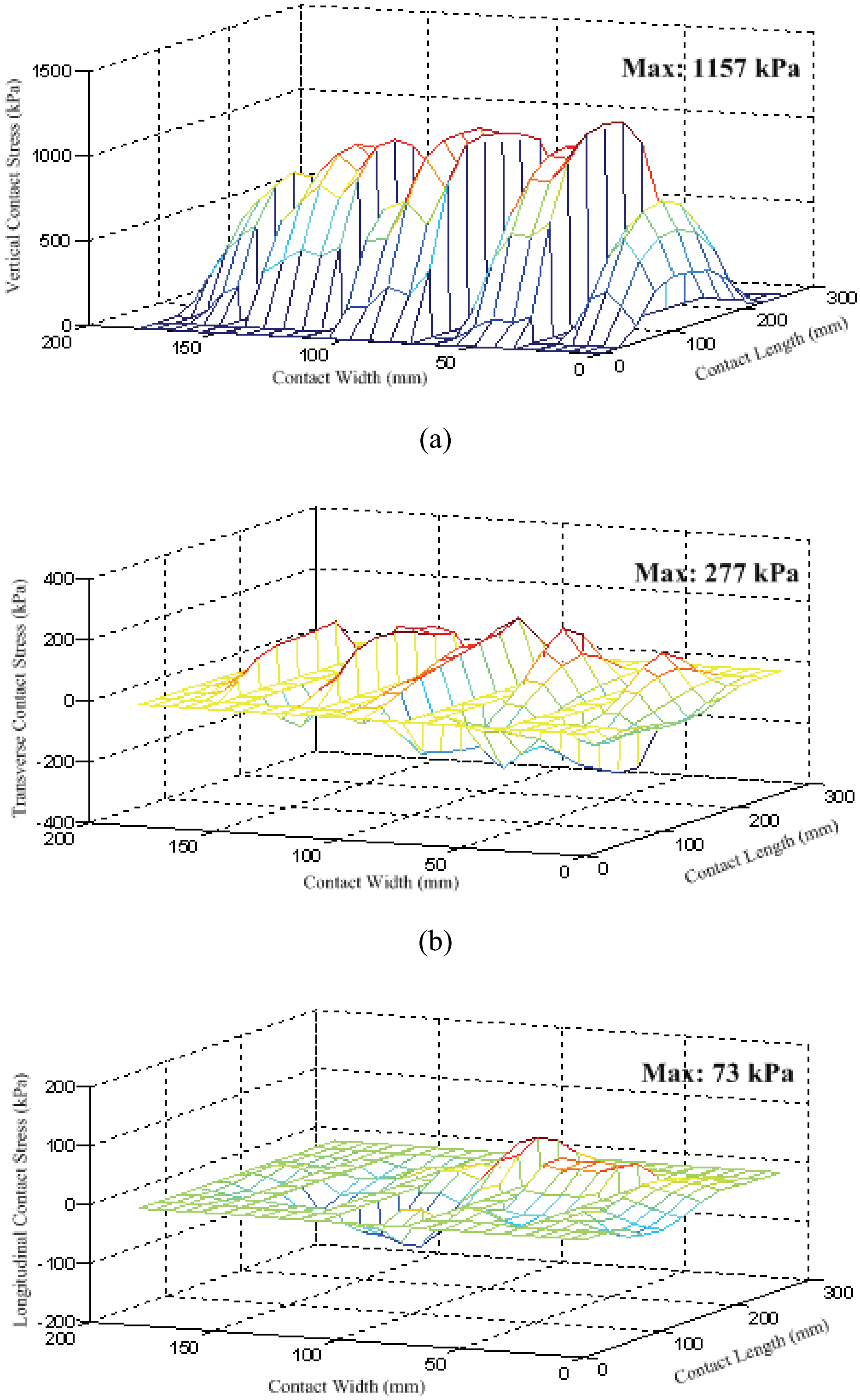

(a)

(b)

(c)

Figure 3.29 Predicted (a) vertical, (b) transverse, and (c) longitudinal tire-pavement contact stresses at cornering condition

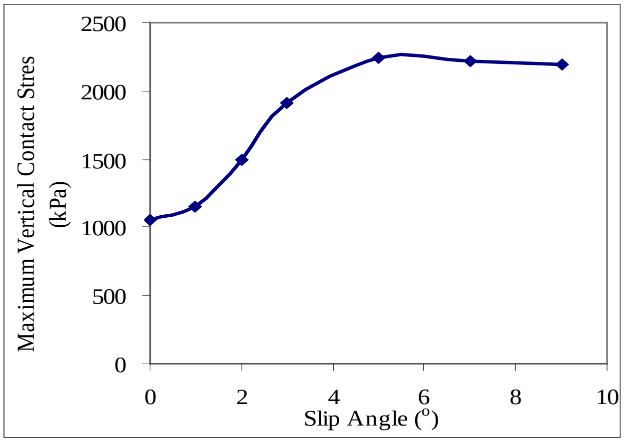

(a)

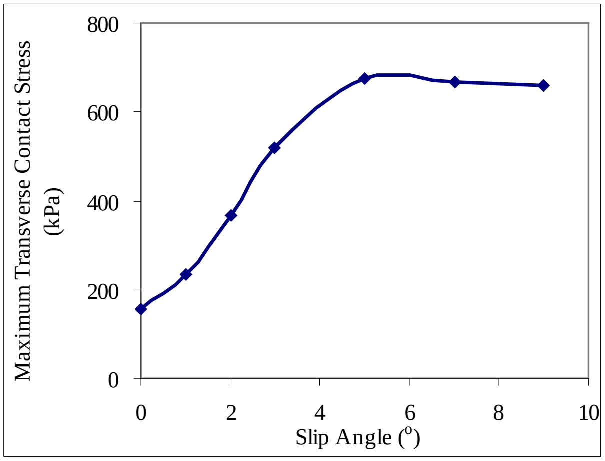

(b)

Figure 3.30 Predicted (a) vertical and (b) transverse contact stress with different slip angles at cornering condition

3.7 Effect of Pavement Surface Friction on Tire-Pavement Interaction

Tire-pavement contact stresses are affected by the friction condition at the tire-pavement interface. Table 3.5 summarizes the maximum contact stresses in three directions and the ratio of these maximum contact stresses at various rolling conditions (v=10km/h) when using different friction coefficients. The results show that when the tire is free rolling or full braking, the vertical contact stresses are kept relatively constant as the friction coefficient increases. However, the tangential contact stress increases as the friction coefficient increases, especially for the transverse contact stress at the free rolling condition and the longitudinal contact stresses at the braking/accelerating condition. Tangential contact stresses develop through shear mechanisms while a tire rolls on a road surface and therefore depends on the friction coupling at the tire-pavement interface. When the tire is cornering, the contact stresses in three directions all increase as the friction coefficient increases and the increase of vertical and transverse contact stresses is more significant than the increase of longitudinal contact stresses. This is probably because the tire deformation tends to be greater at one side of the contact patch during cornering as the allowed maximum friction force before sliding increases.

At the free rolling and cornering conditions, the ratios of tangential contact stresses relative to the vertical contact stresses are smaller than the friction coefficients. This indicates that no relative slippage occurs between the tire and pavement. However, at full braking, longitudinal contact stresses are equal to vertical contact stresses multiplied by friction coefficient since the tire is essentially sliding on the pavement surface.

Table 3.5 Maximum Contact Stresses with Different Friction Coefficients

Rolling Condition	Friction Coefficient	Maximum Contact Stresses (MPa)			Maximum Stress Ratio
		Vertical	Transverse	Longitudinal	
Free Rolling	$\mu = 0.3$	1056	223	65	1:0.21:0.06
	$\mu = 0.5$	1051	309	73	1:0.29:0.07
	$\mu = 0.8$	1067	391	81	1:0.37:0.08
Full Braking	$\mu = 0.3$	1053	14	316	1:0.02:0.30
	$\mu = 0.5$	1099	38	549	1:0.03:0.50
	$\mu = 0.8$	1144	73	915	1:0.06:0.80
Cornering (slip angle =1°)	$\mu = 0.3$	1157	277	73	1:0.24:0.06
	$\mu = 0.5$	1302	401	85	1:0.31:0.07
	$\mu = 0.8$	1432	485	95	1:0.34:0.07

Experiments have found that, for a rubber tire sliding on pavement surface, the friction between the tire and pavement surface is not constant and is strongly dependent on vehicle speed and slip ratio. In this study, the effect of the sliding-velocity-dependent friction coefficient on the contact behavior at the tire-pavement interface is examined. As shown in Equation 3-12, the friction coefficient is modeled as an exponential function of sliding velocity (Oden and Martins, 1985). This equation defined a smooth transition from a static to a kinetic friction coefficient in terms of an exponential curve.

$$\mu = \mu_k + (\mu_s - \mu_k)e^{-\alpha \cdot s} \tag{3-12}$$

where μ_k is kinetic coefficient at the highest sliding velocity; μ_s is static coefficient at the onset of sliding (zero sliding velocity); α is user-defined decay coefficient; and s is sliding velocity (slip rate).

For the contact between the rubber tire and pavement surface, the static friction coefficient is more related to the surface micro-texture, while the decay coefficient is highly dependent on surface macro-texture (Henry 2000). Micro-texture refers to the fine-scale texture contributed by individual aggregate particles whereas macro-texture is mainly controlled by aggregate gradation and mix design. In this study, the static friction coefficient was set as 0.3 for the reason of comparing the contact stresses between the constant friction model and the sliding-velocity-dependent friction model. This number represents the friction of the pavement surface condition with relatively poor micro-texture. Two different values of decay coefficients (0.05 and 0.5) were used to represent the friction characteristics of pavement surface with good and poor macro-texture, respectively (Figure 3.31).

Table 3.6 summarizes the maximum contact stresses in three directions and the ratio of these maximum contact stresses at various rolling conditions when using different friction models (v =10km/h). The tire-pavement contact stresses at the free rolling condition or at the cornering condition are not affected by the sliding-velocity-dependent friction model, because nearly no slip is induced at the tire-pavement interface when the tire is pure rolling or cornering at small slip angles. This indicates that it is reasonable to use constant static friction coefficient when predicting tire-pavement contact stresses at free rolling condition or at cornering condition with small slip angles. However, using the constant friction model may overestimate peak longitudinal contact stresses when the tire is sliding at the full braking condition, because constant friction model cannot simulate the decay of friction coefficient as slip speed increases.

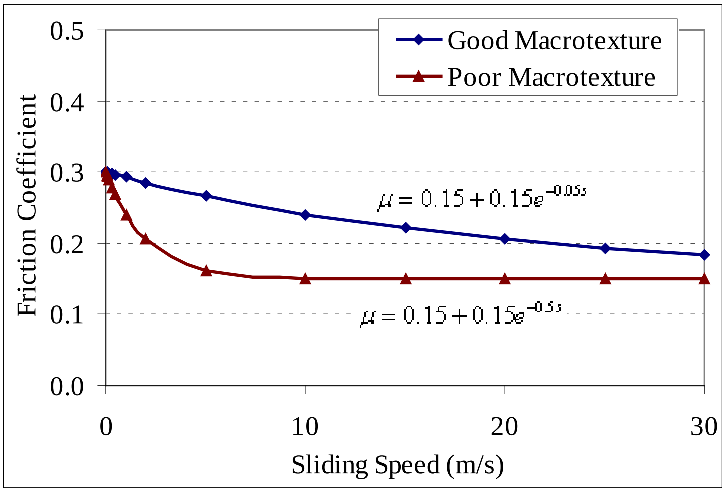

Figure 3.31 Sliding-velocity-dependent friction models

Table 3.6 Maximum Contact Stresses with Different Friction Models

Rolling Condition	Friction Model	Maximum Contact Stresses (MPa)			Maximum Stress Ratio
		Vertical	Transverse	Longitudinal	
Free Rolling	$\mu = 0.3$	1056	223	65	1:0.21:0.06
	$\mu = 0.15 + 0.15e^{-0.05s}$	1056	223	65	1:0.21:0.06
	$\mu = 0.15 + 0.15e^{-0.5s}$	1056	223	65	1:0.21:0.06
Full Braking	$\mu = 0.3$	1053	19	316	1:0.02:0.30
	$\mu = 0.15 + 0.15e^{-0.05s}$	1052	14	306	1:0.01:0.29
	$\mu = 0.15 + 0.15e^{-0.5s}$	1051	10	240	1:0.01:0.23
Cornering (slip angle =1°)	$\mu = 0.3$	1157	277	73	1:0.24:0.06
	$\mu = 0.15 + 0.15e^{-0.05s}$	1157	276	73	1:0.23:0.06
	$\mu = 0.15 + 0.15e^{-0.5s}$	1153	272	73	1:0.23:0.06

In vehicle dynamics, the tangential force developed at the tire-pavement interface as the vehicle is maneuvering is important for stability control. Figure 3.32 plots the calculated longitudinal friction force that acts on the tire during braking at different slip ratios. The general trend shows that the friction force reaches its maximum when the slip ratio is around 10% (critical slip ratio). As the slip ratio is lower than the critical slip ratio, the state of contact is partial slip; while as the slip ratio is greater than the critical slip ratio, the state of contact is full slip. When the tire is at full slip, the value of the maximum frictional force is equal to the normal force applied on the tire multiplied by the friction coefficient.

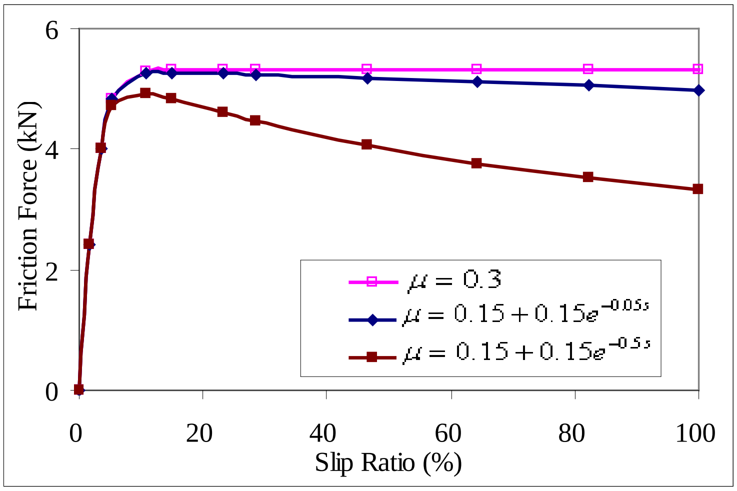

Figure 3.32 Friction forces due to tire braking using different friction models

It was found that when the tire was at partial slip, the calculated friction forces were approximately the same when using the constant and the sliding-velocity-dependent friction models. However, different trends were observed as the tire was at full slip. For the constant friction coefficient model, friction force remains constant as the slip ratio is greater than the critical slip ratio. On the other hand, the friction force decreases as the slip ratio increases when the sliding-velocity-dependent friction model was used. The development trend of friction force using the slide-velocity-dependent model is more consistent with the measured skid resistance during the tire braking process, as indicated in the Rado model (Henry 2000). In addition, it was found that using the constant friction model could overestimate the maximum friction force at the critical slip ratio. This is particularly important for the vehicles with an anti-lock braking system (ABS) because the brakes are controlled on and off repeatedly such that friction force is held near the peak.

Figure 3.33 shows the cornering forces that act on the tire during cornering at various slip angles. The cornering force (side friction force) is induced on the tire due to the tread slip at lateral direction when the vehicle is steering, which is parallel to the road surface and at an angle with the moving direction of the wheel. The results show that the cornering force increases approximately linearly for the first few degrees of slip angle, and then increases non-linearly to its peak value at the slip angle of around 5° and then stays relatively constant. The relationship between the cornering forces and the slip angles strongly affects the directional control and stability of the vehicle. The development trend of the cornering force is consistent with the experimental results in the literature (Wong 2002).

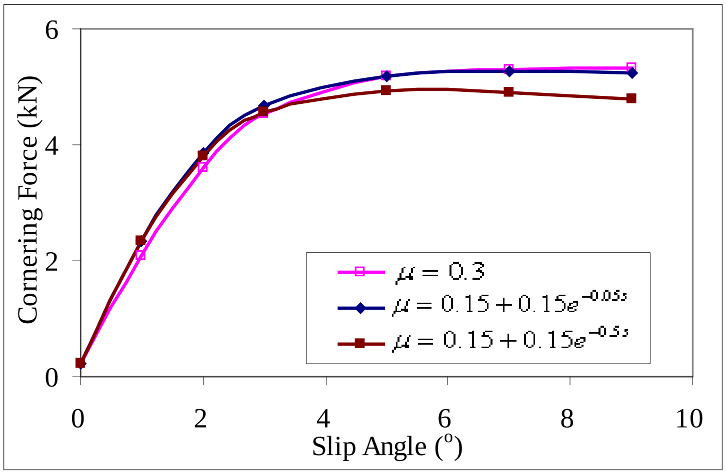

Figure 3.33 Cornering force using different friction models

At low slip angles there is little to no slip in the contact area, thus the cornering force is not affected by the friction model. As the tire reaches higher slip angles, the slip occurs in the contact area where the lateral force approaches the available friction force. After the slip occurs, the global lateral force is dominated by the maximum friction force. Thus, the predicted cornering forces at high slip angles using the sliding-velocity-dependent friction model are slightly smaller than those predicted using the constant friction model.

3.8 Summary

In this chapter, an air-inflated 3-D tire model was built and the interaction between a tire and a non-deformable pavement surface was simulated. The tire was modeled as a composite structure including rubber and reinforcement. The material parameters of each tire component were calibrated through the measured tire load-deflection curves. The steady-state tire rolling process was simulated using an Arbitrary Lagrangian Eulerian (ALE) formulation. The model results are consistent with measured values and validate the non-uniformity vertical contact stresses and localized tangential contact stresses at the tire-pavement interface.

The developed tire-pavement interaction model shows the potential to evaluate the mechanism of load distribution at the tire-pavement interface under various tire loading and rolling conditions. The model results show that the load primarily affects the vertical contact stresses, at the edge of tire contact area, and the longitudinal contact stresses. The tire inflation pressure, on the other hand, primarily controls the vertical contact stresses, at the center of tire contact area, and the transverse contact stresses. A statistical model is developed to predict peak contact stresses at each tire rib under various load and tire inflation pressure levels. In addition, vehicle maneuvering behavior significantly affects the magnitudes and distributions of tire-pavement contact stresses. For example, tire braking/acceleration induces significant longitudinal contact stresses, while tire cornering causes greater vertical and transverse contact stresses shifting toward one side of the contact patch. The tire-pavement contact stresses at various tire rolling conditions are significantly affected by the friction at the tire-pavement interface and vehicle operating parameters, such as slip ratio and slip angle.

CHAPTER 4 FINITE ELEMENT MODELING OF FLEXIBLE PAVEMENT

4.1 Building an FE Model of Flexible Pavement

A 3-D FE model of flexible pavement was simulated using the software ABAQUS. The 3-D FE model is more appropriate, compared to an axisymmetric or 2-D plane model. It allows considering 3-D contact stress distributions at the tire-pavement interface and dynamic transient loading associated with a moving vehicle.

Since the behavior of a layered pavement system may not be approximated using truss, beam, or shell elements, 3-D continuum solid elements are often used. In this study, the eight-node, linear brick elements with reduced integration were used in the finite domains, whereas infinite elements were used to reduce a large number of far-field elements without significant loss of accuracy and to create a “silent” boundary for the dynamic analysis (Figure 4.1). The infinite element has a special shape function for the geometry at the infinite boundary and thus has zero displacement as the coordinate approaches infinity.

The infinite elements provided in ABAQUS introduce additional normal and shear tractions (viscous damping boundary) on the FE boundary that are proportional to the normal and shear components of the velocity of the boundary, as shown in Equations 4-1 and 4-2 (Lysmer and Kuhlemeyer 1969; ABAQUS 2007). This could minimize the reflection of dilatational and shear wave energy back into the FE mesh and it usually provides acceptable results for most practical cases.

$$\sigma = \rho \cdot c_p \cdot \dot{u} \tag{4-1}$$

$$\tau = \rho \cdot c_s \cdot \dot{v} \tag{4-2}$$

$$\text{with } c_p = \sqrt{\frac{(1-\nu)E}{(1-2\nu)(1+\nu)\rho}} \text{ and } c_s = \sqrt{\frac{E}{2(1+\nu)\rho}}$$

where σ and τ are normal and shear stresses along the finite/infinite elements border, respectively; ρ is material density; c_p and c_s are longitudinal and shear wave velocities, respectively; $\dot{u}$ and $\dot{v}$ are velocities in the normal and tangential directions, respectively; E is the modulus of elasticity; and ν is the Poisson’s ratio.

Figure 4.1 illustrates the 3-D FE model that discretizes the pavement structure. The FE mesh is refined around the loading area along the wheel path; a relatively coarse mesh is used far away from the loading area. The element horizontal dimensions along the vehicle loading area were dictated by the tire rib and groove geometries. Hence, the length of elements within the loading area was selected at 15-18mm in the transverse direction and 20mm in the longitudinal (traffic) direction to have good aspect ratios. Based on a mesh convergence study conducted by Yoo and Al-Qadi (2008), the element thicknesses were selected to be 9.5mm for the asphalt surface layer and 20 to 30mm for the asphalt or aggregate base layers in order to have a smooth stress transition between elements.

In the dynamic analysis, the selection of element dimensions is also dependent on the wavelength of propagated stress waves. Elements having relatively large dimensions filter high frequencies, whereas elements having relatively small element dimensions can introduce numerical instability as well as require considerable computational resources. To obtain accurate results, it is recommended that the maximum element size should not exceed 1/12 the minimum wavelength of elastic waves propagating in the structure (Lysmer and Kuhlemeyer 1969). Because the stress wave velocity in flexible pavement structure is around 100-600m/sec and the vehicle loading frequency could be around 0.1-25Hz, the selected element size in the region of interest is much smaller than the requirement.

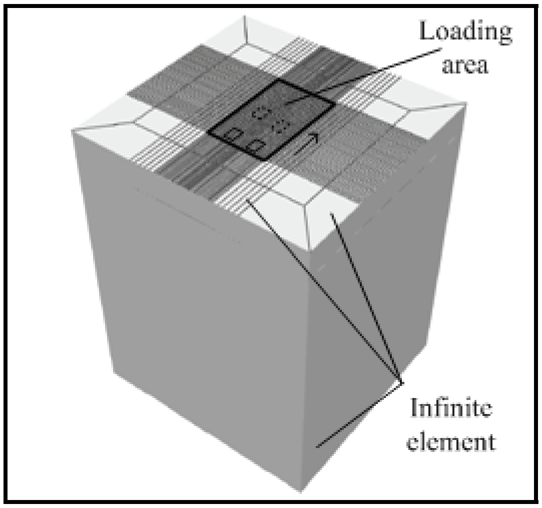

Figure 4.1 Illustration of the developed 3-D FE model

Duncan et al. (1968) have reported that reasonable pavement responses were obtained when the analysis boundary moved to 50 times the radius of circular loading area (R) in the vertical direction and 12 times R in the horizontal direction. In this study, a sensitivity analysis was performed to define the infinite boundaries at both sides, as well as the bottom of FE mesh (Figure 4.2). After comparing the maximum tensile and shear strains in the asphalt layer, the locations of the infinite boundary in three directions from the load center needed to be greater than 1.2m in order to obtain the stable solutions (less than 5% changes). The final selected domain size (finite + infinite) has an in-plane dimension of 2.1×2.1m and a vertical dimension of 2.5m to achieve the balance between computation cost and accuracy.

To check the mesh and boundary conditions, the FE solutions were compared with an analytical solution through a layered elastic theory based on simple assumptions (e.g., static loading, fully-bonded interface conditions, uniform circular contact stress, and linear elastic material behavior). Figures 4.3 (a) and (b) show the comparison between FE and multilayer elastic close-form solutions (from BISAR) for a 154-mm asphalt pavement under 44.4-kN dual-tire assembly loading at 720-kPa tire inflation pressure, respectively, for compressive stresses and longitudinal tensile strains. Good agreements were achieved between the predicted stresses and strains using the two aforementioned approaches. This indicates that the mesh refinement and boundary conditions of the FE model are appropriate.

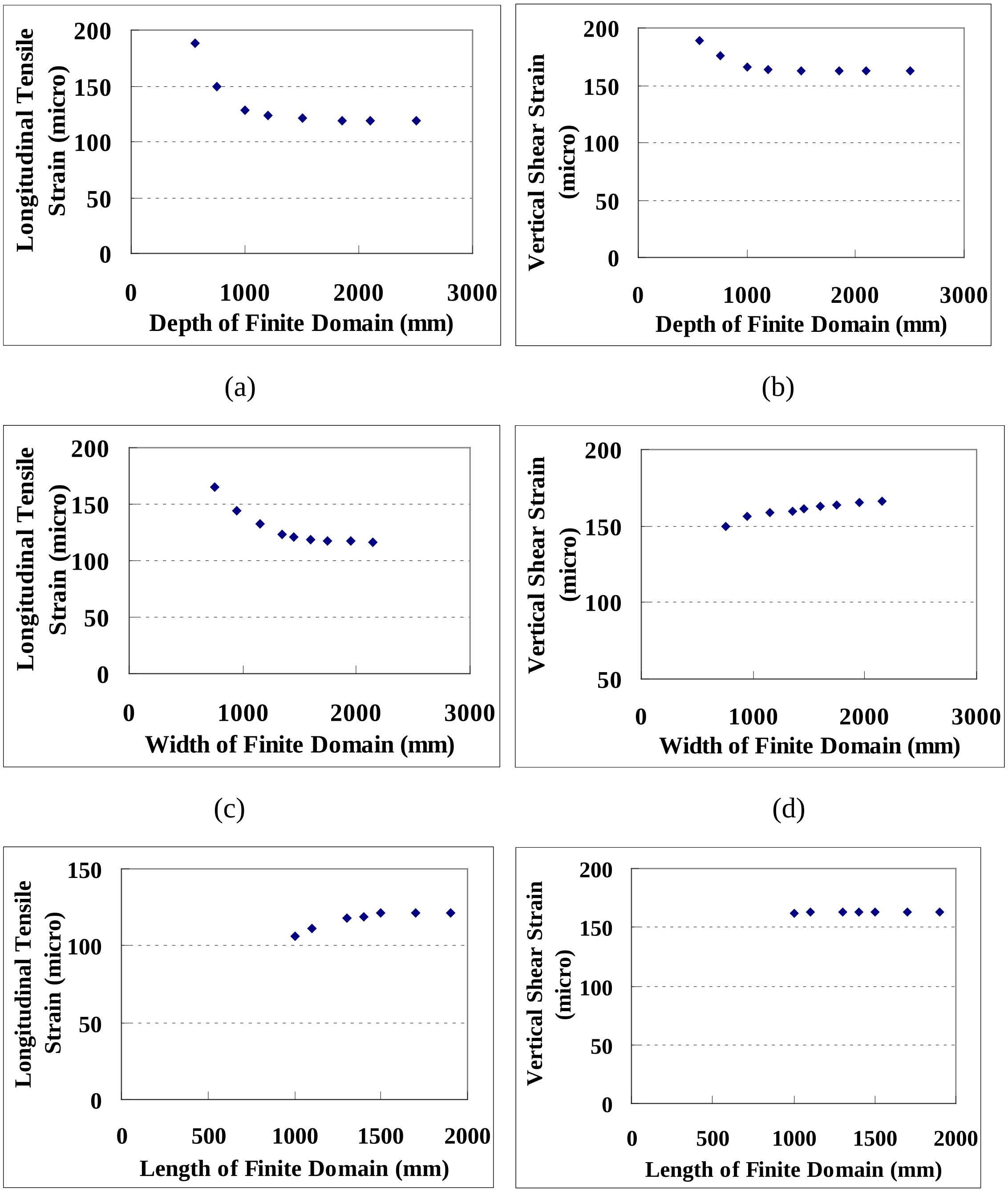

(a) (b)

(c) (d)

(e) (f)

Figure 4.2 Sensitivity analysis of finite domain size for (a) tensile strain vs. domain depth; (b) shear strain vs. domain depth; (c) tensile strain vs. domain width, (d) shear strain vs. domain width; (e) tensile strain vs. domain length; and (f) shear strain vs. domain length

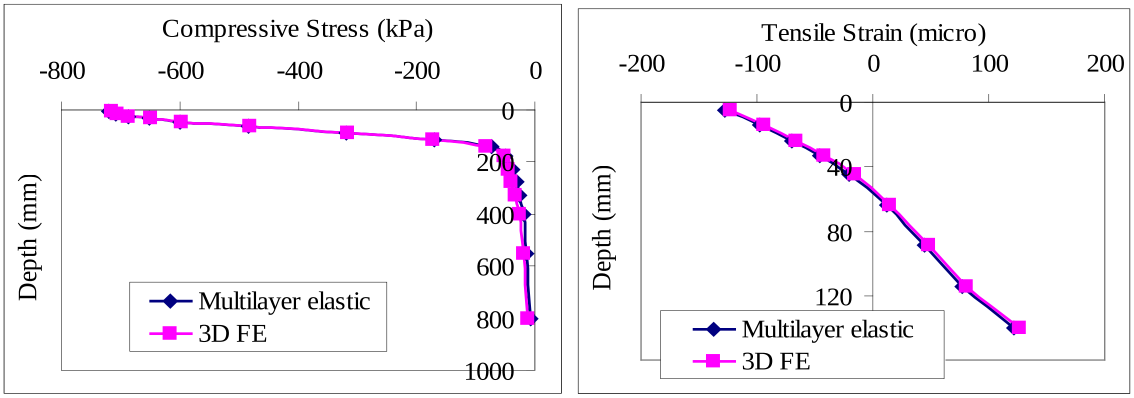

(a) (b)

Figure 4.3 Comparisons between FE and multilayer elastic solutions for (a) compressive stresses; and (b) longitudinal tensile strains

4.2 Material and Interface Characterization

4.2.1 Viscoelastic Asphalt Concrete Layer

Mechanistic analysis of pavement responses requires constitutive modeling of each pavement layer. While elastic theory may be a reasonable approximation for asphalt concrete in the conventional design of flexible pavements, the effect of time (or frequency) and temperature dependency of asphalt concrete modulus cannot be fully considered using this approach. The time-dependent nature of asphalt concrete modulus is characterized by the fact that the stress depends not only on the current state of strain but also on the full history of strain development. An integration model decomposed for the deviatoric and bulk stresses is usually used in the 3-D viscoelastic theory (Equations 4-3 and 4-4) (Ferry 1980). In these equations, the relaxation modulus can be modeled as a generalized Maxwell solid model (Figure 4.4) in terms of a Prony series, Equations 4-5 and 4-6 (ABAQUS 2007).

$$s = \int_{-\infty}^{t} 2G(t-\tau)\frac{de}{d\tau}d\tau \tag{4-3}$$

$$p = \int_{-\infty}^{t} K(t-\tau)\frac{d(tr[\varepsilon])}{d\tau}d\tau \tag{4-4}$$

$$G(t) = G_0(1-\sum_{i=1}^{n} G_i(1-e^{-t/\tau_i})) \tag{4-5}$$

$$K(t) = K_0(1 - \sum_{i=1}^{n} K_i(1 - e^{-t/\tau_i})) \quad (4\text{-}6)$$

where s is deviatoric stress; e is deviatoric strain; p is volumetric stress; $tr[\varepsilon]$ is trace of volumetric strain; G is shear modulus; K is bulk modulus; t is relaxation time; G_0 and K_0 are instantaneous shear and volumetric elastic moduli; and G_i, K_i; and τ_i are Prony series parameters.

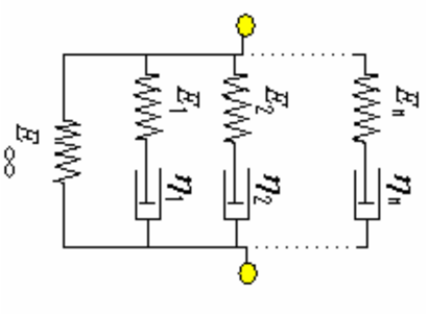

Figure 4.4 Illustration of a generalized Maxwell solid model

The temperature dependency of asphalt concrete modulus is characterized by time-temperature superposition principle because the asphalt concrete has been proved as a thermorheologically simple (TRS) material. Therefore, the effect of temperature on the asphalt concrete modulus can be considered using the reduced time (or frequency). This behavior allows for the horizontal shifting (along time or frequency axis) of the material property to form a single characteristic master curve as a function of reduced time (or frequency) at a desired reference temperature (Equations 4-7 and 4-8). The amount of horizontal shift is decided by the time-temperature shift factor. The relationship between the shift factor and the temperature can be approximated by the Williams-Landell-Ferry (WLF) function (Equation 4-9) (ABAQUS 2007). When combined with the master curve, the time-temperature shift factor allows for the prediction of the viscoelastic behavior over a wide range of conditions.

$$E(t, T) = E(\xi) \quad (4\text{-}7)$$

$$\xi = t / a_T \quad (4\text{-}8)$$

where t is time before shifting for a given temperature, T; ξ is reduced time at reference temperature; and a_T is shift factor for temperature T.

$$\log(a_T) = -\frac{C_1(T - T_0)}{C_2 + (T - T_0)} \qquad (4\text{-}9)$$

where T_0 is reference temperature; T is actual temperature corresponding to the shift factor; and C_1, C_2 are regression parameters.

The viscoelastic property of asphalt concrete can be predicted using the time-dependent creep compliance test, or the frequency-dependent complex modulus test. Different laboratory setups are available for conducting these tests: uniaxial, triaxial, or indirect tensile (IDT). The indirect tensile setup was used in this study to allow testing thin asphalt layer cores taken from the field. The test specimens were cut from the field cores and have the dimensions of 152mm in diameter by 51mm in height.

The IDT creep tests were performed at five temperatures (-15, -5, 5, 15, and 25°C) for 100s under a constant load (Figure 4.5). Stress/strain levels applied to the specimens were kept low enough to ensure minimum damage during the entire testing period, and therefore, linear viscoelastic behavior. The creep compliance [D(t)] was calculated based on the measured deformations using the AASHTO T322 method (Buttlar and Roque 1994). Master creep curves were constructed by horizontally shifting the creep curves at various temperatures to the creep curve at the reference temperature of 25°C.

The relaxation modulus E(t) is the ratio of stress response to a constant strain input, while the creep compliance, D(t), is the ratio of the strain response to a constant stress input. For a purely elastic material, E(t) and D(t) are reciprocals. However, for the viscoelastic material, this is only true in the Laplace transform domain. Ferry (1980) showed that there is an exact relationship between the creep compliance and relaxation modulus using the convolution integral in Equation 4-10.

$$\int_0^t E(t-\tau)D(\tau)d\tau = t \quad \text{for } t>0 \qquad (4\text{-}10)$$

An approximate method can be used to convert from creep compliance to relaxation modulus if both the creep compliance and relaxation modulus are modeled using a power law analytical form, as shown in Equation 4-11. Practically, the laboratory-determined creep compliance is not exactly represented by power law function. In this case, the local slope of the power model can be determined using Equation 4-12 (Park and Kim 1999). The bulk (K) and shear (G) relaxation modulus are calculated from relaxation modulus (E) assuming a constant Poisson's ratio and fitted into the Prony series as a generalized

Maxwell solid model (Equations 4-11 and 4-12). This inter-conversion method has been successfully used by the previous researchers when analyzing the viscoelastic behavior of pavement structure (Elseifi et al. 2006; Yoo and Al-Qadi 2008). The fitted Prony series parameters for the asphalt layer in two flexible pavement sections are shown in Tables 4.1 and 4.2, respectively.

$$E(t)D(t) = \frac{\sin n\pi}{n\pi} \tag{4-11}$$

$$n = \left| \frac{d \log D(t)}{d \log t} \right| \tag{4-12}$$

where $E(t) = E_1 t^{-n}$ is relaxation modulus; and $D(t) = D_1 t^{n}$ is creep compliance.

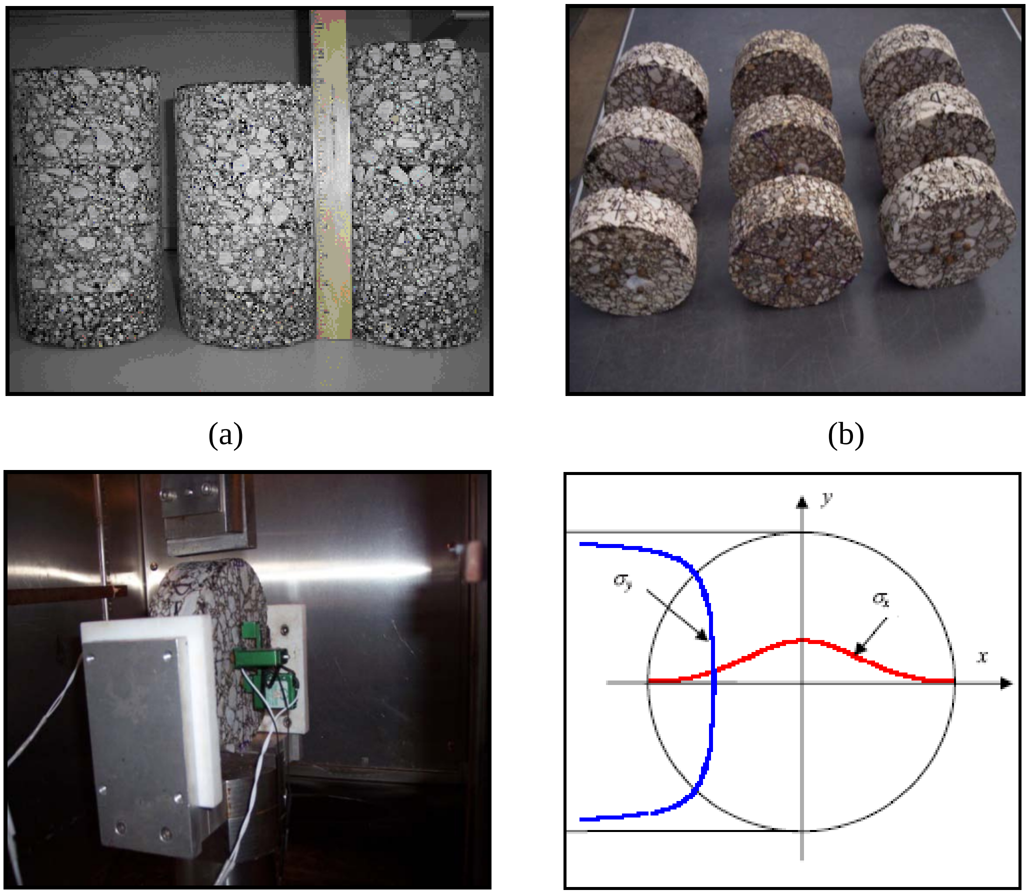

(a) (b)

(c) (d)

Figure 4.5 Indirect tensile test: (a) cores taken from field; (b) prepared specimens for test; (c) IDT set-up for testing; and (d) schematic stress state in the IDT test

Table 4.1 Viscoelastic Parameters of Asphalt Concrete in Full-Depth Pavement at 25°C

i		Wearing surface		Binder course		Base course	
		G_i or K_i	τ_i	G_i or K_i	τ_i	G_i or K_i	τ_i
1		3.66E-01	1.13E-04	3.88E-01	1.13E-04	4.52E-01	1.13E-04
2		2.70E-01	3.14E-03	3.15E-01	3.14E-03	2.78E-01	3.14E-03
3		1.34E-01	1.30E-02	8.21E-02	1.30E-02	1.48E-01	1.30E-02
4		1.61E-01	1.64E-01	1.73E-01	1.64E-01	1.08E-01	1.84E-01
5		4.75E-02	2.09E+00	2.51E-02	2.09E+00	7.46E-03	2.29E+00
6		1.95E-02	3.77E+01	1.07E-02	3.77E+01	4.36E-03	2.57E+01
WLF	C_1	18.06		20.24		20.70	
	C_2	197.82		184.67		173.61	

Table 4.2 Viscoelastic Parameters of Asphalt Concrete in Thin Asphalt Pavement at 25°C

i	Surface course		WLF	
	G_i or K_i	τ_i		
1	6.31E-01	2.06E-02	C_1	18.1
2	2.51E-01	1.73E-01		
3	8.47E-02	1.29E+00		
4	2.67E-02	5.35E+00	C_2	164.7
5	6.66E-03	1.06E+02		

4.2.2 Nonlinear Anisotropic Aggregate Base Layer

The resilient modulus of unbound material is defined as the ratio of the deviatoric stress to the recoverable part of the axial strain from the triaxial load tests, as shown in Equation 4-13 (Huang 1993). Many nonlinear models have been proposed over the years to incorporate the effect of stress level on the resilient modulus. The most commonly used nonlinear elastic model is the k-θ model or the two-parameter bulk stress model (Hicks and Monismith 1971). Uzan (1992) introduced the effect of octahedral shear stress to the k-θ model and added atmospheric pressure as a normalizing factor. The octahedral shear-stress term is believed to account for the dilation effect that takes place when a pavement element is subjected to a large principal stress ratio directly under a wheel load.

$$M_r = \frac{\sigma_d}{\varepsilon_r} \tag{4-13}$$

where σ_d is deviatoric stress; and ε_r is recoverable strain.

An isotropic model has the same resilient modulus in all directions, while a cross-anisotropic model has different material properties (i.e., resilient modulus and Poisson's ratio) in the horizontal and vertical directions. Previous research studies have proved that granular base layers in the pavement exhibit cross-anisotropic behavior due to compaction and the wheel loading applied in the vertical direction (Tutumluer 2008). Assuming the 1-2 plane (horizontal plane) to be the plane of isotropy, the constitutive stress-strain relation for cross anisotropy can be expressed as in Equation 4-14 (Zienkiewicz 2000). Therefore, five material parameters ($E_1, E_3, G_{13}, \nu_{12}$, and ν_{31}) are needed to define a cross-anisotropic elastic material.

$$\begin{Bmatrix} \sigma_{11} \\ \sigma_{22} \\ \sigma_{33} \\ \sigma_{12} \\ \sigma_{13} \\ \sigma_{23} \end{Bmatrix} = \begin{bmatrix} D_{1111} & D_{1122} & D_{1133} & 0 & 0 & 0 \\ & D_{2222} & D_{2233} & 0 & 0 & 0 \\ & & D_{3333} & 0 & 0 & 0 \\ & & & D_{1212} & 0 & 0 \\ & sym & & & D_{1313} & 0 \\ & & & & & D_{2323} \end{bmatrix} \begin{Bmatrix} \varepsilon_{11} \\ \varepsilon_{22} \\ \varepsilon_{33} \\ \varepsilon_{12} \\ \varepsilon_{13} \\ \varepsilon_{23} \end{Bmatrix} \tag{4-14}$$

$$\text{with} \quad \begin{aligned} D_{1111} &= D_{2222} = E_1(1-\nu_{13}\nu_{31})\lambda \\ D_{3333} &= E_3(1-\nu_{12}\nu_{12})\lambda \\ D_{1122} &= E_1(\nu_{12}+\nu_{31}\nu_{13})\lambda \\ D_{1133} &= D_{2233} = E_1(\nu_{31}+\nu_{12}\nu_{31})\lambda \\ D_{1212} &= G_{12} = E_1/(2(1+\nu_{12})) \\ D_{1313} &= D_{2323} = G_{13} \\ \lambda &= 1/(1-\nu_{12}^2-2\nu_{13}\nu_{31}-2\nu_{12}\nu_{13}\nu_{31}) \end{aligned}$$

where E_1 is modulus in the plane of isotropy; E_3 is modulus normal to the plane of isotropy; ν_{12} is Poisson's ratio for strain in direction 2 due to stress in direction 1; ν_{13} is Poisson's ratio for strain in direction 3 due to stress in direction 1; ν_{31} is Poisson's ratio for strain in direction 1 due to stress in direction 3; G_{13} is shear modulus in 1-3 plane; and $E_1 / E_3 = \nu_{13} / \nu_{31}$.

In this study, the granular base layer is modeled as a cross anisotropic material and the vertical, horizontal, and shear moduli are described using the generalized model adopted in the proposed AASHTO MEPDG, Equations 4-15, 4-16, and 4-17, respectively (ARA 2004). In this model, the first stress invariant or bulk stress term considers the hardening effect, while the octahedral shear stress term considers the softening effect. The stress dependency of Poisson's ratios is not considered in this study and the in-plane and out-of-plane Poisson's ratios are assumed constant.

$$M_r^v = k_1 p_a (\frac{\theta}{p_a})^{k_2} (\frac{\tau_{oct}}{p_a} + 1)^{k_3} \tag{4-15}$$

$$M_r^h = k_4 p_a (\frac{\theta}{p_a})^{k_5} (\frac{\tau_{oct}}{p_a} + 1)^{k_6} \tag{4-16}$$

$$G_r = k_7 p_a (\frac{\theta}{p_a})^{k_8} (\frac{\tau_{oct}}{p_a} + 1)^{k_9} \tag{4-17}$$

where M_r^v is vertical resilient modulus (kPa); M_r^h is horizontal resilient modulus (kPa); G_r is shear resilient modulus (kPa); θ is bulk stress (kPa); τ_{oct} is octahedral shear stress (kPa); $k_1, k_2, k_3, k_4, k_5,\ k_6, k_7, k_8, k_9$ are exponent parameters; and p_a is atmospheric pressure (100kPa).

Table 4.3 summarizes the nonlinear model parameters used in the FE analysis for the granular base layer. The model parameters were obtained from a previous project for evaluating the effectiveness of geogrid reinforcement (Al-Qadi et al. 2007; Kwon et al. 2009). Repeated load triaxial tests were conducted on the aggregate material to determine its resilient modulus properties following the AASHTO T307 procedure. The anisotropic modulus properties were determined by applying vertical and radial dynamic stress states on the same specimen (Tutumluer and Seyhan 1999).

Table 4.3 Nonlinear Anisotropic Model Parameters for Granular Base Layer

Modulus	$k_1/k_4/k_7$	$k_2/k_5/k_8$	$k_3/k_6/k_9$	ν_{12}	ν_{31}
Vertical	1010	0.791	-0.477	0.35	0.35
Horizontal	277	1.071	-1.332		
Shear	321	0.857	-0.681		

4.2.3 Subgrade Modulus

Typically, the modulus of fine-grained soil decrease as stress levels increase and thus show the stress-softening behavior. The softening behavior of the subgrade is important when the stress level in the subgrade is relatively high, such as in thin asphalt pavements. A nonlinear stress-dependent model is used for subgrade stiffness (Equation 4-18), that is similar to the one used for the granular base layer with k_2=0. The coefficients (k_1=0.8125 and k_3 =-11.5) were estimated from the bilinear model parameters (Thompson and Robnett 1979), which was used by Kwon et al. (2009) in the previous research.

$$M_R = k_1 p_a (\frac{\tau_{oct}}{p_a} + 1)^{k_3} \tag{4-18}$$

In order to compare the model results using both linear and nonlinear subgrade models, the linear elastic modulus of the subgrade in the thin asphalt pavement section was estimated from its California Bearing Ratio (CBR) value using the equation in the AASHTO MEPDG, Equation 4-19 (ARA 2004).

$$M_R = 2555(CBR)^{0.64} \tag{4-19}$$

where M_R is resilient modulus of subgrade in psi; and CBR is California Bearing Ratio of subgrade in percentage.

The subgrade in the full-depth pavement section is modeled having linear elastic modulus considering the stress transmitted into the subgrade under a thick asphalt layer is relatively small. The falling weight deflectometer (FWD) test results were used to back-calculate the linear elastic modulus of the subgrade. The back-calculated subgrade modulus is 393MPa for the lime-stabilized layer and 173MPa for the deeper natural soil.

4.2.4 Interface Model

Contact conditions at layer interfaces are important parameters that could significantly affect pavement responses to vehicular loading. It is expected that the layers within the pavement structure remains in contact with no gap-opening since the contact area is very large and high compressive loading is applied by vehicles. This assumption was controlled by the “no separation” feature supported by ABAQUS. In addition, it is assumed that both relative and absolute motions of contacting surfaces at layer interfaces are small.

The interface bonding between asphalt layers is significantly affected by the type and quantity of tack coat and construction quality. In this study, the HMA layers were assumed to be fully-bonded (tied) in the thick asphalt pavement, which is validated by field core inspection from test sections. The Coulomb friction model with a friction coefficient of 1.0 was used at the HMA-base interface (Romanoschi and Metcalf 2001). The coefficient of friction (μ) is defined as the ratio of the allowed maximum shear stress before the interface slides and the normal stress, as shown in Equation 4-20.

$$\mu = \tau_{\max} / \sigma \tag{4-20}$$

where $\tau_{\max}$ is allowed maximum shear stress before sliding; and σ is normal stress at the interface.

4.3 Nonlinear Solution Technique

Several solution techniques have been used to solve the nonlinearity problem of the granular material. Tutumluer (1995) recommended that a direct secant stiffness method (also known as a fixed point iteration method) with a damped factor should be used due to the hardening nature of the granular material. The direct secant stiffness method solves the nonlinear load displacement behavior by updating the secant stiffness at each iteration until that a convergence is reached for the load increment. Kim and Tutumluer (2008) further developed a user material subroutine (UMAT) in ABAQUS by utilizing the direct secant stiffness approach. Hjelmstad and Taciroglu (2000) analyzed the nonlinear flexible pavement responses using a Newton-Raphson approach with tangent stiffness. In their approach, the nonlinear stress-dependent model of the granular base layer was formulated as a function of strain states not stresses. Schwartz (2002) employed the hypoelastic material model in ABAQUS to simulate the nonlinear behavior of the granular material. The nonlinear stress-dependent modulus of the granular material was numerically converted to tangent modulus for input as a function of the first stress invariant.

ABAQUS/Standard uses the iterative Newton-Raphson method to solve nonlinear equations. The applied load is augmented incrementally, and at each increment the program solves a system of equations through iterations. The iterations continue on the basis of the previous solutions until it reaches a reasonable convergence (ABAQUS

2007). Because the modulus of the granular material is a function of the total stress state, a modified Newton-Raphson approach with secant stiffness is used in this study.

Figure 4.6 shows the iteration process of the modified Newton-Raphson approach with secant stiffness. The load (P) is applied in small increments and the displacement for each load increment (u) is determined using the current stiffness matrix (K) of the model. The residual force (R) between the applied load increment and the load increment determined from the internal stress state is calculated. If the residual force is within the specified tolerance, the increment is deemed to have converged and the next load increment is applied. If the residual force is not within the tolerance, then the stiffness matrix is recalculated and an additional displacement is determined. This iterative process continues until the difference between the applied and calculated load increment is within the tolerance value.

In the FE model, a UMAT is developed to calculate the anisotropic modulus of the granular material corresponding to the stress state at each iteration. The UMAT allows users to implement general constitutive models other than the default models in ABAQUS. The flowchart of the UMAT is shown in Figure 4.7. Within the UMAT, the Jacobian Matrix (incremental stiffness matrix) is calculated and the total stress state is updated using the forward Euler (explicit integration) approach. The Jacobian Matrix (C) is defined using Equation 4-21 (ABAQUS 2007).

$$C = \frac{\partial \Delta \sigma}{\partial \Delta \varepsilon} \tag{4-21}$$

where C is Jacobian Matrix (incremental stiffness matrix); $\partial \Delta \sigma$ is increment in stress; and $\partial \Delta \varepsilon$ is increment in strain.

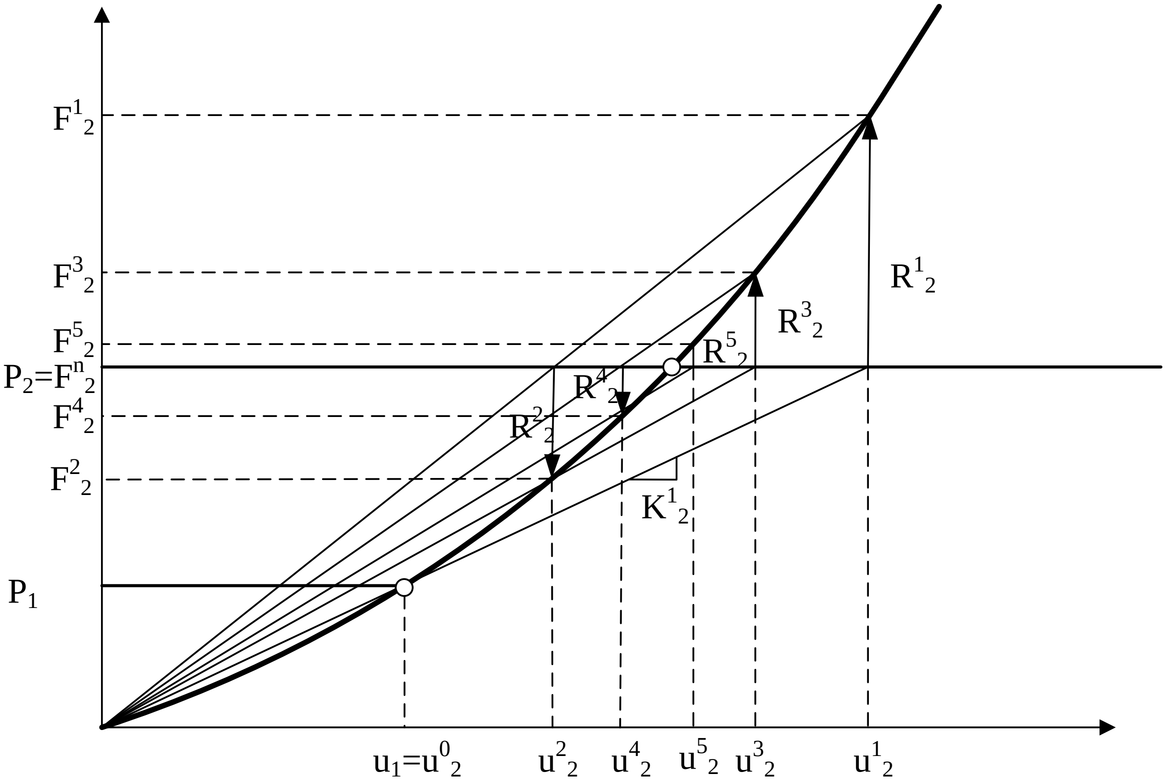

P_1: load increment 1;
u_1: total displacement at load increment 1 after equilibrium;
P_2: load increment 2;
u^1_2: total displacement after 1st iteration at load increment 2;
F^1_2: calculated internal load after 1st iteration at load increment 2;
R^1_2: residual force after 1st iteration at load increment 2;
K^1_2: secant stiffness for 1st iteration at load increment 2;
n: number of iterations for convergence.

Figure 4.6 A modified Newton-Raphson approach with secant stiffness

The UMAT program requires nine exponent parameters (k_1-k_9) and two Poisson's ratios (v_{12} and v_{13}) for calculating the nonlinear anisotropic modulus. In addition, the initial vertical stress is calculated as the overburden stress that results from the density (ρ) and thickness of the material above the point of interest. The initial horizontal stress depends on the material properties, over-consolidation history, and the residual stress caused by compaction. A coefficient of horizontal stress (k_0=1.0) is defined as the ratio of horizontal stress to overburden stress. To prevent unreasonable values, cutoff values are used for the minimum resilient modulus at low stress levels.

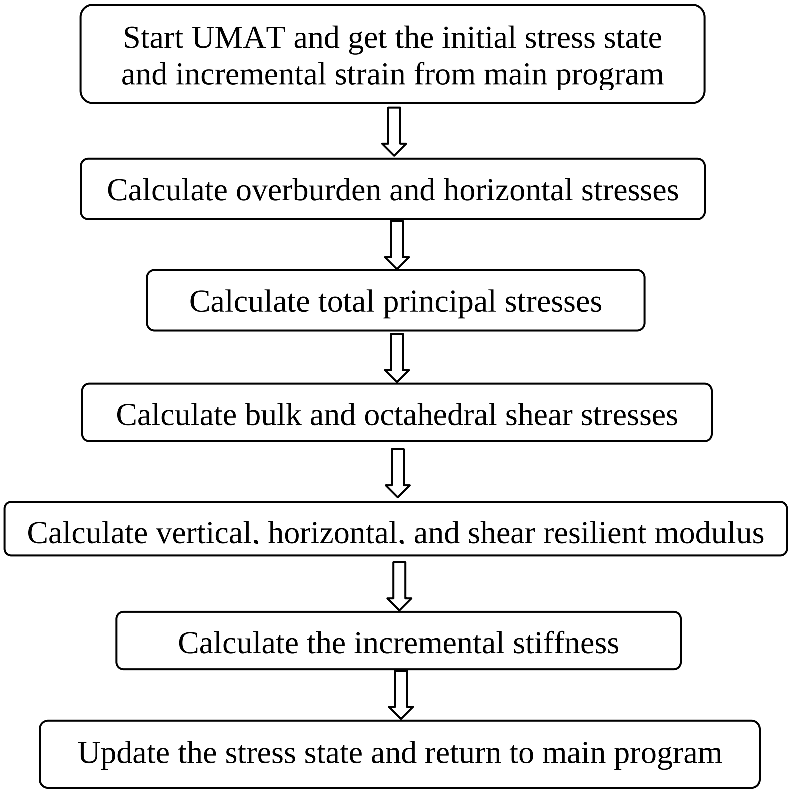

Figure 4.7 Flow chart of UMAT program

4.4 Tire Loading Simulation

4.4.1 Transient Moving Load

Traffic loading on a highway is a phenomenon that involves the repeated application of moving dynamic wheel loads. The dynamic wheel load is the sum of the static load and a continuously changing dynamic tire force. The dynamic tire force typically occurs in two distinct frequency ranges: 1.5-4 Hz for sprung mass (vehicle body) bounce, pitch and roll, and 8–15 Hz for unsprung mass (tire) bounce and roll. The dynamic load effect is typically expressed as the Dynamic Load Coefficient (DLC) equal to the coefficient of variation of the applied load. Typical DLC values range between 0.01 and 0.40, depending on the vehicle components (suspension and tire stiffness), operating conditions, and pavement roughness (OECD, 1992).

To define the dynamic wheel load, intensive field measurements from vehicle axles are needed. For pavement specialists, most studies are focused on measuring dynamic tire-pavement contact stresses rather than the stochastic distribution of dynamic wheel loads. In order to characterize the transient local dynamic load without extensive field data in this study, the dynamic loading is simplified by using the measured and predicted tire contact stresses on a smooth pavement surface.

There are several methods that can be used to simulate vehicular loading: stationary constant load; moving constant load; stationary transient load (triangle, trapezoidal, or haversine function); and moving transient load. The load applied by the vehicle is in nature a continuously changing moving load as the vehicle is approaching and leaving. To simulate the nature of moving vehicular loading at a certain speed, the concept of continuously moving load (Yoo and Al-Qadi 2008) is used in this study.

In this approach, the loading area is gradually shifted over the pavement surface at each step until a single wheel pass is completed, as shown in Figure 4.8. At each loading step, a linear loading amplitude was applied to accurately simulate the variation of contact stresses in the tire imprint area. Different loading amplitude paths were used to define the entrance and the exit parts of the tire imprint, respectively.

For example, the tire imprint of rib A is composed of nine elements (A1-A8) and A9 is the element that the tire is approaching. As the vehicle approaches a given element in the loading path, the element is loaded with the amplitude that simulates the increase in loading with time (A6-A9). Similarly, as the tire moves away from a given element, the loading amplitude that simulates the decrease in loading with time is used (A1-A4). For each loading step, the tire imprint area is maintained constant. The step time is decided by the vehicle speed and element lengths. The time increment in each step is selected to satisfy the time integration requirement for implicit dynamic analysis and the convergence requirement for the nonlinear iteration.

4.4.2 Incorporation of Tire-Pavement Contact Stresses

In the FE model, the 3-D tire-pavement contact stresses (vertical, transverse, and longitudinal) under each rib were applied on the tire imprint area, respectively (Figure 4.9). The exact footprint shape at a specific load and tire pressure level is considered by adjusting the number and dimension of elements within the tire imprint area of each rib. Generally, the tire imprint area of each rib includes two elements laterally and seven to ten elements longitudinally. All elements along a tire rib were loaded with non-uniform vertical contact stresses corresponding to their locations within the tire imprint area. As the tire is moving, the loading amplitudes of vertical contact stress change continuously at each step. The transverse and longitudinal contact stresses are assembled into the equivalent concentrated forces using element shape functions, and assumed constant at each loading step.

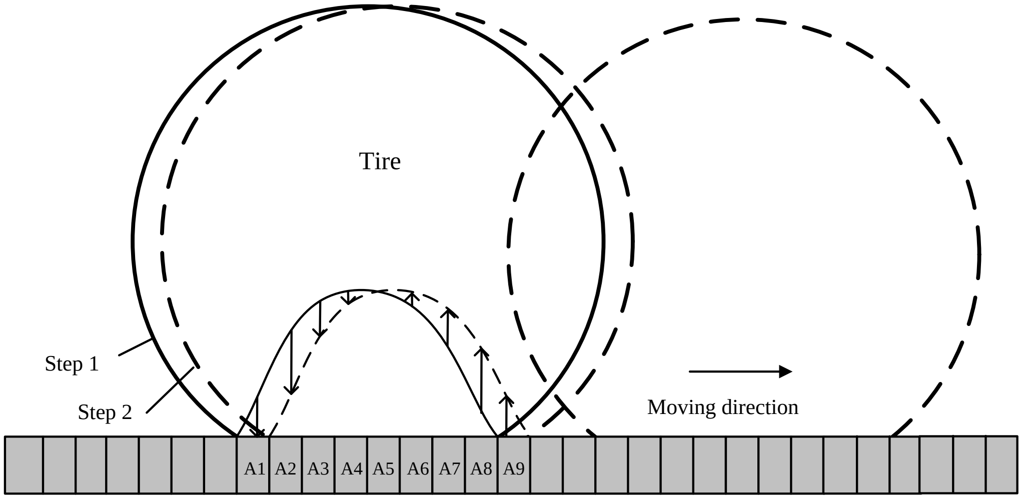

Figure 4.8 Schematic illustration of tire moving along pavement surface

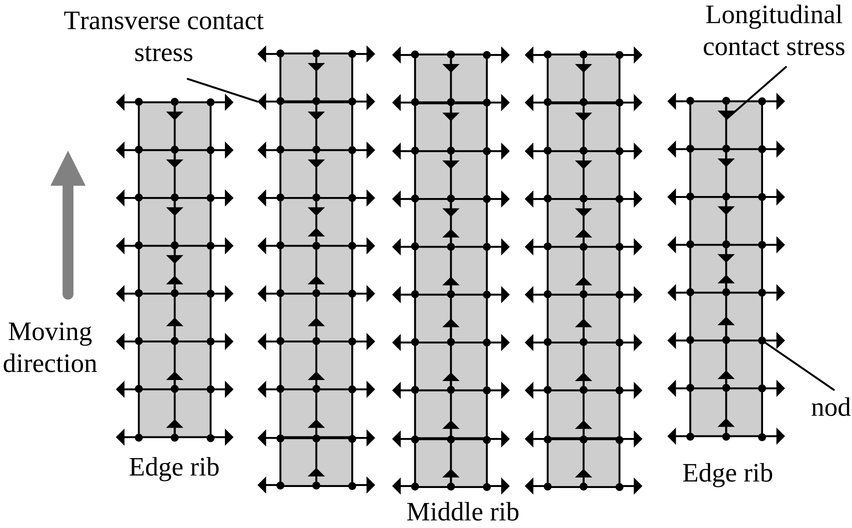

Figure 4.9 Incorporation of 3D contact stresses under each tire rib

4.5 Implicit Dynamic Analysis

Three different approaches can be used in pavement analysis: static, quasi-static, and dynamic transient analysis. The static approach has been traditionally used in multilayer elastic analysis. The quasi-static approach is based on the concept of moving the load at subsequent positions along the pavement for each time step, and assuming the load is static at each position. Inertia or damping effects are not considered in quasi-static analysis. In dynamic transient analysis, two important factors need to be considered, the inertia associated with the moving load and the dependency of the material properties on the loading frequency.

Dynamic problems can be considered to be either structural dynamics or wave propagation problems. In general, a wave propagation problem deals with very high frequency mode shapes in a very short period (e.g., explosion, vehicle crash, and buckling). In wave propagation problems, the analysis spans a short period of time and it is typically of the order of a wave travel time across the structure. Hence, the structure responses are rich in high frequencies and the number of the significant modes should be large. However, a structural dynamic problem considers a more slowly changing load, which is dictated by lower mode shapes. In these problems, the focus may be on how the structure responses under prescribed loads, i.e., a time history analysis. The structure excitation is usually of the same order of the structure's lowest natural frequencies. In other words, the response is dominated by the lower modes, and high modes may be insignificant in application (Chopra 2001, Bathe 1996).

Basically, if the rise time and duration of the load exceeds a small multiple of the time required for a stress wave to travel through the structure, the problem is probably a structural dynamic problem. In pavement analysis, the vehicle speed, e.g., 8km/h (2.2m/sec) in this study is much smaller than the stress wave speed (100-600m/sec) in the flexible pavement structure (OECD 1992). Hence, the pavement analysis problem may be classified as a structural dynamic problem.

The equation of motion of a multiple degree of freedom system with viscous damping is shown in Equation 4-22. Dynamic analysis of linear problems is generally solved by using the eigenmodes of the system as a basis for calculating the response. For a nonlinear dynamic analysis problem, the direct integration method is commonly used. In this method, the equation of motion is integrated using a numerical step-by-step procedure at discrete time intervals. Two types of direct integration are available, explicit and implicit. The implicit integration method computes the displacements at time *t* and *t-1* by solving a set of nonlinear equations simultaneously, while the explicit integration computes the displacement at time *t* by adding the incremental displacement between time *t* and *t-1* computed by double integration of the acceleration. The implicit dynamic analysis is used in this study, because it provides better numerical stability than explicit analysis and is generally efficient for structural dynamic problems (Bathe 1996).

$$[M]\{\ddot{U}\}+[C]\{\dot{U}\}+[K]\{U\}=\{P\} \tag{4-22}$$

where $[M]$ is mass matrix; $[C]$ is damping matrix; $[K]$ is stiffness matrix; $\{P\}$ is external force vector; $\{\ddot{U}\}$ is acceleration vector; $\{\dot{U}\}$ is velocity vector; and $\{U\}$ is displacement vector.

The implicit integration method in ABAQUS uses the Newmark integration scheme and the Hilber–Hughes–Taylor method (*α -method)* (ABAQUS 2007). The *α -method* is unconditionally stable if the analysis parameters are chosen properly. Therefore, the selection of time increment (Δt) is only dependent on the accuracy criterion. Because only low modes and a few intermediate modes are excited by the vehicular loading in the pavement structure, the dynamic response contribution in the high frequencies are negligible in the analysis. The procedure for choosing the time increment in implicit dynamic analysis is as follows (Bathe 1996): 1) identifying the dominant frequency (f) in the loading or responses of a structure; 2) selecting the time increment (Δt) less than or equal to $\frac{1}{20f}$. For example, as the vehicle speed is 8kmh, the time increment should be less than 0.005sec because the highest loading frequency is usually less than 10Hz.

The dynamic analysis considers the mass inertia effect and damping effect. As shown in Equation 4-22, the inertial force is equal to the mass multiplied by the acceleration, whereby the acceleration is the second derivative of the displacement. The dissipative contribution depends on the damping properties. The sources of damping can be an arbitrary damping factor, a friction factor, or a viscoelastic material behavior. When using viscoelastic material behavior for an asphalt layer, it is not necessary to introduce additional structural or mass damping for that layer. However, the elastic aggregate base layer and subgrade do not have such energy dissipation sources. Therefore, introducing a general damping rule to those layers is needed.

A popular spectral damping scheme used in structure dynamic analysis is Rayleigh damping; giving the damping matrix $[C]$ as the combination of mass-proportional damping and stiffness-proportional damping, as shown in Equation 4-23. For multiple degrees of freedom system, the critical damping ratio at any frequency of mode is given as Equation 4-24. The coefficients α_R and β_R can be determined from specific ξ_i and ξ_j for the i th and j th modes, respectively. If both modes are assumed to have the same damping ratio ξ, the Raleigh coefficients can be calculated using Equation 4-25 (Chopra 2001).

$$[C] = \alpha_R [M] + \beta_R [K] \tag{4-23}$$

$$\xi_i = \frac{\alpha_R}{2\omega_i} + \frac{\beta_R \omega_i}{2} \tag{4-24}$$

$$\alpha_R = \xi \frac{2w_i w_j}{w_i + w_j}, \ \beta_R = \xi \frac{2}{w_i + w_j} \tag{4-25}$$

where α_R, β_R are Raleigh coefficients; and ξ_i is critical damping ratio at the frequency of ω_i.

For the dynamic loading on a pavement structure, the two frequencies in calculating the Raleigh coefficients may be taken as the lowest natural frequency of the structure and the highest loading frequency. The critical damping ratio of soil falls in the range of 2% to 5% depending on the confining pressure and shear strain level, which can be measured from the resonant column test or cyclic triaxial test (Zhong et al. 2002). Because the granular base layer and subgrade are considered as elastic material without any other energy dissipation sources (such as plastic), the maximum damping ratio, 5%, is used.

4.6 Comparison between Model Results and Field Measurements

Two typical pavement structures were selected in this dissertation: a thin asphalt pavement with a granular base layer (simulating a secondary road), and a thick asphalt pavement, such as that used for interstate highway systems. The two pavement structures were exposed to the accelerated pavement testing (APT) using the Accelerated Testing Loading ASsembly (ATLAS) (Figure 4.10). The full-scale pavement testing provides an acceptable middle ground between real pavement loading in the field and laboratory tests. Various pavement responses were measured during APT using *in-situ* instrumentations, including strains, stresses, and deflections.

(a) (b)

Figure 4.10 Advanced Transportation Loading ASsembly (ATLAS) with a (a) dual-tire assembly; and (b) wide-base tire

The secondary road pavement structure resembled one of the existing test sections constructed in a previous project for evaluating the effectiveness of geogrid reinforcement (Al-Qadi et al. 2007). It is composed of a 76-mm asphalt layer and a 305-mm unbound aggregate base layer, as shown in Figure 4.11(a). PG 64-22 binder was used in the SM-9.5 mix (surface mix with maximum nominal aggregate size of 9.5mm) for the asphalt layer. Dense-graded crushed limestone aggregates were used for the granular base layer. The pavement section was constructed on subgrade with a low CBR of 4. During construction, strain gauges were embedded at the bottom of the asphalt layer, and pressure cells and linear variable deflection transformers (LVDTs) were embedded in the base layer and subgrade. Thermocouples were placed in the asphalt layer, base layer, and subgrade to monitor the pavement temperature.

The thick pavement structure is one of the test sections built as part of an extended-life pavement project (Carpenter 2008). It is composed of a 254-mm asphalt layer directly over a lime-stabilized subgrade, as shown in Figure 4.11(b). Two asphalt binders were used in the asphalt layers: a PG 64-22 for base course, and an SBS PG 70-22 for polymer-modified binder course and wearing surface. The asphalt contents of the binder and base courses are 4.5%; while the asphalt content of wearing surface is 5.4%. No liquid anti-strips were used in any mixture. The aggregate used in all mixes is limestone. The subgrade is lime-stabilized to address the high water content existing in the natural soil. Longitudinal strain measurements were obtained at the stabilized subgrade–asphalt layer interface using an H-shape strain gauge. Temperature data was continuously collected using T-type copper–constantan thermocouples throughout the pavement depth.

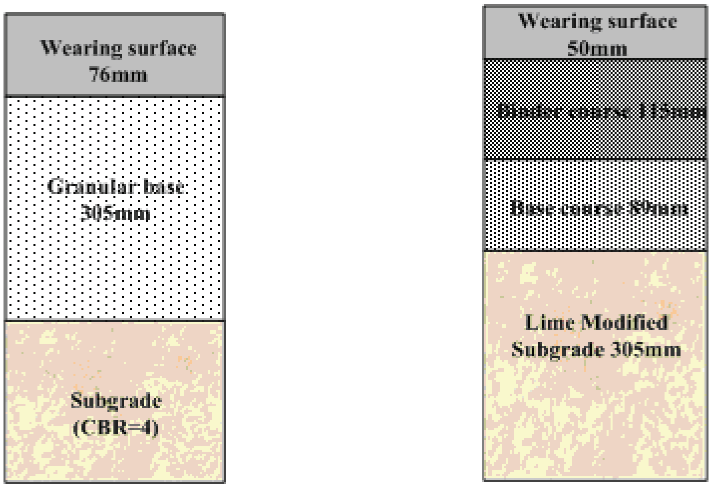

(a) (b)

Figure 4.11 Cross sections of (a) thin asphalt pavement and (b) thick asphalt pavement

The FE solutions are compared with the field measurements to further check the accuracy of the model. Table 4.4 compares the measured and calculated longitudinal tensile strains at the bottom of the asphalt layer in the full-depth pavement section under the loading of two different tire configurations (690kPa, 8km/h, and 25ºC). Generally, the predicted tensile strains were found slightly greater than the measured strains. A good agreement of the response ratios caused by the two tire configurations is achieved between the predicted and measured results.

Table 4.5 compares the calculated pavement responses with the field measurements under the loading of a dual-tire assembly in the thin asphalt pavement section (35.5kN, 690kPa, 8km/h, and 30ºC). The pavement responses are calculated using various scenarios of contact stress distributions and material models. The use of 3-D contact stress distribution and the nonlinear model for the base layer and subgrade results in smaller differences between the measured and calculated stresses and strains, compared to the values obtained when the tire contact stresses are assumed uniform or the conventional linear isotropic model is used. It was found that, for the tensile strain at the bottom of the asphalt layer, the calculated strain is smaller than the measured strain, but the calculated responses in the base layer and subgrade are greater than the measured ones.

Table 4.4 Measured and Calculated Longitudinal Tensile Strains for Thick Asphalt Pavement Section (strain units: micro)

Tire configurations	Field measurements			FEM		
	35.5kN	44.4kN	53.3kN	35.5kN	44.4kN	53.3kN
Dual-tire assembly	89	105	119	102	115	131
Wide-base 455 tire	117	134	146	128	150	168
Ratios	1.31	1.28	1.23	1.25	1.30	1.28

Table 4.5 Measured and Calculated Pavement Responses for Thin Asphalt Pavement Section

Pavement responses	FEM			Field
Tire contact stress	Uniform	3-D		
Base and subgrade model	Nonlinear	Linear	Nonlinear	
Tensile strain at the bottom of asphalt layer (micro)	370	324	397	529
Vertical stress at the bottom of base (kPa)	68	66	63	44
Compressive strain on top of subgrade (micro)	1987	1094	1789	1656

The accuracy of FE analysis is affected by the material models used in the analysis. The discrepancies between the measured and the calculated pavement responses could be related to two reasons: 1) the nonlinear viscoelasticity of asphalt concrete was not considered in the analysis and these factors have more significant effects on the thin asphalt pavement responses with weak supports; 2) the measured tensile strains in the thin asphalt layer could be overstated because at the bottom of the thin asphalt layer the bending is more significant than tension. Considering the variability of as-built pavement thickness, environmental conditions, laboratory-measured material stiffness, and instrumentation responses, the discrepancies between the measured and the calculated responses were considered acceptable in this study for the purpose of comparing pavement responses at various tire loading conditions.

4.7 Summary

A 3-D FE model of flexible pavement is developed to analyze pavement responses under vehicular loading. This model utilizes implicit dynamic analysis and simulates the vehicular loading as a continuous moving load with three-dimensional contact stresses at the tire-pavement interface. In the model, the asphalt layer is modeled as a linear viscoelastic material and its relaxation modulus is converted from the laboratory-determined creep compliance data. The granular base layer is modeled as a nonlinear anisotropic material and its vertical, horizontal, and shear modulus is dependent on both the bulk stress and shear stress. A UMAT is developed to implement the constitutive model of the granular base layer in the FE model. The FE model results were compared with field measurements and the discrepancies were considered acceptable for the purpose of comparing pavement responses at various tire loading conditions.

CHAPTER 5 ANALYSES OF THIN ASPHALT PAVEMENT RESPONSES

5.1 Nonlinear Anisotropic Behavior of Granular Base

5.1.1 Modulus Distribution in Base Layer

In this chapter, the thin asphalt pavement section with a 76-mm-thick asphalt layer and a 305-mm-thick granular base layer, described in Chapter 4, is used in the analysis. Since the base layer is modeled having stress- and direction-dependent behavior, the modulus of the base layer is affected by the stress transmitted into the base layer and the material constitutive model. Figures 5.1 and 5.2 plot the distributions of vertical modulus in the base layer under the loading of a dual-tire assembly at 25°C and 47°C (35.5kN, 724kPa, and 8km/h), respectively, using the nonlinear isotropic model and anisotropic model for the granular base layer. Due to the symmetry of dual tires, only the asphalt layer and the base layer under one tire of a dual-tire assembly was plotted.

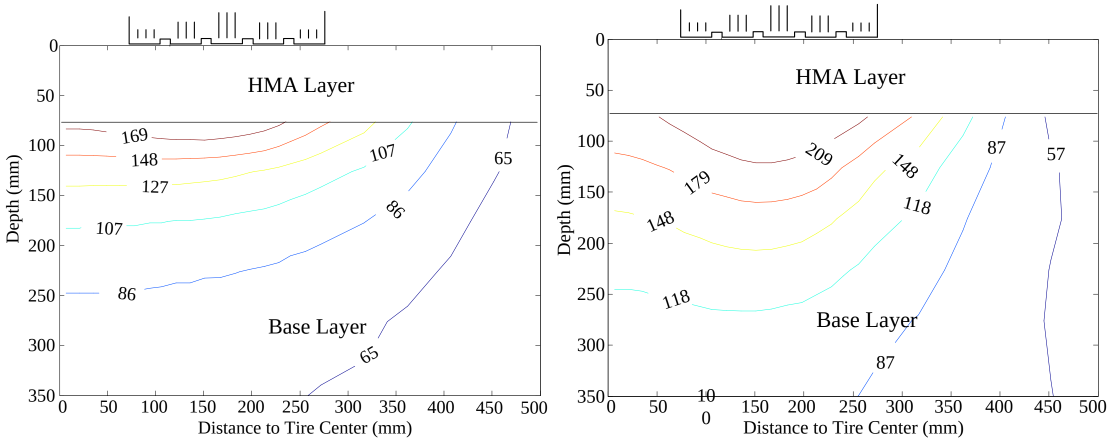

(a)

(b)

Figure 5.1 Vertical modulus distributions in base layer using nonlinear isotropic model at (a) 25°C and (b) 47°C

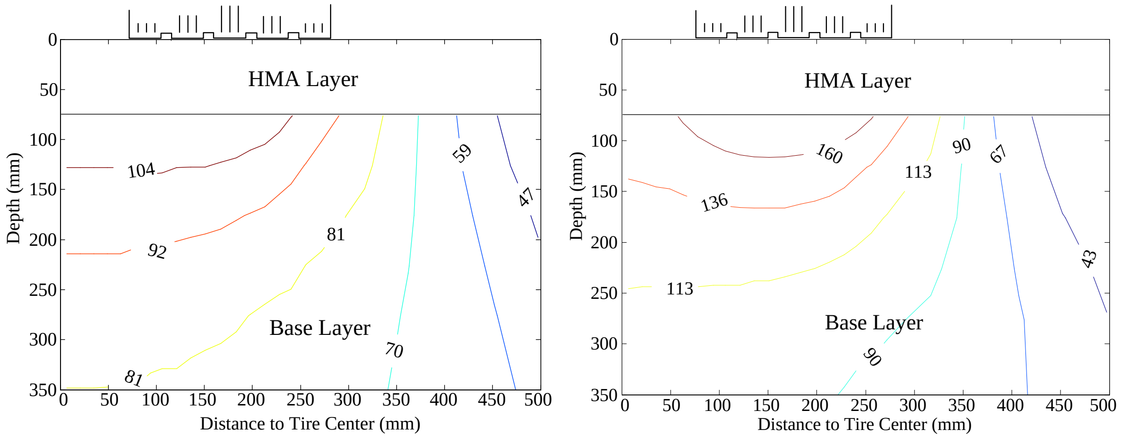

(a) (b)

Figure 5.2 Vertical modulus distributions in base layer using nonlinear anisotropic model at (a) 25°C and (b) 47°C

It is clearly shown that the modulus varies both vertically and horizontally because the stress state changes throughout the base layer. As expected, the highest modulus was observed on the top of the base layer under the loading center and the modulus decreases as the horizontal distance or vertical depth increases. It was found that the predicted vertical modulus using the anisotropic model is 10-40% less than the modulus predicted using the isotropic model, especially at the upper part of the base layer. This is because the granular material is modeled as a stress-hardening material and the anisotropic model results in less confinement stress at the upper part of the base layer.

Figures 5.3 and 5.4 plot the distributions of horizontal and shear modulus in the base layer under the loading of a dual-tire assembly at 25°C and 47°C, as the nonlinear anisotropic model is used for the base layer. The predicted horizontal modulus was found equal to 19 to 24% of the vertical modulus; the predicted shear modulus was found equal to 28 to 31% of the vertical modulus. Based on the model parameters for the anisotropic modulus, the horizontal modulus and shear modulus ratios (n and m) can be calculated using Equations 5-1 and 5-2. The modulus ratios increase as the bulk stress increases but decrease as the shear stress increases. Therefore, the modulus ratios are dependent on the combination of bulk stress and shears tress in the granular base layer.

The horizontal and shear modulus ratios were found having a relatively small range of variation and close to the constant ratio term (k_4 / k_1 or k_7 / k_1). This is consistent with the findings reported by Tutumluer and Thompson (1997). In their study, 49 triaxial test results of the aggregate from various sources were analyzed using the Uzan model and it was found that deviatoric and bulk stress terms have less effects in determining the modulus ratios when compared to the constant ratio term.

$$n = M_r^h / M_r^v = \frac{k_4}{k_1}\left(\frac{\theta}{p_a}\right)^{k_5-k_2}\left(\frac{\tau_{oct}}{p_a}+1\right)^{k_6-k_3} = 0.27\left(\frac{\theta}{p_a}\right)^{0.28}\left(\frac{\tau_{oct}}{p_a}+1\right)^{-0.86} \qquad (5\text{-}1)$$

$$m = G_r / M_r^v = \frac{k_7}{k_1}\left(\frac{\theta}{p_a}\right)^{k_8-k_2}\left(\frac{\tau_{oct}}{p_a}+1\right)^{k_9-k_3} = 0.32\left(\frac{\theta}{p_a}\right)^{0.07}\left(\frac{\tau_{oct}}{p_a}+1\right)^{-0.2} \qquad (5\text{-}2)$$

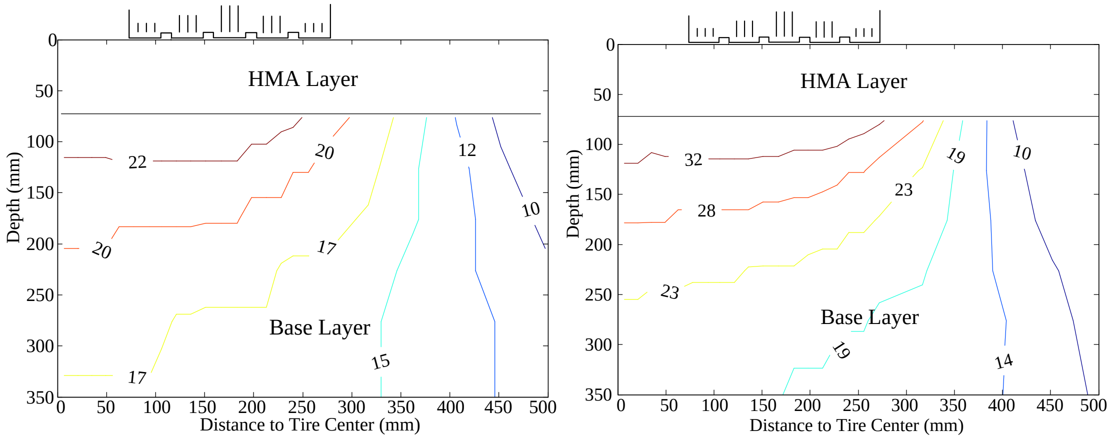

(a)

(b)

Figure 5.3 Horizontal modulus distributions in base layer using nonlinear anisotropic model at (a) 25°C and (b) 47°C

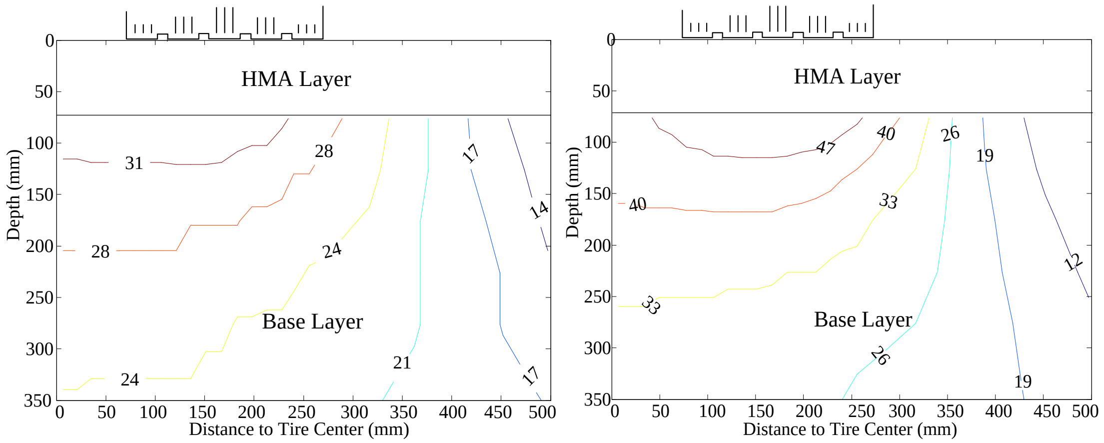

(a)

(b)

Figure 5.4 Shear modulus distributions in base layer using nonlinear anisotropic model at (a) 25°C and (b) 47°C

It is noted that the anisotropic moduli of the base layer (vertical, horizontal, and shear) increase as the temperature increases. This is because at high temperatures the asphalt layer becomes less stiff due to its viscoelastic nature and the base layer carries higher stress in the pavement structure. Similarly, the modulus of the base layer is affected by the vehicle speed. Figure 5.5 presents the distributions of vertical modulus in the base layer under the loading of a dual-tire assembly at 25°C and 47°C when the vehicle travels at a high speed (80km/h). Compared to Figure 5.2, the moduli of the base layer decrease by 10 to 33% as the vehicle speed increases by 10 times. This indicates that accurate pavement responses can only be predicted when the viscoelastic nature of the asphalt layer and the nonlinear anisotropic behavior of the granular base layer are integrated in the mechanistic model. The pavement structure performs in a way that the stress state within each layer depends on the material properties of all pavement layers and the interaction between these layers.

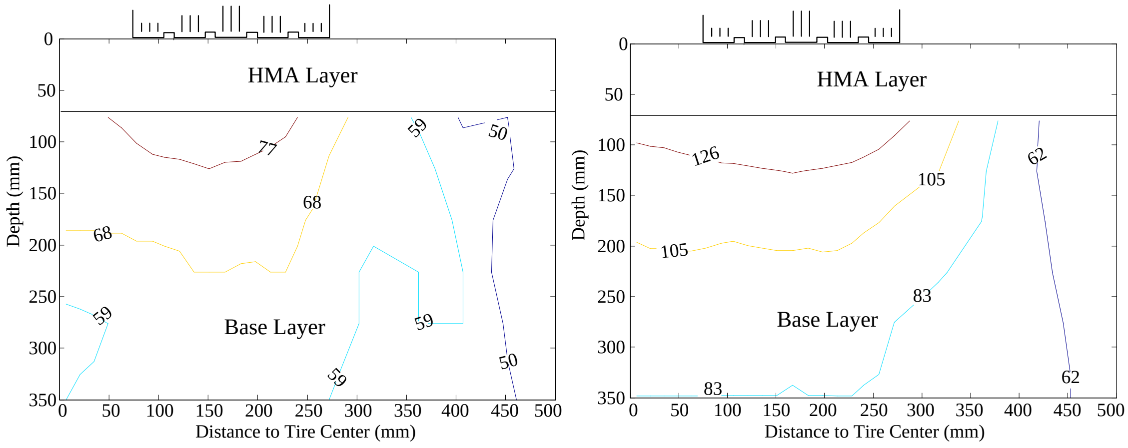

(a) (b)

Figure 5.5 Vertical modulus distributions in base layer under vehicle loading at 80km/h at (a) 25°C and (b) 47°C

5.1.2 Pavement Responses under Moving Load

The examples of stress and strain pulses under a moving load calculated from the FE model are plotted in Figure 5.6, respectively, for the vertical stress, tensile strain, and shear strain. The presented vertical stresses are located under the middle rib of one tire in a dual-tire assembly where the maximum vertical contact stress exists. The presented tensile strains (E11 and E22) are the maximum tensile strains located at the bottom of the asphalt layer. The presented shear strains (E13 and E23) are the maximum shear strains along the depth of the asphalt layer under the tire's outermost ribs where the maximum shear stress exists.

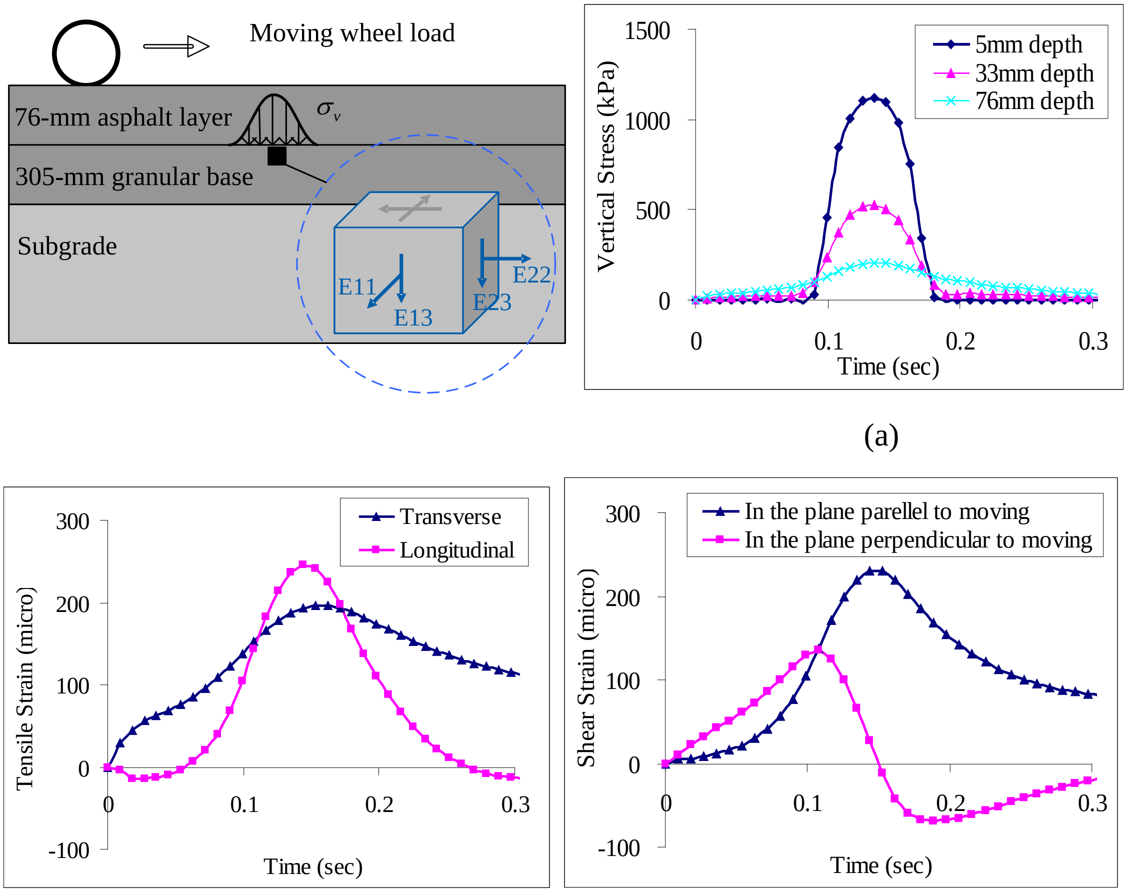

(a)

(b) (c)

Figure 5.6 Stress and strain pulses under moving vehicular loading for (a) vertical stress; (b) tensile strain; and (c) shear strain

As expected, the magnitude of vertical stress dissipates as the depth increases below the pavement surface; while the pulse duration of vertical stress increases with depth because the moving load pattern (approaching and leaving) was simulated in the model. This is particularly important for predicting the responses of the asphalt layer, which has time-dependent properties. The longitudinal strain (E22) is composed of a compressive part followed by a tensile part and another compressive part; while the transverse strain

(E11) is composed of only a tensile part. The shear strain in the plane parallel to the moving direction (E13) has its maximum value when the load is on top of the point of interest; while the shear strain in the plane perpendicular to the moving direction (E23) has a reversed shape under the moving load. The reversed shape of the shear strain is asymmetric due to the viscoelasticity of asphalt material.

The in-depth distributions of tensile strains and shear stresses/strains within the 76-mm asphalt layer caused by the loading of a dual-tire assembly (35.5kN, 724kPa and 8km/h) are shown in Figure 5.7, respectively, at 25°C and 47°C. As expected, the horizontal strain distribution is compressive in the upper half of the asphalt layer and becomes tensile in the lower part of the layer. The highest tensile strain is obtained at the bottom of the asphalt layer at both intermediate and high temperatures. The in-depth distributions of vertical shear stresses and strains are different from the distributions of the horizontal strains. The greatest shear strain within the asphalt layer is located at the shallow depth of the layer. The locations of critical shear strains are consistent with the locations where the horizontal strains change from compression to tension. The vertical shear strain was found having a local-hump near the surface (13-25mm below surface). This is probably caused by the localized distributions of vertical and tangential contact stresses under each tire rib.

As the temperature increases, the tensile strain and shear strain both increase. The increase of shear strain was found more significant than the increase of tensile strain. This indicates that the distortional deformation under vehicular loading becomes predominant in the asphalt layer as the temperature increases. However, the shear stress in the asphalt layer decreases as the temperature increases. This is probably because more stress is carried by the base layer when the asphalt layer becomes soft at high temperatures.

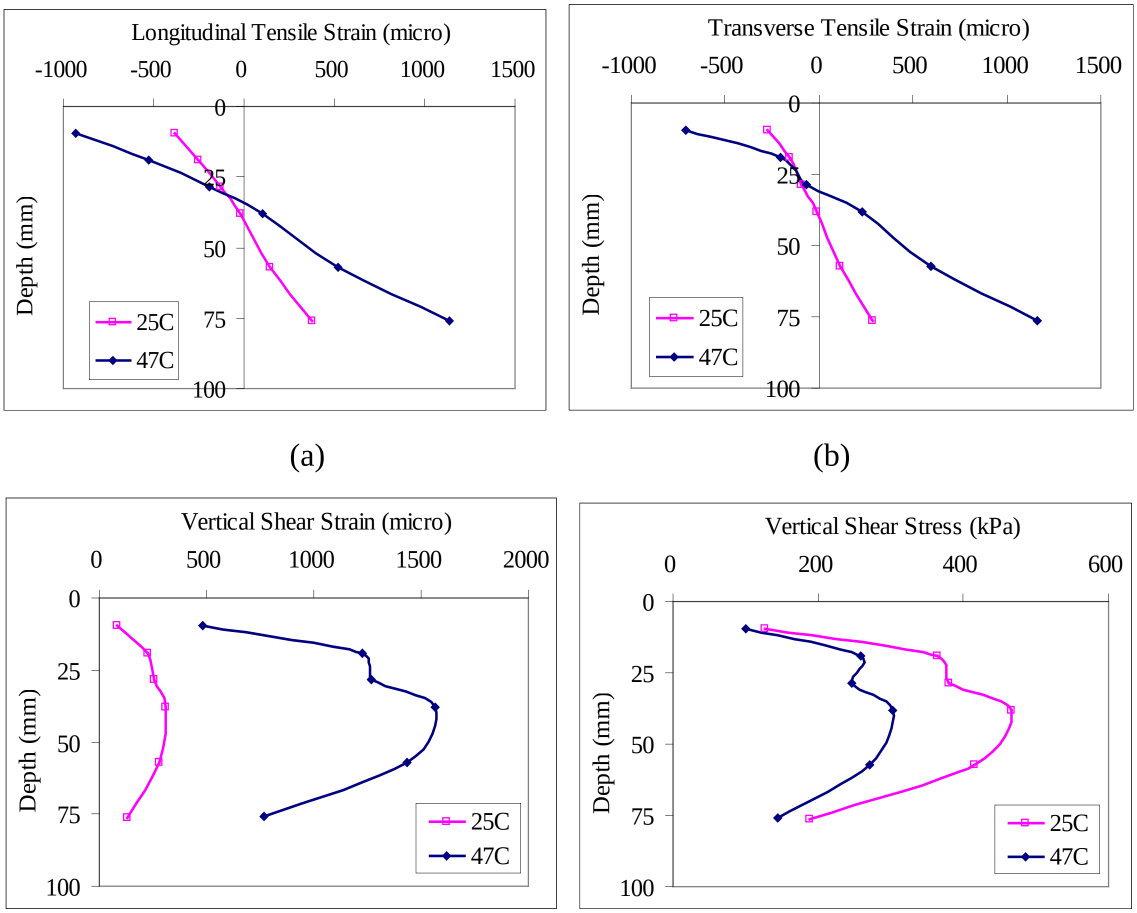

(a) (b)

(c) (d)

Figure 5.7 In-depth strain distributions for (a) longitudinal tensile strain; (b) transverse tensile strain; (c) vertical shear strain; and (d) vertical shear stress

5.1.3 Effect of Base Modulus on Pavement Responses

The linear isotropic, nonlinear isotropic and cross-anisotropic models are used in the analyses to investigate the effect of nonlinear anisotropic behavior of the granular base layer on pavement responses. For the linear isotropic analysis, the selection of elastic modulus could affect the calculation results. In this study, the equivalent elastic modulus was set equal to the average vertical modulus of the base layer under the center of the load from the nonlinear isotropic analysis. The equivalent elastic modulus was approximated to 140MPa at 47°C and 110MPa at 25°C.

Figure 5.8 compares the in-depth distributions of vertical and horizontal stresses in the base layer under the loading of a dual-tire assembly at 25°C and 47°C (35.5kN, 724kPa, and 8km/h), respectively. The results show that the nonlinear anisotropic model eliminates the horizontal tensile stresses in the lower part of the base layer, which is consistent with previous research findings (Tutumluer et al. 2003). This indicates that the nonlinear anisotropic model predicts more realistic stress states in the pavement structure than other models because an unbound granular layer cannot withstand high tensile stresses.

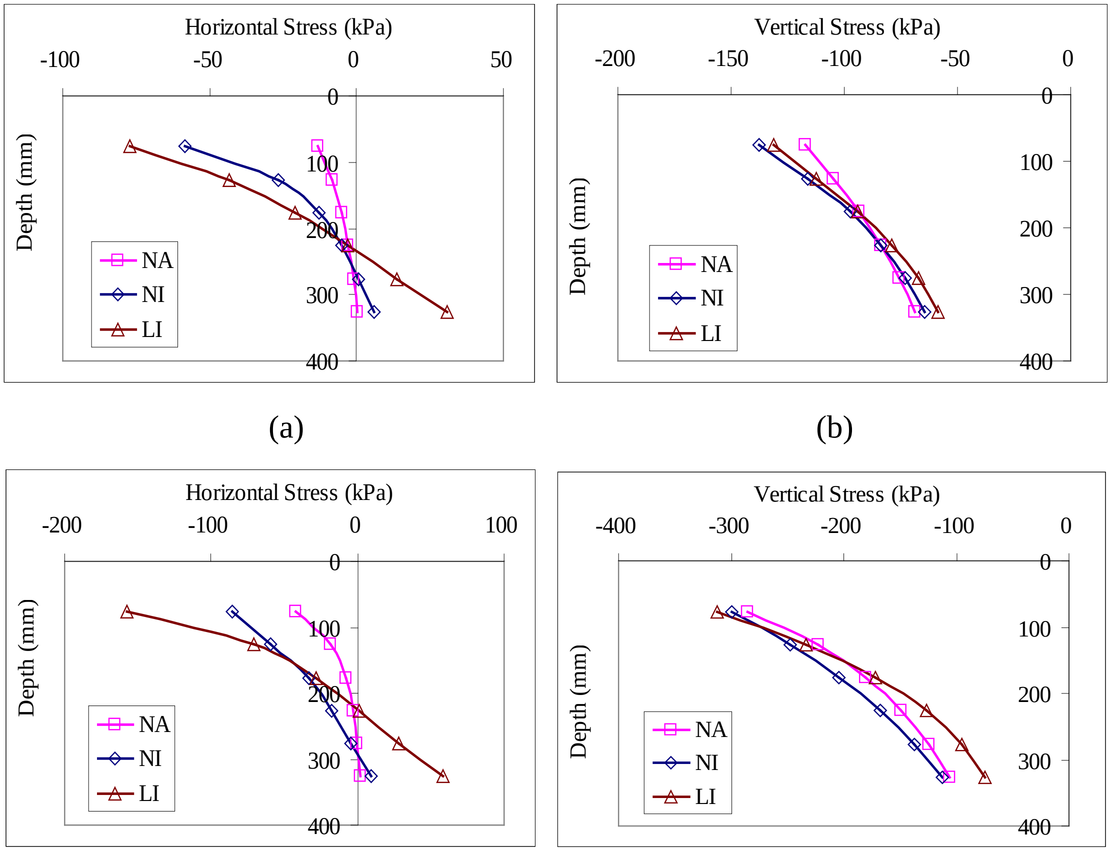

(a) (b)

(c) (d)

Figure 5.8 In-depth distributions of (a) horizontal stress; (b) vertical stress at 25°C; (a) horizontal stress; and (b) vertical stress at 47°C using various base models (NA: nonlinear anisotropic; NI: nonlinear isotropic; and LI: linear isotropic)

The nonlinear anisotropic model results in similar vertical stresses but significant reduction in the confinement stress in the upper part of the base layer, compared to the traditional linear isotropic model. This is consistent with the field measurements reported by Al-Qadi et al. (2007) that significant amounts of horizontal shear displacements were found in the base layer of thin-surfaced asphalt pavement sections, especially in the traffic direction. Previous research has shown that the permanent strain in the base layer increases as the principal stress ratio increases (Kim and Tutumluer 2005). Thus, the linear isotropic model could significantly underestimate the permanent deformation or the shear failure potential in the base layer. In addition, the nonlinear isotropic or anisotropic model results in slightly greater vertical stresses in the lower part of the base layer, compared to the traditional linear isotropic model.

Table 5.1 summarizes the predicted pavement responses at selected positions under the loading of a dual-tire assembly, using various material models for the base layer. For the thin asphalt pavement with a granular base layer, each layer exhibits a unique mode of failure. The tensile strain at the bottom of the thin asphalt layer and shear stress/strain at the shallow depth of the asphalt layer are thought to be related to fatigue cracking and primary rutting, respectively. The compressive strain on the top of the subgrade is thought to be related to secondary rutting due to compression, while the deviatoric stress on the top of the subgrade may indicate shear failure potential for subgrade. At this point, only pavement responses are presented as indicators of pavement damage, considering the limited accuracy and high variability of the parameters used in currently available performance transfer functions.

The results show that the cross-anisotropic stress dependent model results in 24 to 42% greater tensile strains, 10 to 23% greater shear stresses/strains, 16 to 38% greater deviatoric stresses, and 17 to 36% greater compressive strains, compared to the results obtained using the traditional linear isotropic model. Generally, the effect of stress-dependency and cross-anisotropy of the granular base layer becomes more significant as the temperature increases. This is probably because the base layer plays a more important role in the pavement structure as the asphalt layer becomes soft at high temperatures. Therefore, the estimated pavement life due to fatigue cracking or rutting could be much less when the cross-anisotropic stress-dependent model is used for the base layer. This clearly indicates that the effects of cross-anisotropy and stress-dependency of the granular base layer are substantial for accurate pavement performance prediction.

Table 5.1 Comparison of Pavement Responses Using Different Models for Base Layer

Responses	Using different base models at 25°C			Using different base models at 47°C		
	LI	NI	NA	LI	NI	NA
Longitudinal tensile strain at the bottom of asphalt layer (micro)	302	+11%	+24%	916	+23%	+24%
Transverse tensile strain at the bottom of asphalt layer (micro)	228	+15%	+26%	818	+30%	+42%
Maximum shear strain in the asphalt layer (micro)	281	+4%	+11%	1284	+19%	+23%
Maximum shear stress in the asphalt layer (kPa)	426	+4%	+10%	256	+17%	+18%
Deviatoric stress on top of subgrade (kPa)	43	+16%	+16%	58	+38%	+38%
Compressive strain on top of subgrade (micro)	1041	+11%	+17%	1245	+35%	+36%

* LI: linear isotropic; NI: nonlinear isotropic; and NA: nonlinear anisotropic

5.1.4 Effect of Subgrade Modulus on Pavement Responses

Table 5.2 shows the effect of subgrade modulus on the predicted pavement responses at selected positions under the loading of a dual-tire assembly. Two subgrade models were used in the analysis: one is linear model and the other is nonlinear model. When the nonlinear stress-softening model is used, the subgrade modulus varies from 10 to 55MPa, depending on the depth, while the subgrade modulus is constant at 45MPa in the linear model.

The results show that as the nonlinear stress-softening model is used for the subgrade, the pavement responses in the asphalt layer increase 3 to 18%, compared to the results obtained using the linear model. The longitudinal tensile strain at high temperature is the most sensitive response in the asphalt layer to the change of the subgrade modulus. However, the nonlinear model of the subgrade results in 26 to 40% smaller deviatoric stresses but 42 to 124% greater compressive strains on the top of subgrade. This indicates that the stress-softening bahavior of subgrade has more significant effects on the responses in the base layer and subgrade.

Table 5.2 Comparison of Pavement Responses Using Different Models for Subgrade

Responses	Using different subgrade models at 25°C		Using different subgrade models at 47°C	
	Linear	Nonlinear	Linear	Nonlinear
Longitudinal tensile strain at the bottom of asphalt layer (micro)	375	+6%	1139	+18%
Transverse tensile strain at the bottom of asphalt layer (micro)	288	+3%	1162	+6%
Maximum shear strain in the asphalt layer (micro)	311	+4%	1573	+7%
Maximum shear stress in the asphalt layer (kPa)	467	+3%	303	+4%
Deviatoric stress on top of subgrade (kPa)	50	-26%	77	-40%
Compressive strain on top of subgrade (micro)	1151	+42%	1678	+124%

5.2 Influence of Loading Conditions on Pavement Responses

5.2.1 Effect of 3-D Contact Stresses

To evaluate the effect of 3-D contact stresses on thin asphalt pavement responses, two groups of analyses were conducted: one using the 3-D contact stress distribution, and another using the uniform contact stress distribution. Table 5.3 shows the detailed comparison between the two different contact stress distributions. The uniform contact stress was calculated as the total load divided by the actual tire-pavement contact area. The analyses were conducted by loading a dual-tire assembly at a speed of 8km/h under various loads and tire inflation pressures.

Tables 5.4 and 5.5 compare the predicted pavement responses at selected positions using the uniform and 3-D contact stress distributions, respectively, under various loads and tire inflation pressures. The results show that the differences in response between two contact stress distributions depend on the type of response, the asphalt mixture stiffness, and the applied load and tire pressure.

Table 5.3 Comparison between Uniform and 3-D Contact Stress Distributions

Load on dual tires (kN)	Inflation pressure (kPa)	Uniform contact stress (kPa)	3-D contact stresses (kPa)		
			Peak vertical stress (center/inter./edge rib)	Maximum trans. contact stress	Maximum long. contact stress
35.5	414	562	857/626/528	180	257
35.5	724	700	1235/995/606	346	173
35.5	966	869	1530/1212/674	474	107
53.6	724	814	1239/1014/799	335	223
80.4	724	960	1248/1017/1233	324	262

At the intermediate temperature, the 3-D contact stresses induce similar or slightly greater tensile strains at the bottom of the asphalt layer; while at the high temperature, the 3-D contact stresses induce 3 to 19% greater tensile strains at the bottom of the asphalt layer. The 3-D contact stresses also induce slightly greater shear strains and 5 to 25% greater shear stresses in the asphalt layer. Among various responses in the asphalt layer, the shear stress changes most when 3-D contact stresses are used. The effect of 3D contact stresses becomes more significant as the asphalt concrete is softer as temperatures increase. On the other hand, the 3-D contact stresses induce 2 to 11% smaller deviatoric stresses and compressive strains on the top of the subgrade. Therefore, uniform contact stress distribution could underestimate fatigue cracking and primary rutting potential but overestimate permanent deformation potential in the base layer and subgrade.

As the load increases, the response differences using two contact stress distributions have a decreasing trend. This is probably because the vertical contact stress distribution tends to be more uniform as the load increases. Although the 3-D contact stresses cause the greatest differences in responses when the tire inflation pressure is 724kPa, no clear trend was found between the response differences and the level of tire inflation pressure.

On the basis of the calculated response differences using two contact stress distributions (uniform versus 3-D), the pavement responses from traditional pavement analysis could be adjusted for more accurate prediction of pavement performance. This would result in the change of the pavement design thickness or the requirements for the material used in each pavement layer.

Table 5.4 Comparison of Calculated Pavement Responses Using Uniform and 3-D Contact Stresses under Various Loads

Load on dual-tire assembly (kN)	35.5		53.6		80.4	
Contact stress	Uniform	3-D	Uniform	3-D	Uniform	3-D
Pavement responses under 724 kPa at 25°C						
Longitudinal tensile strain at the bottom of asphalt layer (micro)	374	+0%	471	+1%	599	+5%
Transverse tensile strain at the bottom of asphalt layer (micro)	272	+6%	360	+1%	491	+1%
Maximum shear strain in the asphalt layer (micro)	299	+4%	385	+2%	507	+3%
Maximum shear stress in the asphalt layer (kPa)	401	+16%	492	+12%	604	+13%
Deviatoric stress on top of subgrade (kPa)	54	-7%	77	-5%	114	-3%
Compressive strain on top of subgrade (micro)	1246	-8%	1777	-7%	2646	-4%
Pavement responses under 724 kPa at 47°C						
Longitudinal tensile strain at the bottom of asphalt layer (micro)	1057	+8%	1206	+8%	1402	+10%
Transverse tensile strain at the bottom of asphalt layer (micro)	973	+19%	1230	+7%	1553	+3%
Maximum shear strain in the asphalt layer (micro)	1499	+5%	1876	+2%	2454	+1%
Maximum shear stress in the asphalt layer (kPa)	243	+25%	279	+20%	324	+16%
Deviatoric stress on top of subgrade (kPa)	81	-5%	113	-6%	160	-2%
Compressive strain on top of subgrade (micro)	1781	-6%	2468	-5%	3527	-2%

Table 5.5 Comparison of Calculated Pavement Responses Using Uniform and 3-D Contact Stresses under Various Tire Inflation Pressures

Tire inflation pressure (kPa)	414		724		966	
Contact stress	Uniform	3-D	Uniform	3-D	Uniform	3-D
Pavement responses under 35.5-kN loading at 25°C						
Longitudinal tensile strain at the bottom of asphalt layer (micro)	342	-2%	374	+0%	401	-2%
Transverse tensile strain at the bottom of asphalt layer (micro)	259	+1%	272	+6%	294	+1%
Maximum shear strain in the asphalt layer (micro)	274	+0%	299	+4%	325	-3%
Maximum shear stress in the asphalt layer (kPa)	348	+9%	401	+16%	463	+5%
Deviatoric stress on top of subgrade (kPa)	52	-10%	54	-7%	56	-11%
Compressive strain on top of subgrade (micro)	1203	-9%	1246	-9%	1290	-11%
Pavement responses under 35.5-kN loading at 47°C						
Longitudinal tensile strain at the bottom of asphalt layer (micro)	927	+4%	1057	+8%	1159	+4%
Transverse tensile strain at the bottom of asphalt layer (micro)	911	+12%	973	+19%	1109	+13%
Maximum shear strain in the asphalt layer (micro)	1369	+0%	1499	+5%	1620	-2%
Maximum shear stress in the asphalt layer (kPa)	203	+15%	243	+25%	291	+10%
Deviatoric stress on top of subgrade (kPa)	77	-8%	81	-5%	85	-9%
Compressive strain on top of subgrade (micro)	1707	-8%	1781	-9%	1862	-11%

5.2.2 Effect of Wheel Load and Tire Pressure

Tables 5.6 and 5.7 compare the predicted pavement responses at selected positions using the 3-D contact stresses under various wheel loads and tire inflation pressures. As expected, the heavier load or higher tire inflation pressure induces greater pavement responses. The heavy load mainly causes the increase of responses in the subgrade, while the effect of tire inflation pressure is more significant for the responses in the asphalt layer. As the load increases, the vertical contact stress distribution tends to be more uniform and the tire contact area increases significantly. On the other hand, when the tire inflation pressure increases, the high vertical contact stress tends to concentrate in the central region of the tire contact area. This indicates that the responses in the upper part of the pavement are more affected by the localized tire-pavement contact stress distributions. However, deeper in the pavement, the responses are mainly controlled by the total load and contact area.

The results show that the effect of tire inflation pressure is more related to the shear stress in the asphalt layer, compared to other pavement responses. This is probably because, under high tire inflation pressure, the high vertical contact stress in the central region of the tire contact area and the high tangential contact stress could cause more shear flow at tire edges under low confinements. Interestingly, it was found that the load effect is more significant at intermediate temperatures; while the tire inflation pressure effect is more significant at high temperatures. This indicates that the shear-resistant asphalt mixture is desired when the truck tire pressure is high in the regions with warm climates, while the axle weight limit should be enforced during spring seasons on low-volume roads in order to minimize pavement damage.

Table 5.6 Effect of Loads on Calculated Pavement Responses

Pavement responses under 724kPa (Dual-tire Assembly)						
Temperature	At 25°C			At 47°C		
Load on dual tires (kN)	35.5	53.6	80.4	35.5	53.6	80.4
Longitudinal tensile strain at the bottom of asphalt layer (micro)	375	+27%	+67%	1139	+15%	+35%
Transverse tensile strain at the bottom of asphalt layer (micro)	288	+26%	+72%	1162	+14%	+38%
Maximum shear strain in the asphalt layer (micro)	311	+26%	+68%	1573	+22%	+58%
Maximum shear stress in the asphalt layer (kPa)	467	+18%	+46%	303	+11%	+24%
Deviatoric stress on top of subgrade (kPa)	50	+42%	+122%	77	+38%	+104%
Compressive strain on top of subgrade (micro)	1151	+44%	+121%	1678	+40%	+106%

Table 5.7 Effect of Inflation Pressure on Calculated Pavement Responses

Pavement responses under 35.5kN (Dual-tire Assembly)						
Temperature	At 25°C			At 47°C		
Pressure (kPa)	414	724	966	414	724	966
Longitudinal tensile strain at the bottom of asphalt layer (micro)	335	+12%	+14%	960	+19%	+25%
Transverse tensile strain at the bottom of asphalt layer (micro)	261	+10%	+14%	1020	+14%	+23%
Maximum shear strain in the asphalt layer (micro)	274	+14%	+15%	1373	+15%	+16%
Maximum shear stress in the asphalt layer (kPa)	378	+24%	+28%	234	+29%	+37%
Deviatoric stress on top of subgrade (kPa)	47	+6%	+6%	71	+8%	+8%
Compressive strain on top of subgrade (micro)	1090	+4%	+6%	1575	+3%	+2%

It is noted that the pavement responses increase proportionally as the load increases, while the response changes as the tire pressure increases from 414kPa to 724kPa are more significant than the response changes as the tire pressure increases from 724kPa to 966kPa. This is probably due to the variation of localized tire contact stresses as the tire pressure changes. Although the under inflated tire could cause less pavement damage, it would increase fuel consumption and emission due to the increased rolling resistance.

The level of tire loading affects the modulus distribution in the granular base layer. For example, Figure 5.9 plots the distributions of vertical modulus in the base layer under the loading of a 53.6-kN dual-tire assembly. Compared to Figure 5.2, it was found that the base modulus increases by 20 to 30% as the wheel load increases by 50%. This indicates that the pavement responses could be overestimated at a high load or underestimated at a low load without considering the stress-dependency of the modulus of the granular base layer. The effect of tire inflation pressure on the modulus distribution in the base layer, on the other hand, is deemed insignificant.

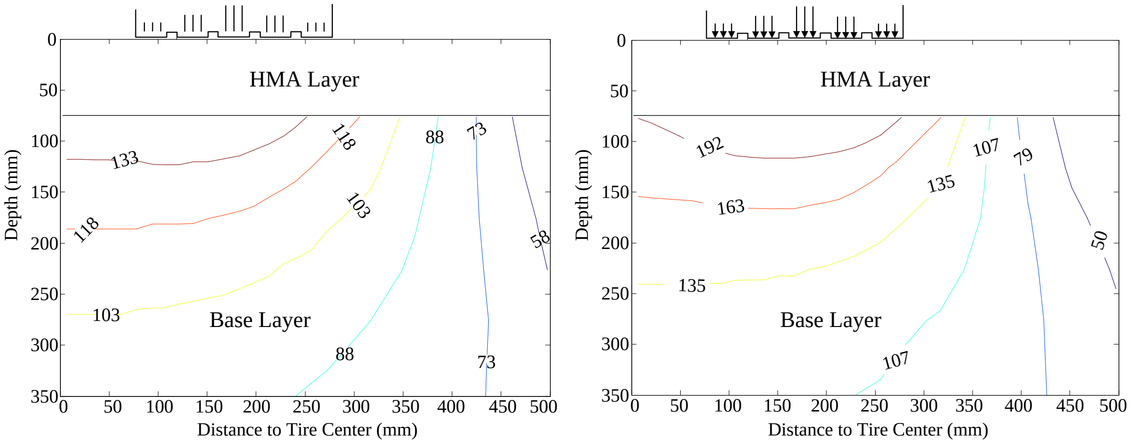

(a) (b)

Figure 5.9 Vertical modulus distributions in base layer under heavy load (53.6kN) at (a) 25°C and (b) 47°C

5.2.3 Effect of Tire Configurations

Table 5.8 compares the predicted pavement responses at selected positions using the measured 3-D tire contact stresses, respectively, under the loading of a dual-tire assembly and a wide-base 455 tire when carrying the same load (35.5kN, 724kPa, and 8km/h). The results show that at 25°C, the wide-base 455 tire results in 19 to 33% greater tensile strains at the bottom of the asphalt layer and similar shear stresses/strains, compared to those induced by the dual-tire assembly. However, at 47°C, the wide-base 455 tire causes 19% greater longitudinal tensile strains; but 11% smaller transverse tensile strains at the bottom of the asphalt layer, compared to those induced by the dual-tire assembly. The wide-base 455 tire also induces 18% smaller shear stresses/strains at the shallow depth of the asphalt layer under tire edges at 47°C.

Table 5.8 Comparison of Pavement Responses under Different Tire Configurations

Pavement Responses	At 25°C		At 47°C	
	Dual	Wide-base	Dual	Wide-base
Longitudinal tensile strain at the bottom of asphalt layer (micro)	375	+19%	1139	+19%
Transverse tensile strain at the bottom of asphalt layer (micro)	288	+33%	1162	-11%
Maximum shear strain in the asphalt layer (micro)	311	+0%	1573	-18%
Maximum shear stress in the asphalt layer (kPa)	467	-3%	303	-18%
Deviatoric stress on top of subgrade (kPa)	50	+8%	77	+21%
Compressive strain on top of subgrade (micro)	1151	+22%	1678	+34%

At intermediate temperatures, the pavement responses in the asphalt layer are more controlled by the load-induced bending effect, while at high temperatures, the asphalt concrete becomes soft and the effect of localized tire contact stresses (vertical and tangential) becomes more significant. Therefore, compared to the dual-tire assembly, the wide-base 455 tire may result in less shear flow at tire edges at high temperatures, because it has the relatively more uniform vertical contact stresses across the contact width and less tangential contact stresses at tire edges.

In addition, the wide-base 455 tire causes 8 to 21% greater deviatoric stresses and 22 to 34% greater compressive strains on the top of the subgrade. This suggests that the impact of wide-base tire on pavement damage depends on the predominant failure mechanisms of the pavement structure. Compared to the conventional dual-tire assembly, the wide-base 455 tire may cause greater fatigue cracking and subgrade rutting potential;

but similar or less primary rutting potential in the asphalt layer. These findings are consistent with the field test findings reported by Pierre et al. (2003) and Greene et al. (2010).

The vertical modulus distributions in the base layer under the loading of a wide-base 455 tire (35.5kN and 724kPa) are shown in Figure 5.10. Compared to Figure 5.2, the wide-base 455 tire results in 15 to 20% greater vertical modulus in the base layer than the dual-tire assembly when carrying the same load. Thus, if the constant linear isotropic modulus is used for the base layer under the loading of two tire configurations (dual versus wide-base), the pavement responses under the loading of a wide-base tire could be overestimated or underestimated. This further necessitates the consideration of nonlinear anisotropic behavior for the granular base layer when predicting thin asphalt pavement responses under various tire loading conditions.

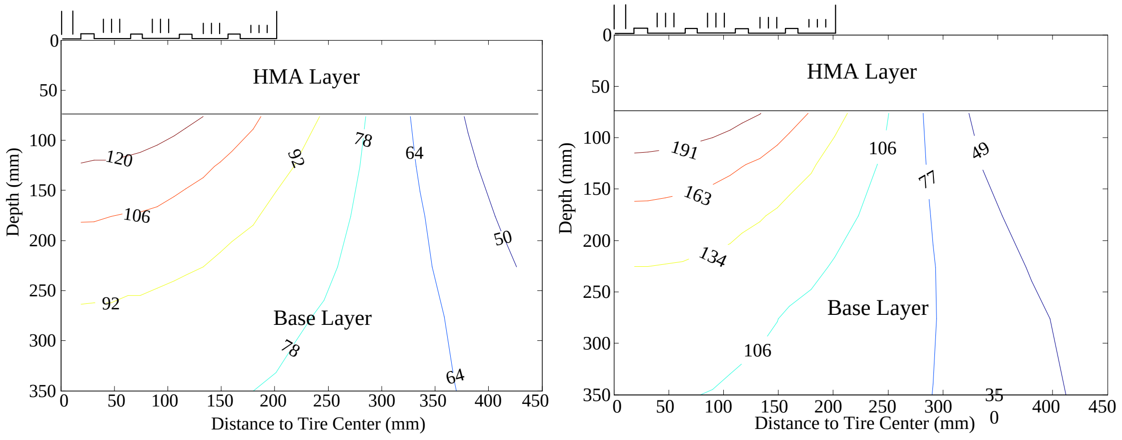

(a) (b)

Figure 5.10 Vertical modulus distributions in base layer using nonlinear anisotropic model under the loading of a wide-base tire at (a) 25°C and (b) 47°C

5.2.4 Effect of Vehicle Maneuvering

Figures 5.11 and 5.12 compare the in-depth distributions of the vertical shear strains at various tire rolling conditions when carrying the same load (35.5kN, 724kPa, and 8km/h). The tire-pavement contact stresses were obtained from the tire-pavement interaction model using a surface friction coefficient of 0.8 at tire braking and slip angle of 5° at tire cornering. At the static loading condition, the maximum shear strains in both planes (parallel and perpendicular to the moving direction) are located at the shallow depth of the asphalt layer. The shear strain in the plane parallel to the moving direction is primarily responsible for the rutting, while the shear strain in the plane perpendicular to the moving direction is related to the shoving/corrugation (as shown in Figure 5.6).

When the tire is braking, the vertical shear strain in the plane perpendicular to the moving direction has the maximum value at the pavement surface (Figure 5.11). This is mainly due to the significant one-directional longitudinal contact stresses caused by tire braking, compared to the reversed longitudinal contact stresses with relatively small magnitudes at the static condition. On the other hand, tire cornering causes 11 to 20% greater shear strain in the plane parallel to the moving direction, compared to the static loading condition (Figure 5.12). This is because tire cornering causes greater vertical and transverse contact stresses and the peak contact stresses shift toward one side of the contact patch. The observations indicate that tire cornering mainly increase the rutting potential, while tire braking mainly increase the shoving/corrugation potential in the asphalt layer.

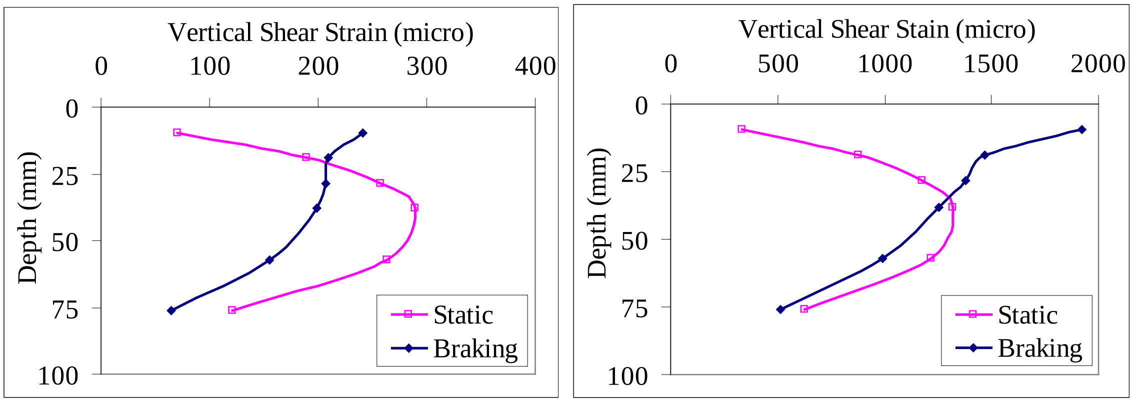

(a) (b)

Figure 5.11 Comparison of vertical shear strains in the plane perpendicular to the moving direction at (a) 25°C and (b) 47°C due to braking

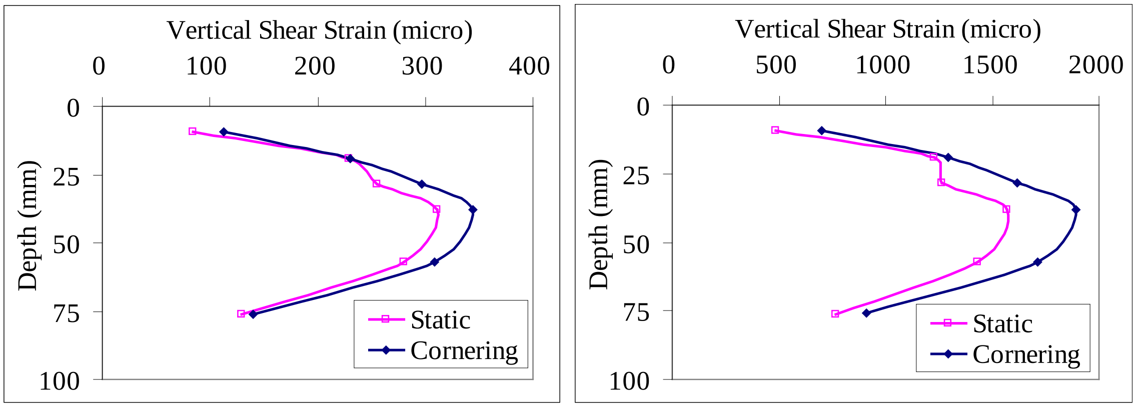

(a) (b)

Figure 5.12 Comparison of vertical shear strains in the plane parallel to the moving direction at (a) 25°C and (b) 47°C due to cornering

Table 5.9 shows the comparisons of other predicted pavement responses at selected positions at various tire rolling conditions. At the intermediate temperature, the tensile strains at the bottom of the asphalt layer and the responses in the subgrade are not significantly affected by vehicle maneuvering behavior. However, compared to the static loading condition, tire braking causes 13% greater longitudinal tensile strains and tire cornering causes 7% greater transverse tensile strains at the bottom of the asphalt layer at the high temperature. These changes are closely related to the high tangential contact stresses generated by vehicle maneuvering. The changes in pavement responses are more significant at high temperatures, which is consistent with the previous findings in this dissertation that the pavement responses are more sensitive to the distributions of tire contact stresses as the asphalt layer becomes soft.

The findings presented here indicate that vehicle maneuvering increases pavement failure potential, especially for the rutting or shoving/corrugation in the asphalt layer at high temperatures. Since the vehicle maneuvering behavior happens frequently at intersections or curved road sections, pavements at these locations need to be designed to withstand more severe loading conditions than regular pavement sections. This could be achieved by constructing the asphalt surface layer using a rut-resistant mix with an adequate shear resistance and stability (cohesive strength and friction angle). For example, the aggregate used in the mix should be carefully selected and should be capable of carrying the load with a stone-to-stone interlock structure. The standard specifications for Superpave volumetric mix design (AASHTO-MP2 2001) requires that the high temperature grade of binder be increased by two grades for standing traffic (< 20km/h) and by one grade for slow traffic (20 to 70km/h) at intersections. Alternative solutions include modifying the binder properties (crumb rubber or styrene-butadiene-styrene (SBS), for instance). Regardless of the mix design approach used, shear testing should be conducted to ensure the suitability of the mix for application at intersections or curved road sections.

Table 5.9 Comparison of Pavement Responses due to Vehicle Maneuvering

Responses	Tire Loading at 25°C			Tire Loading at 47°C		
	Static	Braking	Cornering	Static	Braking	Cornering
Longitudinal tensile strain at the bottom of asphalt layer (micro)	375	-1%	-3%	1139	+13%	-2%
Transverse tensile strain at the bottom of asphalt layer (micro)	288	-3%	+2%	1162	-5%	+7%
Deviatoric stress on top of subgrade (kPa)	50	+2%	+0%	77	+5%	-1%
Compressive strain on top of subgrade (micro)	1151	+0%	+1%	1678	+1%	+1%

5.3 Summary

The analysis results presented in this chapter indicate that accurate pavement responses can only be predicted when the viscoelastic nature of the asphalt layer and the nonlinear anisotropic behavior of the granular base layer are integrated into the mechanistic model. The modulus distribution in the base layer is not only affected by the wheel load, but also affected by the temperature and vehicle speed due to the viscoelastic nature of the asphalt surface layer. In addition, it was found that cross-anisotropic stress dependent behavior of the base layer should be considered; otherwise critical pavement responses in thin asphalt pavements could be underestimated, especially at high temperatures. However, the stress-softening behavior of subgrade mainly affects the responses in the subgrade.

The critical pavement responses in thin asphalt pavements at various tire loading and rolling conditions were analyzed. It is concluded that compared to the uniform contact stress distribution, the 3-D tire contact stresses cause greater fatigue cracking and primary rutting potential but less failure potential in the subgrade. The calculation of pavement responses are affected by the vehicle loading (wheel load and tire inflation pressure), tire configuration (dual-tire assembly and wide-base tire), and vehicle maneuvering behavior (braking/acceleration and cornering). Generally, the pavement responses are more sensitive to the distributions of tire contact stresses as the asphalt layer becomes soft at high temperatures.

CHAPTER 6 NEAR-SURFACE FAILURE POTENTIAL OF THICK ASPHALT PAVEMENT

6.1 Near-Surface Strain Responses in Thick Asphalt Pavement

Long-lasting or perpetual pavement is designed to prevent cracks from initiating at the bottom of the asphalt layer by increasing the asphalt layer thickness or placing a binder-rich layer as the lowest asphalt layer (Newcomb 2001). However, surface-related cracking has recently been observed at the surface or near-surface of thick asphalt pavements or overlays as a premature failure. Therefore, it is important to examine the pavement responses that are related to the failure at the pavement near-surface.

Table 6.1 summarizes the contributing load-related parameters to the surface-initiated cracking that were investigated in the literature. It shows that both the tensile and shear stresses/strains are thought to be related to the near-surface failure, although the analysis approaches, contact stress assumptions, and material models differ in the literature.

Table 6.1 Mechanisms of Surface-Initiated Cracking in the Literature

Literature	Contributing parameters to surface-initiated cracking
Merrill (2000) and Thom (2003)	Tensile strain at tire edge
Groenendijk (1998); Myers et al. (1998); Svasdisant (2002); Soon et al. (2003)	Surface tensile stress around tire edge (plus aging and thermal stress)
Bensalem et al. (2000); Yoo and Al-Qadi (2008); and Al-Qadi et al. (2008)	Load-induced shear strain at tire edge
CROW (1990); Wang and Al-Qadi (2009)	Octahedral shear stress or distortional energy

In this chapter, the thick asphalt pavement section with a 254-mm-thick asphalt layer, described in Chapter 4, is used in the analysis. Figure 6.1 shows the strain distributions along the tire width at the pavement near-surface (13-25mm below surface) under the loading of a dual-tire assembly (35.5kN, 724kPa, 8km/h, and 25°C), respectively, for the maximum tensile strain and the vertical shear strain. The greatest surface tensile strains were found located at some distance away from tire edges, especially the inner tire edges. However, the magnitudes of the surface tensile strains are small compared to the possible endurance limit of asphalt concrete (70-100micro) for fatigue cracking (Carpenter et al. 2003). This indicates that the surface-initiated cracking cannot be induced by surface tensile strains only and the effect of shear strains cannot be neglected. On the other hand, the calculated near-surface shear strains are greater than the surface tensile strains and show a fluctuating pattern under tire ribs and grooves. The maximum near-surface shear strain was found not under the edge ribs, but under the inner ribs, where the maximum transverse tire-pavement contact stress exists.

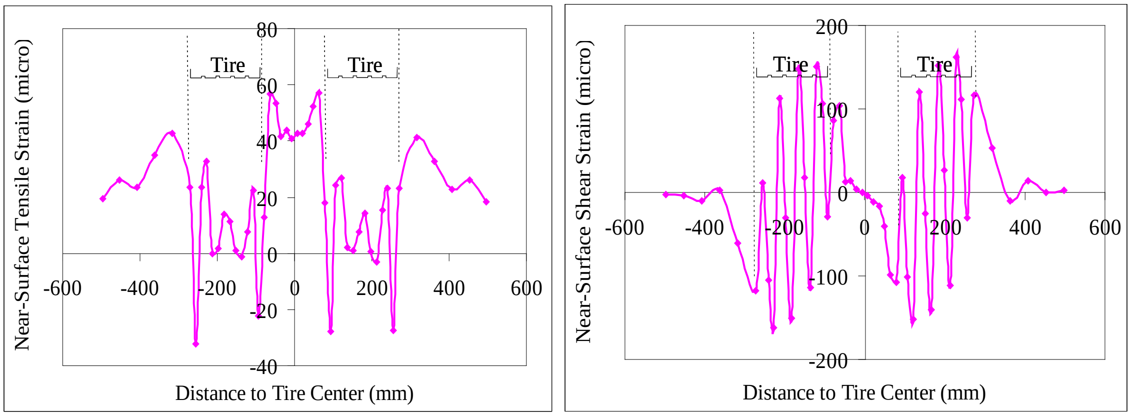

(a) (b)

Figure 6.1 Transverse distributions of (a) maximum tensile strains; and (b) vertical shear strains at the pavement near-surface

Figures 6.2 and 6.3 compare the transverse distributions of tensile and shear strains at the pavement near-surface under various tire loading conditions (35.5kN, 724kPa, 8km/h, and 25°C). Compared to the uniform contact stress distribution, the 3-D contact stresses induce greater tensile and shear strains under tire ribs, but similar tensile and shear strains at the vicinity of tire edges (Figure 6.2). Compared to the dual-tire assembly, the wide-base 455 tire induces smaller tensile and shear strains at the pavement near-surface (Figure 6.3). This indicates that the strain responses at the pavement near-surface are affected by the localized tire-pavement contact stress distributions.

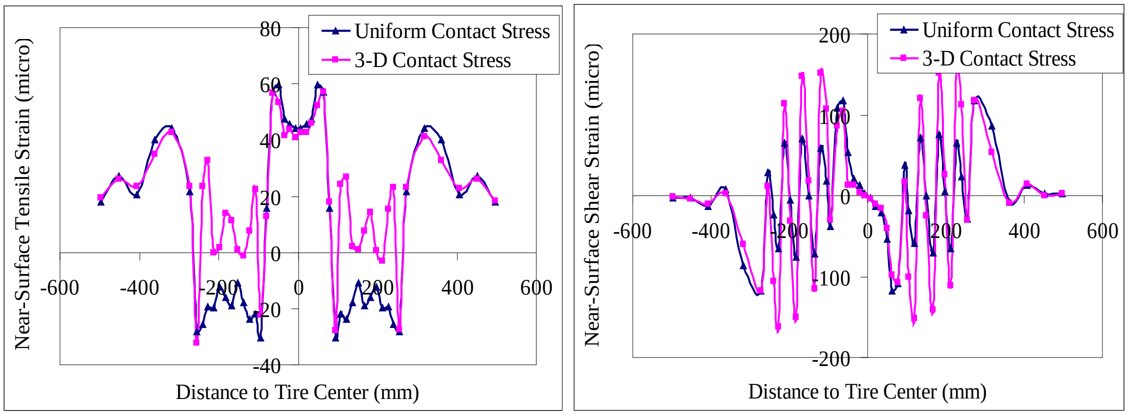

(a) (b)

Figure 6.2 Effect of 3-D contact stresses on (a) maximum tensile strains; and (b) vertical shear strains at the pavement near-surface

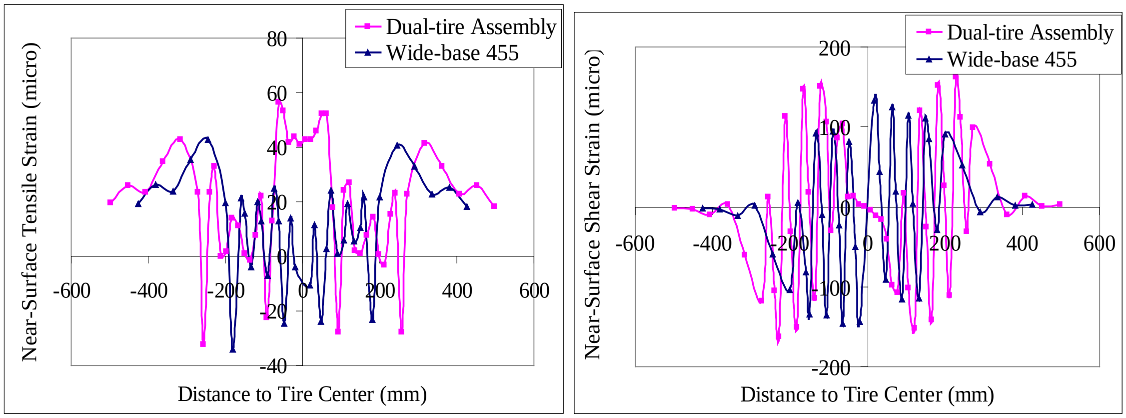

(a) (b)

Figure 6.3 Effect of wide-base tire on (a) maximum tensile strains; and (b) vertical shear strains at the pavement near-surface

Table 6.2 compares the strain ratios predicted from this study and the strain ratios measured by Greene et al. (2010) in the accelerated pavement testing. The strain ratios are calculated as the responses caused by the wide-base 455 tire divided by the responses caused by the dual-tire assembly. In the testing, the surface tensile strains under various tire configurations were measured using the foil-type strain gauge. The testing was conducted at two loading speeds (3.2 and 12.8kph) and the temperature was held constant at 50°C. The comparison shows that a similar trend is observed between the model predictions and field measurements although the asphalt layer thicknesses are different.

Table 6.2 Strain Ratios Caused by the Wide-base 455 Tire with respect to the Dual- tire Assembly

Sources	Asphalt layer thickness (mm)	Tensile strain ratio	Shear strain ratio
Prediction from this study	254	0.75-78	0.9
APT measurements (Greene et al. 2010)	130	0.6-0.8	N/A

The effects of load and tire inflation pressure on the responses at the pavement near-surface are shown in Figures 6.4 and 6.5. It was found that the heavy load mainly increases the tensile strain at the vicinity of tire edges; while the high tire inflation pressure mainly increases the shear strain under the tire center. This is due to the fact that the increase of wheel load mainly increases the vertical contact stresses under tire edge ribs, while the increase of tire pressure mainly increases the vertical and transverse contact stresses under tire center ribs.

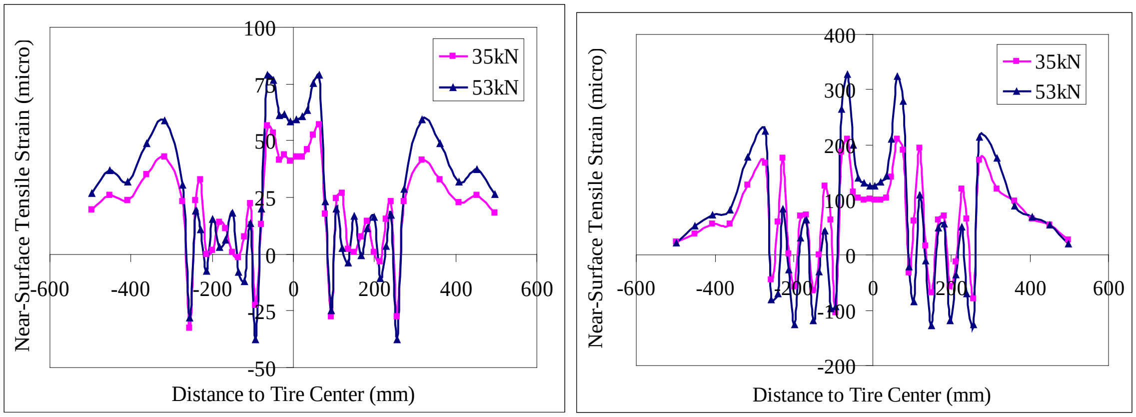

(a) (b)

Figure 6.4 Effect of heavy load on maximum tensile strains at (a) 25°C; and (b) 45°C at the pavement near-surface

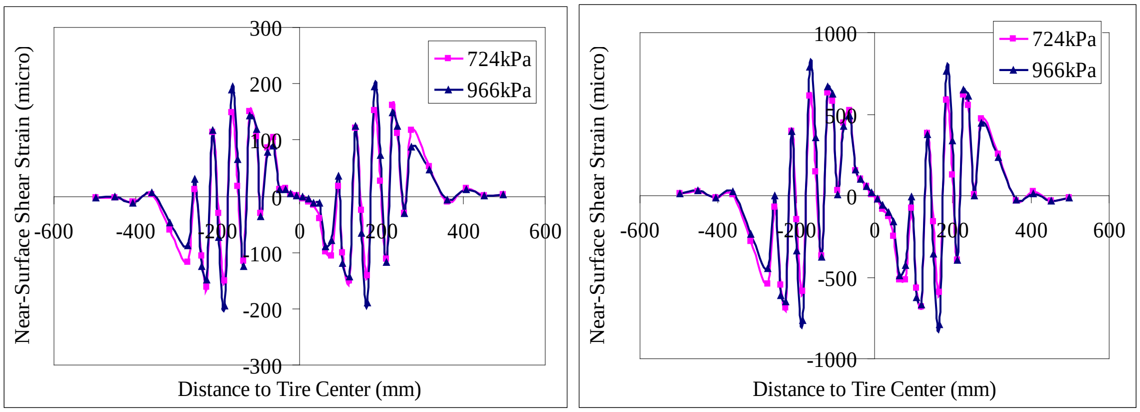

(a) (b)

Figure 6.5 Effect of high tire inflation pressure on vertical shear strains at (a) 25°C; and (b) 45°C at the pavement near-surface

The effects of vehicle maneuvering on the responses at the pavement near-surface are shown in Figures 6.6 and 6.7. As the tire is braking, the tensile strains in the contact area increase due to the increased longitudinal contact stresses under each rib; while as the tire is cornering, the shear strains under the center or intermediate rib of the tire increase due to the increased vertical and transverse contact stresses. Similar to the findings for thin asphalt pavements, the effect of vehicle maneuvering on the near-surface responses of thick asphalt pavements becomes more significant at high temperatures.

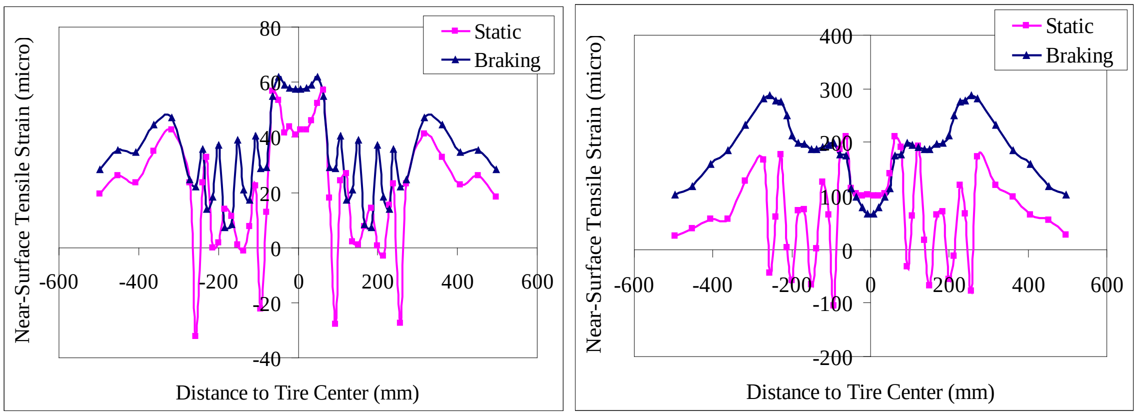

(a) (b)

Figure 6.6 Effect of tire braking on maximum tensile strains at (a) 25°C; and (b) 45°C at the pavement near-surface

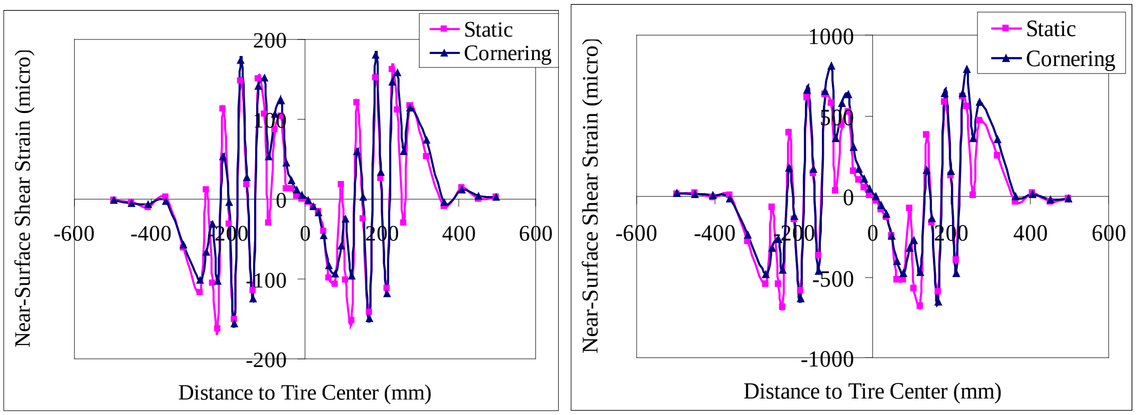

(a) (b)

Figure 6.7 Effect of tire cornering on vertical shear strains at (a) 25°C; and (b) 45°C at the pavement near-surface

Table 6.3 summarizes the pavement tensile and shear strains at near-surface resulted from critical loading conditions, with respect to the normal loading condition (35.5kN, 724kPa, and 8km/h). It clearly shows that the tensile and shear strains vary depending on the loading conditions. Particularly, tire braking causes 9-37% greater tensile strains, while tire cornering causes 12-18% greater shear strains at the pavement near-surface when carrying the same load. This indicates that the responses at the pavement near-surface are significantly affected by the localized contact stress distributions at the tire-pavement interface and the effect of vehicle maneuvering is important.

Table 6.3 Near-surface Strains Caused by Critical Loading Conditions

Case	Load (kN)	Pressure (kPa)	Vehicle maneuvering	Tensile strain (micro)		Shear strain (micro)	
				25°C	45°C	25°C	45°C
1	35.5	724	No	57	162	210	686
2	35.5	966	No	55	185	210	787
3	53.6	724	No	79	170	327	850
4	35.5	724	Braking	62	117	288	582
5	35.5	724	Cornering	59	181	239	808

6.2 Near-Surface Failure Potential under Multi-Axial Stress State

6.2.1 Failure Criteria under Multi-Axial Stress State

Each cubic element within a pavement structure experiences a stress pulse caused by a passing vehicle loading. This stress pulse has two components at each orthogonal plane: normal stress and shear stress. If the element is rotated in such a way that there are zero shear stresses acting on the element, then the normal stresses acting on these planes are called the principal stresses (Figure 6.8).

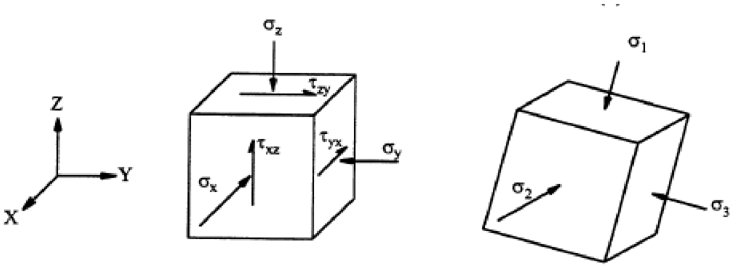

Figure 6.8 General stress sate and principal stress state in a cubic element

The reality of the tire-pavement interaction is that truck tires produce highly non-uniform vertical contact stresses, as well as surface tangential stresses under each tire rib. This creates a complex 3-D stress state near the pavement's surface. Figure 6.9 illustrates the schematic plot of stress states in the maximum and minimum principal stress planes at the pavement near-surface under the loading of a dual-tire assembly. It is obvious that various multi-axial stress states exist, depending on the relative locations with respect to the tire. The greatest compressive stresses were found located under the tire center rib, while the greatest tensile stresses were found within the area between dual tires or at some distance laterally away from tire edges. The highest magnitudes of shear stresses are located at the vicinity of tire edges or under the grooves between adjacent tire ribs.

Therefore, rather than considering one-dimensional tensile or shear stresses only, the multi-axial stress states need to be considered when analyzing the material failure potential at the pavement near-surface. The complex 3-D stress state at the pavement near-surface also suggests that near-surface failure potential of asphalt mixtures can be better evaluated using the experimental methods that can simulate multi-axial stress states, such as the triaxial test or hollow cylinder test.

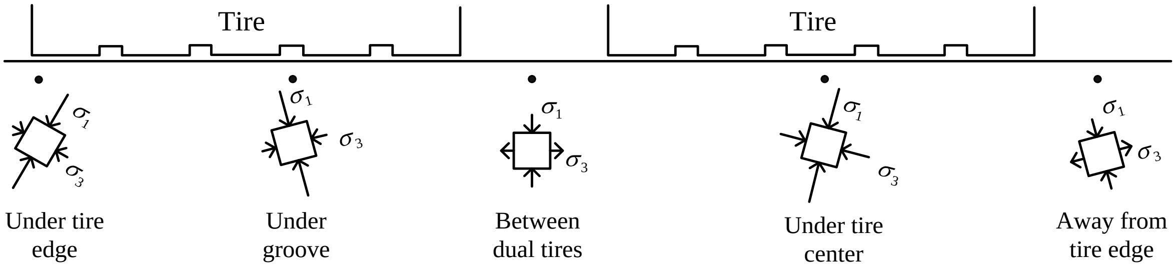

Figure 6.9 Schematic illustration of multi-axial stress sates at the pavement near-surface (Compression: positive and tension: negative)

The failure of asphalt mixture at intermediate and high temperatures is regarded as ductile failure due to the creep deformation of the asphalt mixture. Several failure theories can consider multi-axial stress states for ductile materials; they include maximum shear stress criterion (Tresca criterion), Equation 6-1; maximum octahedral shear stress (maximum distortional energy criterion or von Mises criterion), Equation 6-2; Mohr-Coulomb criterion, Equation 6-3; and Drucker-Prager criterion, Equation 6-4 (Doweling 1999).

$$\max\left(\left|\sigma_1-\sigma_3\right|,\left|\sigma_1-\sigma_2\right|,\left|\sigma_2-\sigma_3\right|\right)=\sigma_y \tag{6-1}$$

$$(\sigma_1-\sigma_2)^2+(\sigma_2-\sigma_3)^2+(\sigma_1-\sigma_3)^2=2\sigma_y^2 \tag{6-2}$$

$$(\frac{\sigma_1+\sigma_3}{2})\sin\phi-\left(\frac{\sigma_1-\sigma_3}{2}\right)+c\cdot\cos\phi=0 \tag{6-3}$$

$$\sqrt{\frac{1}{6}\left[(\sigma_1-\sigma_2)^2+(\sigma_2-\sigma_3)^2+(\sigma_1-\sigma_3)^2\right]}=\frac{6c\cdot\cos\phi}{\sqrt{3}(3-\sin\phi)}+\frac{2\sin\phi}{\sqrt{3}(3-\sin\phi)}(\sigma_1+\sigma_2+\sigma_3) \tag{6-4}$$

where σ_1, σ_2, and σ_3 are maximum, middle, and minimum principal stresses; τ is maximum shear stress (shear strength); σ_y is yield stress in uniaxial tension; ϕ is angle of friction; and c is cohesive strength.

The selection of the failure criteria depends on the distress mode and the stress state in the pavement structure. Freeman and Carpenter (1990) have used the octahedral shear stress as the indicator for a total stress state in the asphalt layer responsible for premature deformation. Ameri-Gaznon and Little (1990) applied the octahedral shear stress theory to the design of asphalt overlays. The octahedral shear stress is independent of the first stress invariant, and thus, it is applicable for indicating the shear flow potential of asphalt concrete without considering volumetric deformation. However, the octahedral shear stress criterion shows no hydrostatic pressure dependence and failure is therefore a function of only shear.

The Mohr-Coulomb failure criterion is widely used in soil mechanics. Asphalt mixtures are composed of aggregate, asphalt, and air, and are analogous to soils composed of soil solids, water, and air. At intermediate-to-high temperatures, the asphalt concrete may be modeled as Mohr–Coulomb materials with both cohesive and granular properties. However, the Mohr-Coulomb criterion ignores the effects of the intermediate principal stress and represents an irregular hexagonal pyramid in the stress space. The Drucker-Prager model is a smooth version of the Mohr–Coulomb model because it modifies the Mohr-Coulomb yield function to avoid singularities associated with corners. Both Mohr–Coulomb and Drucker–Prager criteria are pressure dependent models and consider the compressive strength of the material is much greater than its tensile strength. They have been used in this study to compare failure potential at the pavement near-surface under various loading conditions. However, both models may not capture the distinction between asphalt concrete damage behavior under compression and extension (not necessarily tension) loading conditions (Masad et al. 2005). .

The parameters c and ϕ in Mohr–Coulomb and Drucker–Prager criteria are typically obtained from triaxial strength tests conducted at various confinement levels. Generally, c is equal to zero for pure granular material, while ϕ is equal to zero for pure cohesive material. For asphalt mixtures, the parameters c and ϕ can be obtained from a combination of unconfined tensile and compressive strength tests. A simple linear relationship has been found between the cohesion parameter and the indirect tensile strength of asphalt concrete (Gokhale et al. 2005).

The strength of asphalt concrete develops from both cohesion and the frictional resistance. Cohesion is caused by the viscosity of asphalt binder and affected by the binder grade and content; while the friction comes from the aggregate shape, texture, and the interlock of aggregate skeleton. Previous research has shown that the friction angle of asphalt concrete is relatively independent of test temperature and strain rate, whereas the cohesion coefficient of asphalt concrete decreases as the test temperatures increases or the strain rate decreases (Tan et al. 1994). In this study, for the purpose of evaluating the failure potential at the pavement near-surface under vehicular loading, the strength parameters of asphalt concrete are assumed at a friction angle of 40^o and a cohesion of 400kPa at 45ºC and 600kPa at 25ºC depending on the mix characteristics (Gokhale et al. 2005; Hajj et al. 2007).

6.2.2 Calculation of Shear Stress Ratio

The Mohr-Coulomb theory is usually represented by using Mohr's circles, Figure 6.10(a). Instead of plotting a series of Mohr's circles, it is mathematically convenient to plot the states of stress as points in a $p-q$ diagram, Figure 6.10(b). The Mohr-Coulomb failure envelope with strength parameters (c and ϕ) can be defined by Equations 6-5 and 6-6. The relationship between the unconfined tensile and compressive strengths and the strength parameters can be expressed using Equations 6-7 and 6-8.

$$\tau = c + \sigma tg\ \phi \tag{6-5}$$

$$q = a + ptg\ \alpha \tag{6-6}$$

with $c \cdot \cos\phi = a$ and $\sin\phi = tg\alpha$

$$S_u = \frac{2c \cdot \cos\phi}{1 - \sin\phi} \tag{6-7}$$

$$S_t = \frac{2c \cdot \cos\phi}{1 + \sin\phi} \tag{6-8}$$

where τ is shear stress at failure (shear strength); σ is normal stress at failure; p is normal stress at failure with $p = \frac{1}{2}(\sigma_1 + \sigma_3)$; q is shear stress at failure with $q = \frac{1}{2}(\sigma_1 - \sigma_3)$; S_u is unconfined compressive strength; S_t is unconfined tensile strength; ϕ is angle of friction; and c is cohesive strength.

The Mohr-Coulomb failure criterion states that the failure of a material, either by fracture or by the onset of yielding, will occur when a Mohr's circle reaches its failure envelope. The closeness of the stress state to the failure envelope can be interpreted as a stress ratio-"the actual shear stress divided by the critical shear stress at the same normal stress." This stress ratio is calculated in Equation 6-9, as shown in Figure 6.10(b). A stress ratio below 100% means that the material does not fail. Therefore, the stress ratio provides a measure of the closeness of a multi-axial stress state to the critical failure envelope.

$$\text{Stress Ratio} = \frac{q}{q_{failure}} = \frac{q}{a + ptg\alpha} = \frac{\sigma_1 - \sigma_3}{2c \cdot \cos\phi + (\sigma_1 + \sigma_3)\sin\phi} \tag{6-9}$$

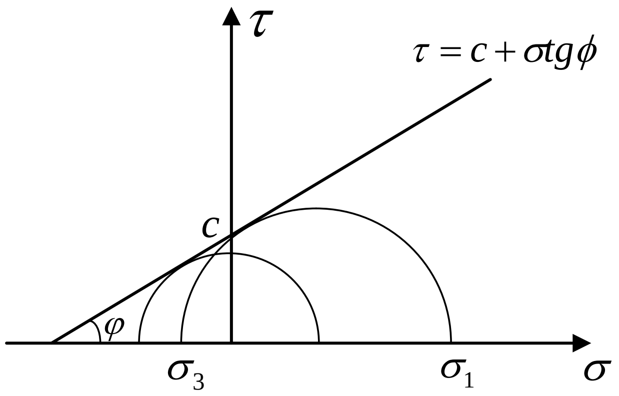

(a)

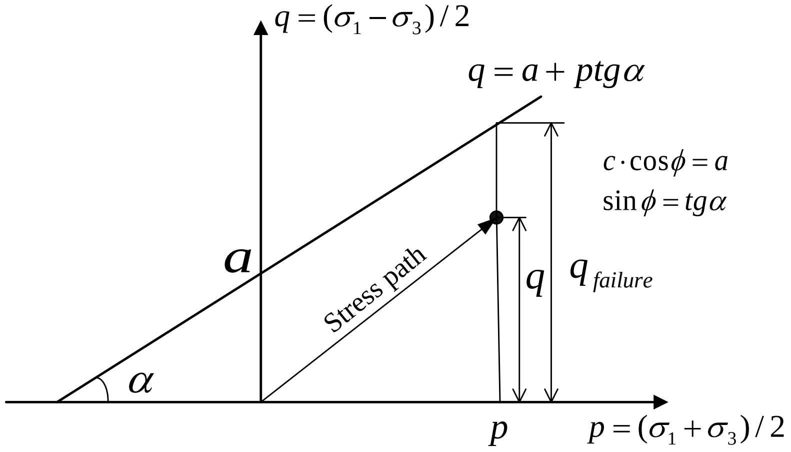

(b)

Figure 6.10 Representations of Mohr-Coulomb failure criterion in (a) Mohr's circles and (b) p-q diagram (compression: positive and tension: negative)

The Drucker-Prager failure envelope can be plotted as a straight line in the $p-q$ diagram, as defined in Equation 6-10. Similarly, the shear stress ratio is defined as the ratio of the applied shear stress divided by the shear stress at failure at the same level of the mean normal stress, as shown in Equation 6-11 (Figure 6.11).

$$q = Ap + B \tag{6-10}$$

$$\text{with } A = \frac{6\sin\varphi}{3-\sin\varphi} \text{ and } B = \frac{6c\cdot\cos\varphi}{3-\sin\varphi}$$

$$\text{Stress Ratio } = \frac{q}{q_{failure}} = \frac{q}{Ap+B} = \frac{\sqrt{3J_2}\,(3-\sin\varphi)}{2I_1\sin\varphi + 6c\cos\varphi} \tag{6-11}$$

where p is the mean normal stress at failure with $p = \frac{1}{3}I_1 = \frac{1}{3}(\sigma_1 + \sigma_2 + \sigma_3)$; q is the shear stress at failure with $q = \sqrt{3J_2} = \frac{1}{6}\left[(\sigma_1 - \sigma_2)^2 + (\sigma_2 - \sigma_3)^2 + (\sigma_1 - \sigma_3)^2\right]$; I_1 is the first stress invariant; J_2 is the second invariant of deviatoric stress; ϕ is the angle of friction; and c is the cohesive strength.

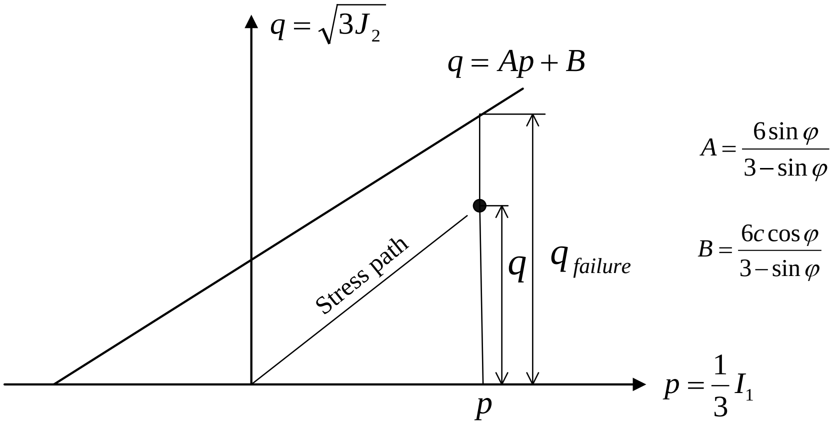

Figure 6.11 Representation of Drucker-Prager failure criterion in p-q diagram (compression: positive and tension: negative)

6.2.3 Stress Invariants at Pavement Near-Surface

Figures 6.12 and 6.13 show the load-induced multi-axial stress states that occur at a depth of 50mm under the pavement surface, respectively at 25ºC and 45ºC. The loading is represented by the measured 3-D tire contact stresses under a dual-tire assembly (35.5kN, 724kPa, and 8km/h). The figures show that similar stress distributions but different stress magnitudes were found when using the Mohr–Coulomb and Drucker–Prager criteria, respectively.

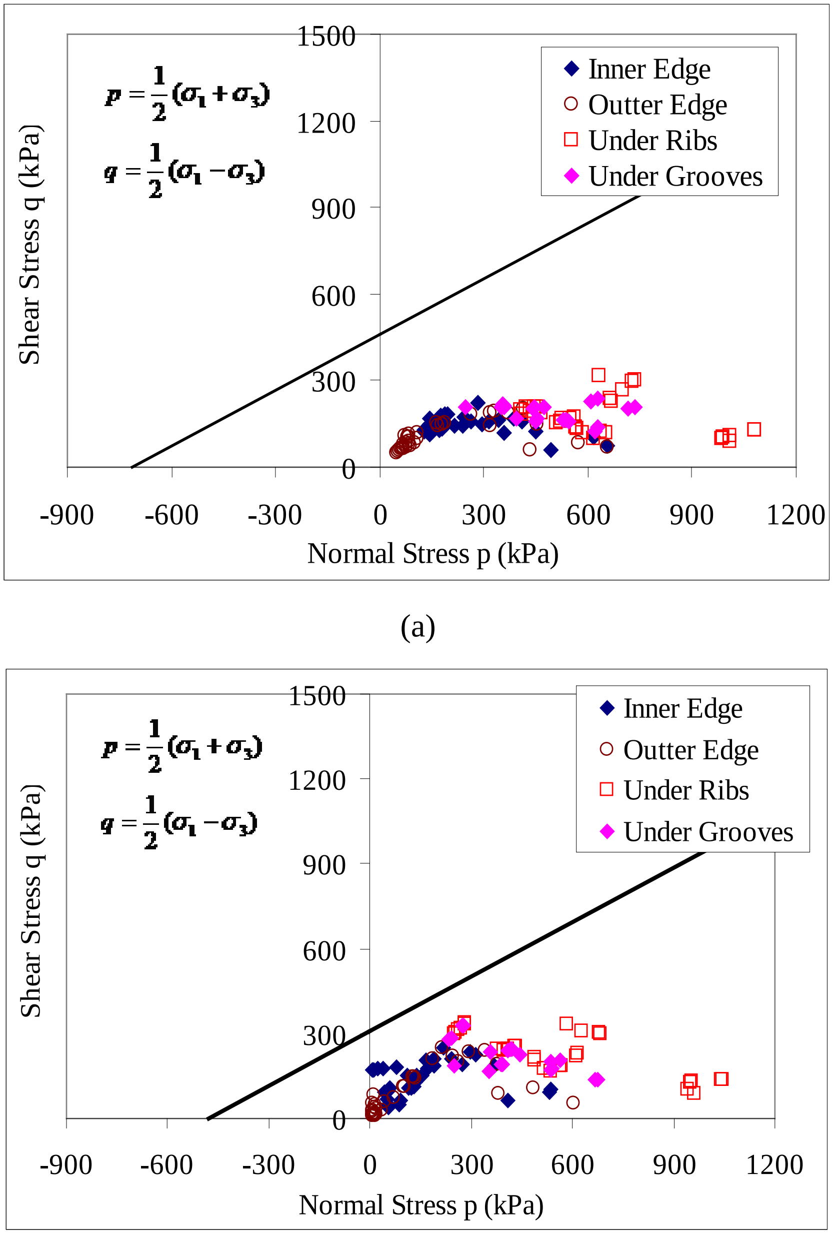

(a)

(b)

Figure 6.12 Stress invariants at the pavement near-surface using Mohr-Coulomb failure criteria at (a) 25ºC; and (b) 45ºC

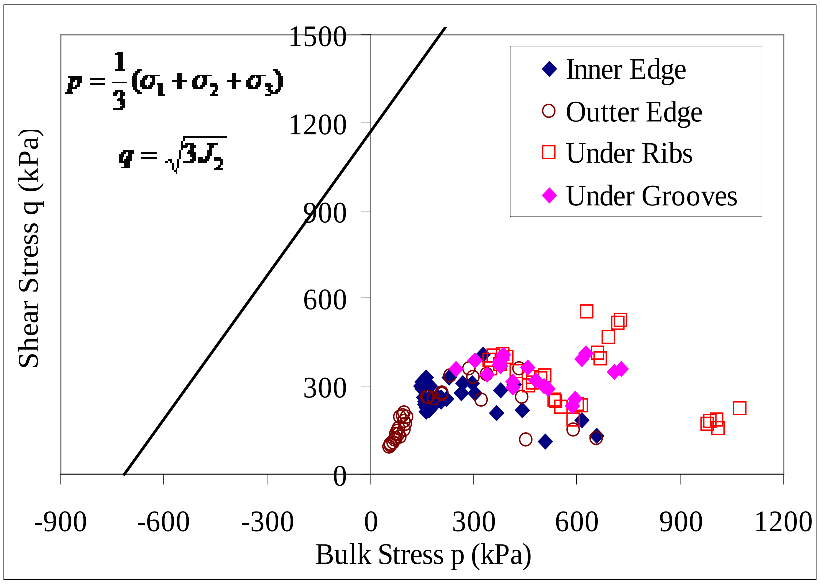

(a)

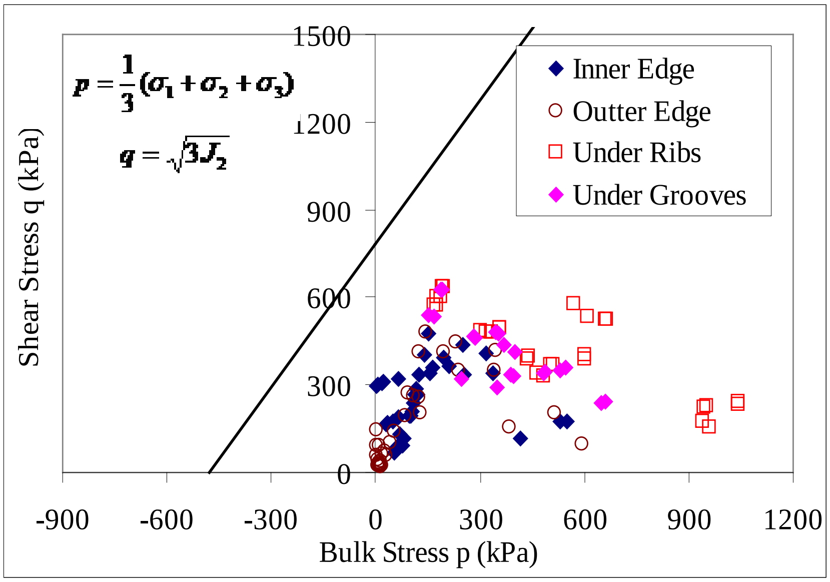

(b)

Figure 6.13 Stress invariants at the pavement near-surface using Drucker-Prager failure criteria at (a) 25ºC; and (b) 45ºC

It is noted that the stress state with the greatest failure potential depends on the combination of normal (or bulk) and shear stress and does not necessarily occur at the location where maximum shear stress or maximum compressive stress occurs. As the temperature increases, the maximum shear stress increases while the maximum normal (or bulk) stress keeps relatively constant. This indicates that the shear effect becomes more significant at high temperatures. At some locations, the shear stresses are greater than the normal stresses, which results in producing critical stress states close to the failure envelope. Interestingly, no negative normal stress state was found at the pavement near-surface. This indicates that the failure at the pavement near-surface is more like shear failure instead of tensile failure for thick asphalt pavements.

As expected, the vehicle load would not cause pavement failure due to one-pass loading because of the relatively lower stress compared to the failure envelope. After repetitive loading, the damage can accumulate because the material stiffness is reduced and the stress may reach the failure envelope. Instead of implementing a full plastic and damage model, the stress ratio under one-pass loading is used in this study to evaluate the failure potential at the pavement near-surface.

6.2.4 Near-Surface Pavement Shear Failure Potential

The critical failure locations in the asphalt layer can be determined by plotting contours of the calculated shear stress ratios. Figures 6.14(a) and (b) plot the calculated stress ratios within the asphalt layer under the loading of a dual-tire assembly at 25ºC (35.5kN, 724kPa, and 8km/h), respectively, using the Mohr–Coulomb and Drucker–Prager criteria. Due to the symmetry of dual tires, only the asphalt layer under one tire of the dual-tire assembly was plotted. The stress ratio contours have the similar trends when using the two failure criteria.

The stress ratio has a local concentration at the pavement surface due to the localized tire contact stresses (non-uniform vertical and tangential stresses) under each tire rib. The stress states at tire edges or under the grooves between adjacent ribs where the confinement is lower are more critical than the stress states under tire ribs. In this case, the stress state at the bottom of the asphalt layer is more critical. The critical stress state at the bottom of the asphalt layer is caused by high tensile stresses due to bending, while the critical stress state at the pavement near-surface is mainly caused by high shear stresses at low confinements. However, the surface-initiated cracking potential may increase after considering the effect of thermal stress, construction defects (segregation or joints between pavers), or binder brittleness due to aging.

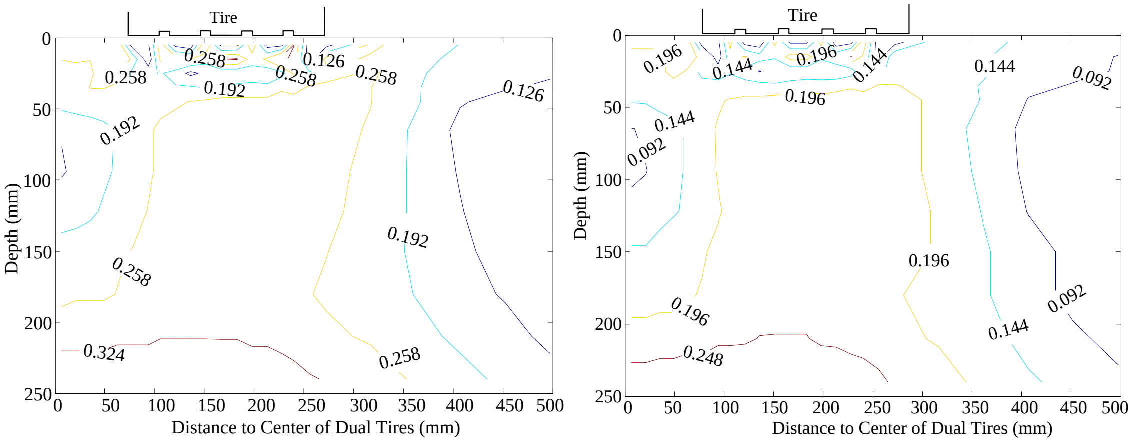

(a) (b)

Figure 6.14 Calculated shear stress ratios using (a) Mohr-Coulomb; and (b) Drucker-Prager Failure Criteria at 25ºC

Figures 6.15(a) and (b) show the calculated stress ratios within the asphalt layer under the loading of a dual-tire assembly at 45ºC (35.5kN, 724kPa, and 8km/h), respectively, using the Mohr–Coulomb and Drucker–Prager criteria. Similar to the case at 25ºC, the stress ratio contours have similar trends when using the two failure criteria. The results show that at the pavement surface, relatively high failure potential occurs in the area between dual tires, similar to the case at the intermediate temperature. However, at the high temperature, the most critical stress state is located at the shallow depth of the asphalt layer (around 50mm). This is probably because the shear effect within the asphalt layer is more significant when the asphalt becomes soft. This indicates that "what appeared to be surface cracking" could initiate at some distance below pavement surface in conjunction with the distortional deformation.

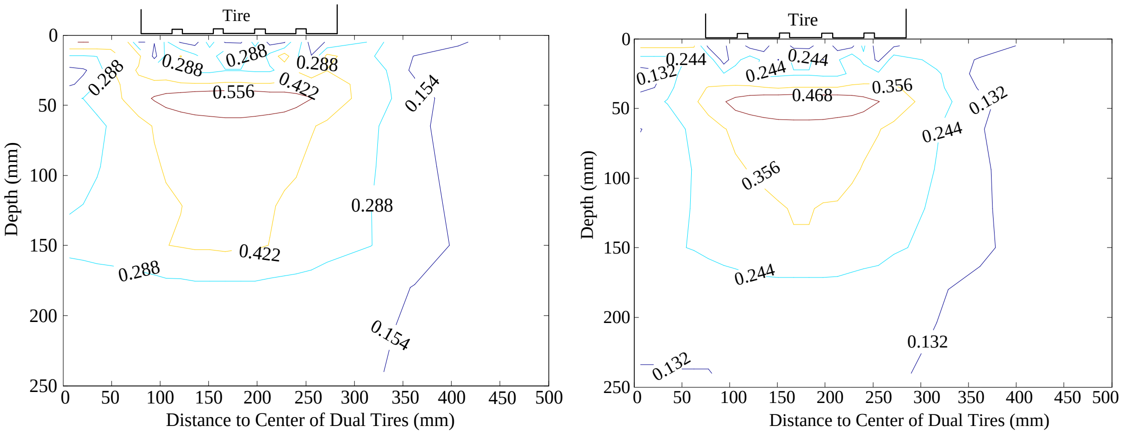

(a) (b)

Figure 6.15 Calculated shear stress ratios using (a) Mohr-Coulomb; and (b) Drucker-Prager Failure Criteria at 45ºC

Cracks develop in pavement structure could be tensile-induced (Mode I) or shear-induced (Mode II) cracking. Under tensile stresses, a crack may initiate and open in bending or pure tension, such as the bottom-up fatigue cracking or the low temperature cracking. However, shear-induced cracking usually develops at a location with relatively high shear stresses and low confinements, such as at the pavement near-surface. Due to the high cohesion, asphalt concrete may prevent shearing by dilation and developing secondary tension that could result in micro-cracks. However, visible cracks are more likely to develop in the absence of higher confinement that keeps the micro-cracks closed (Song and Pellinen 2007).

The shear-induced cracking phenomenon is supported by laboratory findings reported in the literature. Wang et al. (2003) observed that cracks initiated in the rutting zone (25-50mm below surface) as the shear deformation developed in the cyclic wheel test at the high temperature (Figure 6.16). From an energy dissipation point of view, the energy dissipation of damaged material could occur in the form of new fracture surfaces, or plastic deformation, or both. Therefore, the importance of shear effect in the formation and growth of near-surface cracking should not be neglected, and an asphalt mixture that is sensitive to rutting at high temperatures may also be sensitive to shear-induced cracking.

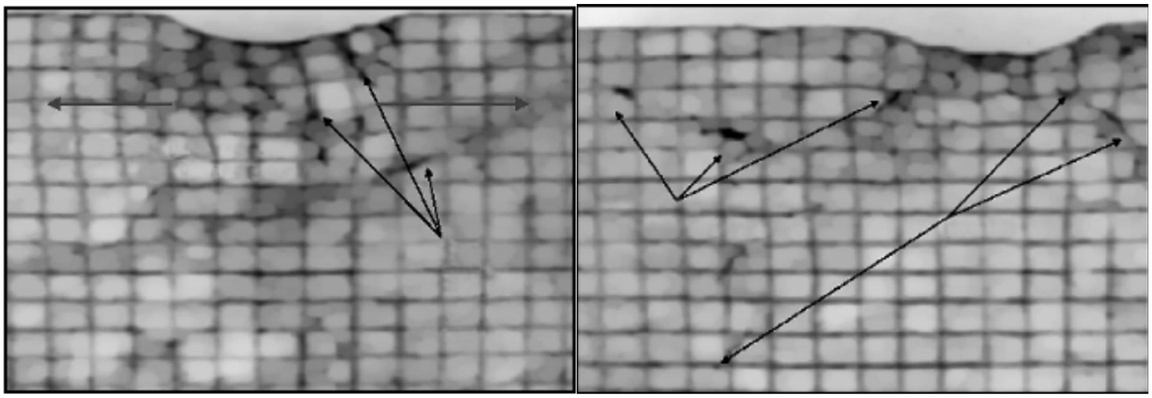

(a) (b)

Figure 6.16 Development of near-surface cracking (a) under the wheel; and (b) away from the wheel after cyclic wheel test (after Wang et al. 2003)

6.3 Effect of Contact Stress Distributions on Near-Surface Failure Potential

The contact stress distributions at the tire-pavement interface vary under various tire loading conditions (load, tire pressure, tire type, and vehicle maneuvering) and thus affect the stress states at the pavement near-surface. In the sensitivity analysis, the shear stress ratios at various scenarios are calculated using the Drucker-Prager failure criterion.

Figures 6.17(a) and (b) show the calculated stress ratios within the asphalt layer under the uniform contact stress distribution, respectively, at 25ºC and 45ºC. Compared to Figures 6.14(b) and 6.15(b), it is clear that the uniform contact stress distribution underestimates the failure potential at both temperatures. Especially, the shear failure potential at the shallow depth of the asphalt layer at the high temperature can be significantly underestimated if neglecting the non-uniform distribution of vertical contact stresses and surface tangential stresses.

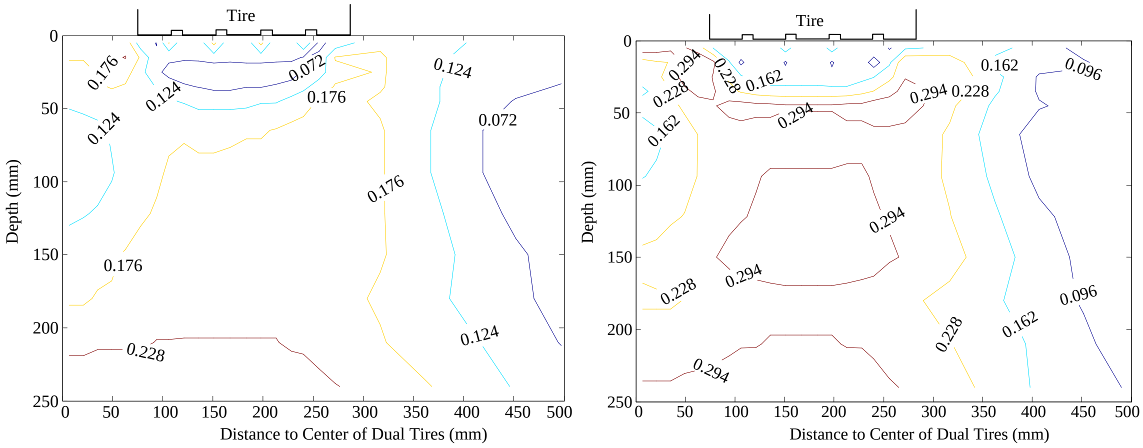

(a) (b)

Figure 6.17 Calculated stress ratios under the uniform contact stress distribution at (a) 25ºC; and (b) 45ºC

Figures 6.18(a) and (b) show the calculated stress ratios within the asphalt layer under the loading of a wide-base 455 tire at 25ºC and 45ºC, respectively. Compared to Figures 6.14(b) and 6.15(b), it is clear that the wide-base tire increases the failure potential at the bottom of the asphalt layer at the intermediate temperature, but reduces the failure potential at the pavement near-surface at both temperatures.

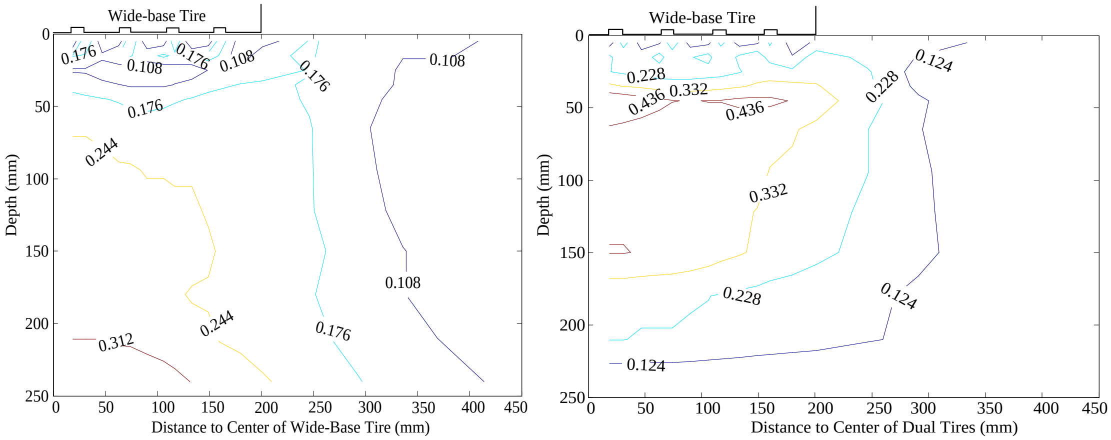

(a) (b)

Figure 6.18 Calculated shear stress ratios under the loading of a wide-base 455 tire at (a) 25ºC; and (b) 45ºC

Figures 6.19 and 6.20 show the calculated stress ratios within the asphalt layer under heavy load (53.6kN) and high tire inflation pressure (966kPa), respectively, at 25ºC and 45ºC. At the intermediate temperature, the surface failure potential at the inner tire edge becomes more critical as the load increases, while the increase of surface failure potential is relatively not significant as the tire pressure increases (compared to Figures 6.14(b)). At the high temperature, the heavy load mainly increases the area of stress concentration with a slightly increased peak stress ratio; while the high tire pressure significantly increases the peak stress ratio in a small area of stress concentration (compared to Figure 6.15(b)). Again, these observations are related to the variations of the localized contact stress distributions as the load or tire pressure increases.

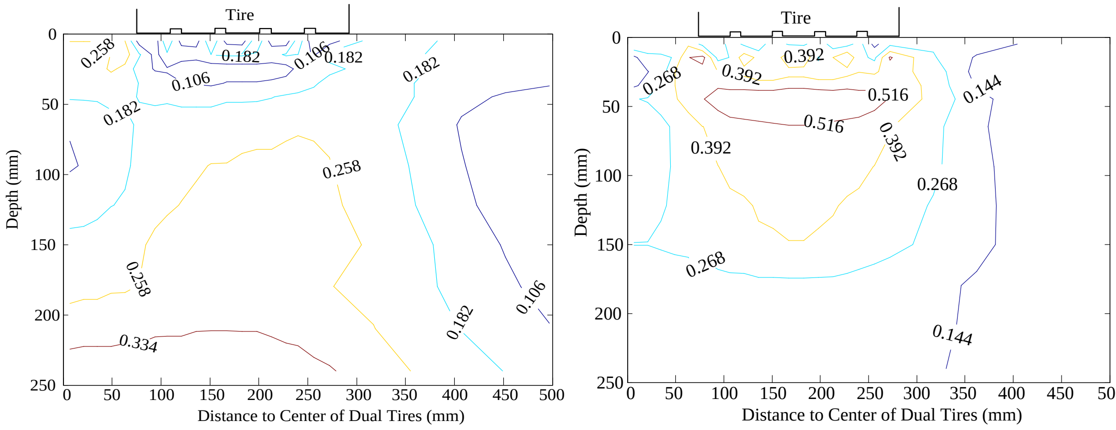

(a)

(b)

Figure 6.19 Calculated shear stress ratios under heavy load at (a) 25ºC; and (b) 45ºC

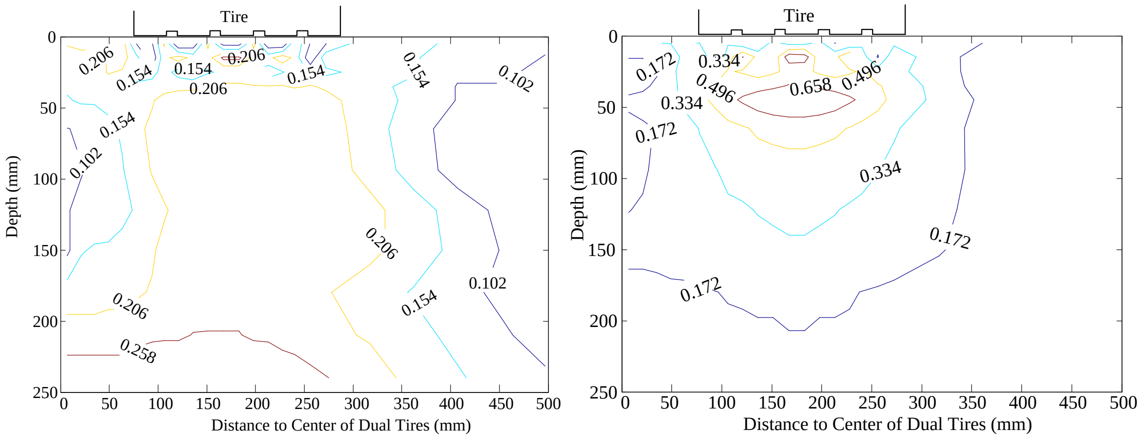

(a)

(b)

Figure 6.20 Calculated shear stress ratios at high tire pressure at (a) 25ºC; and (b) 45ºC

Figures 6.21 and 6.22 show the calculated stress ratios within the asphalt layer under vehicle maneuvering at 25ºC and 45ºC, respectively. The tire-pavement contact stresses were obtained from the tire-pavement interaction model using a surface friction coefficient of 0.8 at tire braking and slip angle of 5º at tire cornering. Compared to Figures 6.14(b) and 6.15(b), the results show that tire braking or cornering causes the greater failure potential, especially at the high temperature. It is noted that as the tire is cornering, the critical stress states are concentrated towards one side of the tire because tire cornering causes high vertical and transverse contact stresses shifted to one side of the tire contact area.

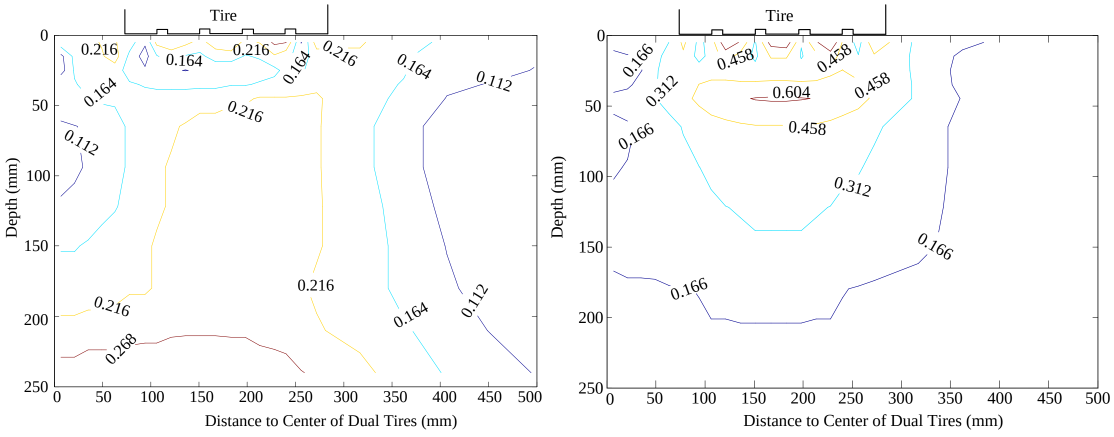

(a) (b)

Figure 6.21 Calculated shear stress ratios due to tire braking at (a) 25ºC; and (b) 45ºC

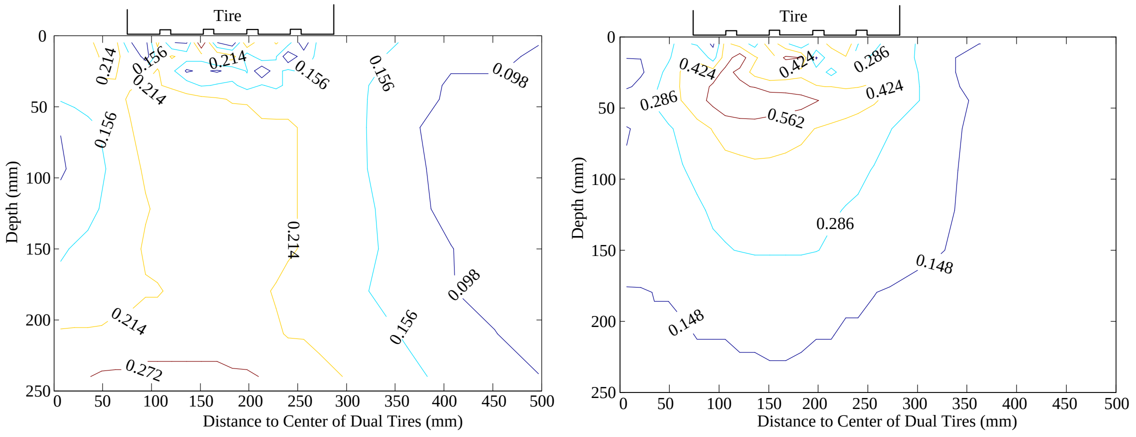

(a) (b)

Figure 6.22 Calculated shear stress ratios due to tire cornering at (a) 25ºC; and (b) 45ºC

Table 6.4 summarizes the shear stress ratios at the pavement near-surface at critical loading conditions with respect to the normal loading condition (35.5kN, 724kPa, and 8km/h). The results clearly show that high tire pressure is detrimental to the shear failure at the shallow depth of the asphalt layer at high temperatures, while overload can significantly increase the surface failure potential at intermediate temperatures.

Table 6.4 Stress Ratios Caused by Critical Loading Conditions

Case	Load (kN)	Pressure (kPa)	Vehicle Maneuvering	Stress ratio at surface at 25°C	Stress ratio at shallow depth at 45°C
1	35.5	724	No	0.196	0.468
2	35.5	966	No	0.206	0.658
3	53.6	724	No	0.258	0.516
4	35.5	724	Braking	0.216	0.604
5	35.5	724	Cornering	0.214	0.562

6.4 Effect of Structure Characteristics on Near-Surface Failure Potential

Since the failure potential at the pavement near-surface is related to other factors in addition to loading, the effects of pavement structure characteristics on the stress states at the pavement near-surface were investigated, such as the asphalt layer stiffness gradient, interface bonding condition, and underlying support.

For thick asphalt pavements, the stiffness gradient in the asphalt layer could be caused by variations in the characteristics of each course, aging of surface layer, and temperature gradients. Changes in temperature during the day and night would produce high stiffness variations in the asphalt layer. In this study, a temperature profile is assumed by introducing a rate of linear temperature differential of 1.1ºC/cm within the asphalt layer based on a previous study (Myers et al. 1998). For the purpose of comparison with the case of the uniform temperature of 25ºC, the average temperature is kept at 25ºC at the middle of the asphalt layer for both negative and positive temperature gradients (Figure 6.23). The stiffness variation due to the negative temperature gradient is similar to the case that the stiffness of the asphalt layer decreases as the depth increases.

Figures 6.24(a) and (b) show the calculated stress ratios within the asphalt layer under the loading of a dual-tire assembly for the negative and positive temperature gradients, respectively. It was found that the critical stress states are located at 75-150mm below the pavement surface when the asphalt layer has the negative temperature gradient. For the negative temperature gradient, the calculated critical stress ratios are greater than those obtained from the uniform temperature case, as shown in Figure 6.14(b). On the other hand, the critical stress states are located at the bottom of the asphalt layer when the asphalt layer has the positive temperature gradient.

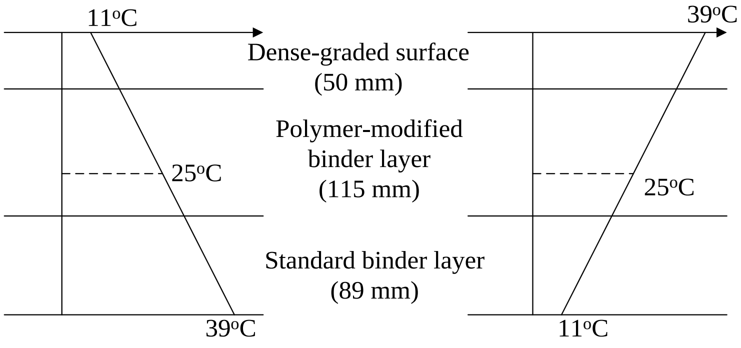

(a) (b)

Figure 6.23 Illustration of (a) negative and (b) positive temperature gradients in the asphalt layer

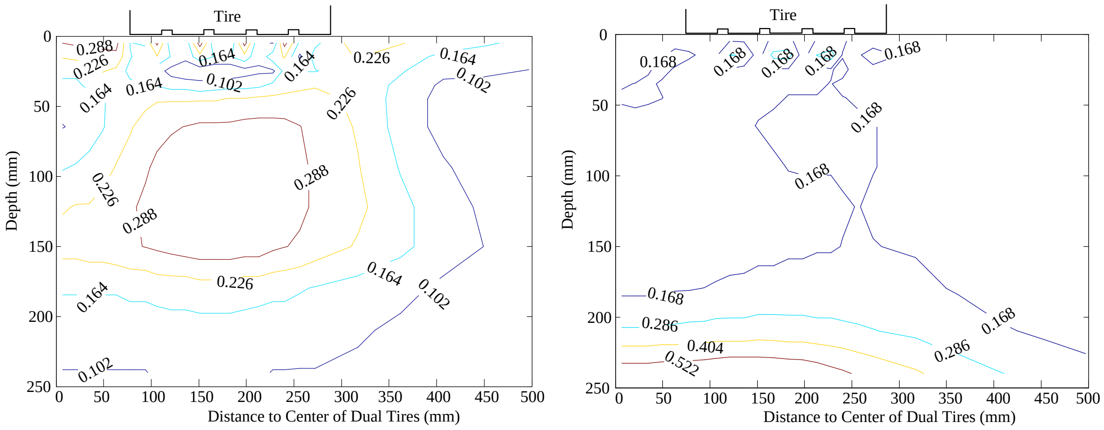

(a) (b)

Figure 6.24 Calculated shear stress ratios for the (a) negative; and (b) positive temperature gradients

The general assumption in the design of thick asphalt pavements is that the asphalt layers are fully bonded together without relative slip. Debonding describes a condition where adjacent asphalt layers lose adhesion to one another. In the analysis, the debonding between asphalt layers is modeled as two separate layers with frictional interface, and the coefficient of friction is assumed equal to one.

The calculated stress ratios within the asphalt layers under the loading of a dual-tire assembly at 25ºC were plotted in Figures 6.25(a) and (b), respectively, for the first and second interface debonding. The first interface is between the dense-graded surface layer (50mm) and the polymer-modified binder layer (115mm), while the second interface is between the polymer-modified binder layer and the standard binder layer (89mm). Compared to Figure 6.14(b), the debonding significantly increases the critical stress ratio around the debonded interface, especially for the debonded first interface. This indicates that debonding under the wearing surface could cause near-surface cracking to initiate at the bottom of the surface layer and propagate upward. This is in agreement with the field observation reported by Willis and Timm (2007) (Figure 6.26). Hence, the achievement of adequate bonding between asphalt layers during construction should be emphasized for thick asphalt pavements.

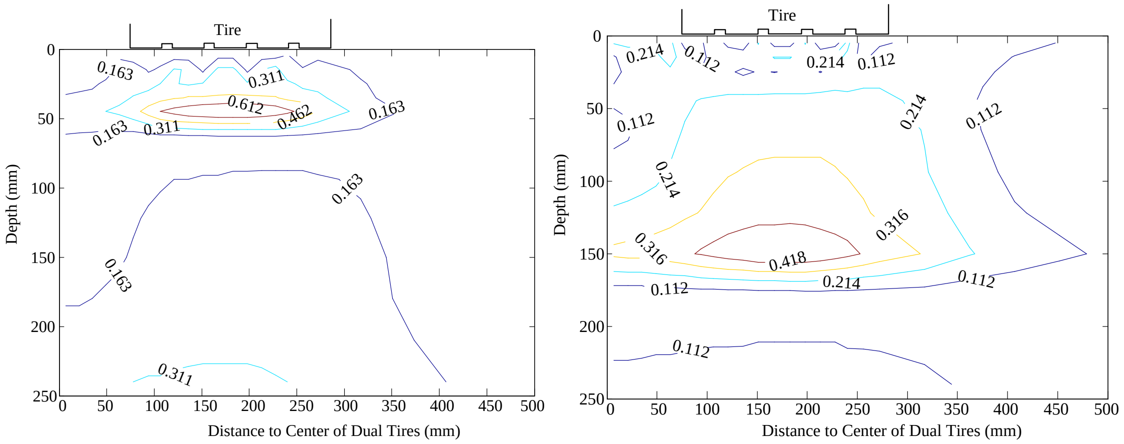

(a) (b)

Figure 6.25 Calculated shear stress ratios with debonding at the (a) first; and (b) second interface

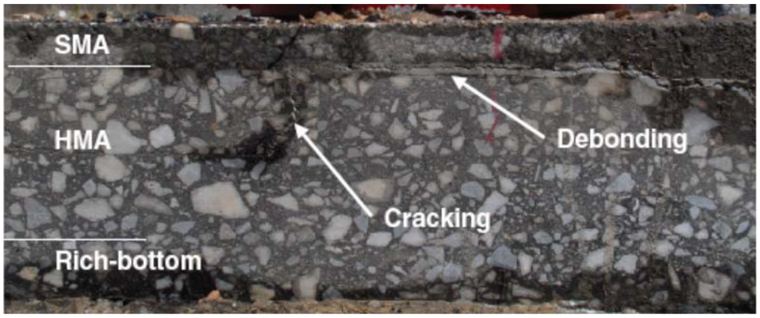

Figure 6.26 Development of near-surface cracking due to debonding (after Wills and Timm 2003)

Figures 6.27(a) and (b) show the calculated stress ratios within the asphalt layer under the loading of a dual-tire assembly at 25ºC with a weak (150MPa) and strong (700MPa) subgrade support, respectively. The results show that the failure potential in the asphalt layer decreases as the subgrade support becomes stronger, especially for the failure potential at the bottom of the asphalt layer. It is noted that as the subgrade support becomes stronger, the critical failure location could shift to the upper asphalt layer close to the pavement surface. This indicates that the failure potential at the pavement near-surface could increase as the underlying layer is very stiff.

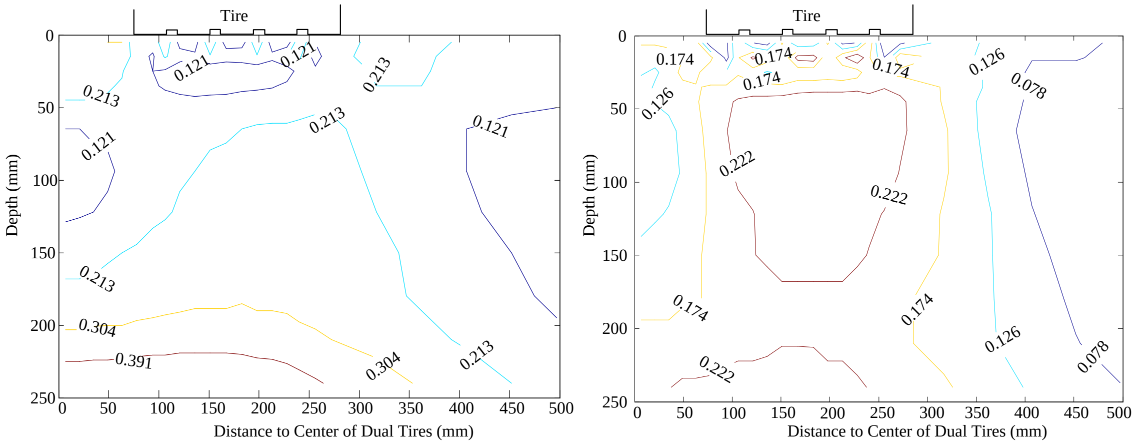

(a) (b)

Figure 6.27 Calculated shear stress ratios with a (a) weak and (b) strong subgrade support

6.5 Summary

In this chapter, strain responses responsible for near-surface failure in thick asphalt pavements were investigated at various loading scenarios. The analysis results indicate that surface-initiated cracking cannot be induced by tension only and the effect of shear is important and can not be neglected. In order to evaluate the failure potential at multi-axial stress states, a shear stress ratio concept based on the Drucker-Prager failure criterion was proposed.

It was found that cracks may initiate at the pavement surface at intermediate temperatures. However, at high temperatures, shear-induced cracking becomes more critical and may initiate at the shallow depth below the pavement surface in conjunction with distortional deformation. The failure potential at the pavement near-surface is affected by tire-pavement contact stress distributions, which is dependent on load, tire inflation pressure, tire configuration, and vehicle maneuvering. In addition, the analysis results show that the critical failure location in the thick asphalt layer vary as the pavement structure characteristics (stiffness gradient, interface bonding, or underlying support) change.

CHAPTER 7 FINDINGS, CONCLUSIONS, AND RECOMMENDATIONS

In this dissertation, the mechanism of tire-pavement interaction and the effect of tire-pavement interaction on pavement responses were analyzed through a decoupled modeling approach. First, an air-inflated 3-D tire model was built and the interaction between a tire and a non-deformable pavement surface was simulated. The tire is modeled as a composite structure including rubber and reinforcement. The steady-state tire rolling process was simulated using an Arbitrary Lagrangian Eulerian (ALE) formulation. The developed tire-pavement interaction model is used to evaluate the mechanism of load distribution at the tire-pavement interface under various tire loading and rolling conditions. Second, a 3-D FE model of flexible pavement was developed to analyze pavement responses under various loading scenarios. This model utilizes implicit dynamic analysis and simulates vehicular loading as a continuous moving load with three-dimensional contact stresses at the tire-pavement interface. In the pavement model, the asphalt layer is modeled as a linear viscoelastic material and the granular base layer is modeled as a nonlinear anisotropic material. The FE model is used to analyze critical pavement responses in thin and thick asphalt pavements considering different damage mechanisms.

7.1 Findings

The following findings were obtained from the analyses:

Tire-Pavement Interaction

1) Both the prediction and measurements show that the vertical contact stresses and localized tangential contact stresses are non-uniformly distributed at the tire-pavement interface. At the static loading condition, both the vertical and transverse contact stresses have a convex shape along the contact length; while the longitudinal contact stresses have a reversed distribution pattern. It is noted that the transverse contact stress increases in magnitude with the lateral distance from the center of each rib and reaches its maximum at the edge of each rib.
2) The load and tire inflation pressure affect the tire-pavement contact stress distributions in different ways. As the load increases, the vertical contact stresses

at tire edges and the longitudinal contact stresses increase. On the other hand, as the tire inflation pressure increases, the vertical contact stresses at tire center and the transverse contact stresses increase. Therefore, at heavy load, the maximum vertical contact stress may be located at tire edges; while at high tire inflation pressure, the non-uniformity of vertical contact stress is the highest. The stress ratio of the maximum contact stresses in three directions ranges from 1:0.23:0.07 to 1:0.31:0.30 as the load varies between 18 and 40kN and the tire inflation pressure varies between 414 and 966kPa.

3) Vehicle maneuvering behavior significantly affects the magnitudes and distributions of tire-pavement contact stresses. Compared to the free rolling condition, tire braking/acceleration causes reduction in transverse contact stresses; but significant increase in longitudinal contact stresses. The longitudinal contact stresses at tire braking increase with the slip ratio until the tire reaches full braking. As the tire is cornering, both the vertical and transverse contact stresses are greater than those at the free rolling condition. The peak contact stresses at tire cornering shift toward one side of the contact patch and increase as the slip angle increases.
4) As the friction at the tire-pavement surface increases, the tangential tire-pavement contact stresses at various rolling conditions and the vertical contact stresses at tire cornering increase. It is reasonable to use the constant static friction coefficient when predicting the tire-pavement contact stresses at the free rolling condition or at the cornering condition with small slip angles. However, using the constant friction model may overestimate the peak longitudinal contact stress when the tire is sliding at the full braking condition.

Critical Pavement Responses and Failure Mechanism

1) Accurate pavement responses can only be predicted when the viscoelastic nature of the asphalt layer and the nonlinear anisotropic behavior of the granular base layer are integrated into the mechanistic model. The modulus distribution in the base layer is not only affected by the wheel load, but also affected by the

temperature and vehicle speed due to the viscoelastic nature of the asphalt surface layer.

2) It was found that neglecting the cross-anisotropic stress-dependent behavior of the granular base layer could significantly underestimate fatigue cracking and rutting potential in thin asphalt pavements; especially at high temperatures. However, the stress-softening behavior of subgrade mainly affects the responses in the base layer and subgrade.
3) The multi-axial stress state needs to be considered when evaluating near-surface failure potential in thick asphalt pavements. The analysis results indicate that surface-initiated cracking cannot be induced by tension only and the effect of shear cannot be neglected. The calculated shear stress ratio based on the Drucker-Prager failure criterion provides a reasonable indication for the failure at the pavement near-surface at intermediate and high temperatures.
4) It was found that cracks may initiate at the pavement surface at intermediate temperatures. At high temperatures, shear-induced cracking becomes more critical and it may initiate at the shallow depth below the pavement surface in conjunction with the distortional deformation. The critical failure location in thick asphalt pavements is also affected by pavement structure characteristics, such as the stiffness gradient, interface debonding, or underlying support.

Effect of Tire-Pavement Interaction on Pavement Responses

1) Flexible pavement responses are sensitive to the loading input represented by the tire-pavement contact stress distributions, especially when the asphalt layer is soft. The analysis results show that compared to the uniform contact stress assumption, the 3-D tire contact stresses cause greater fatigue cracking and primary rutting potential but less failure potential in the base layer and subgrade in thin asphalt pavements. In addition, assuming uniform contact stress distribution at the tire-pavement interface underestimates near-surface failure potential in thick asphalt pavements.
2) For thin asphalt pavements, the heavy load mainly causes the increase of responses in the subgrade, while the effect of tire inflation pressure is more

significant for the responses in the asphalt layer. In addition, the load effect is more significant at intermediate temperatures; while the inflated tire pressure effect is more significant at high temperatures. This indicates that the high shear-resistant mixture is desired when the truck tire pressure is high in regions with warm climates, while the axle weight limit should be enforced during spring seasons on low-volume roads in order to minimize pavement damage.

3) The effects of load or inflated tire pressure on near-surface failure potential in thick asphalt pavements are dependent on the variations of localized tire contact stress distributions. At intermediate temperatures, surface failure potential at the inner tire edges becomes more critical as the load increases, while the effect of tire pressure is relatively not significant. However, at high temperatures, high tire pressure significantly increases shear failure potential at the shallow depth of the asphalt layer.
4) Tire braking and cornering induce high tangential contact stresses at the pavement surface, which increase near-surface failure potential in thick asphalt pavements. For thin asphalt pavements, tire cornering mainly increase rutting potential, while tire braking mainly increase shoving/corrugation potential in the asphalt layer. This indicates that the effect of vehicle maneuvering behavior should be considered for pavement design at specific sites, such as intersections, pavement sections with great slopes, or curved road sections.
5) The impact of wide-base tire on pavement damage depends on the predominant failure mechanisms of the roadway. Compared to the conventional dual-tire assembly, the new generation of wide-base tire results in similar or less primary rutting potential in thin asphalt pavements and near-surface failure potential in thick asphalt pavements, although it increases the damage potential at deeper pavement depths, which is less pronounced in causing failure.

7.2 Conclusions

This study concludes that knowledge of tire-pavement contact stress distributions is critical for pavement response prediction. Most importantly, the non-uniform distribution of vertical contact stresses and the localized tangential contact stresses should be considered in the mechanistic-empirical pavement design. The contact stress distributions at the tire-pavement interface are affected by vehicle loading (wheel load and tire inflation pressure), tire configuration (dual-tire assembly and wide-base tire), vehicle maneuvering (braking/acceleration and cornering), and pavement surface friction. Therefore, pavement damage should be quantified using accurate loading inputs that are represented by realistic tire-pavement contact stress distributions.

Thin and thick asphalt pavements fail in different ways. Multiple distress modes could happen in thin asphalt pavements, including bottom-up fatigue cracking and rutting in each pavement layer. It was found that the interaction between the viscoelastic asphalt layer and the nonlinear anisotropic granular base material plays an important role for the stress distribution within a thin asphalt pavement structure under vehicular loading. In thick asphalt pavements, near-surface cracking is a critical failure mechanism, which is affected by the localized stress states and pavement structure characteristics. Particularly, the effect of shear stress on the formation of near-surface cracking at multi-axial stress states is important and can not be neglected, especially at high temperatures.

7.3 Recommendations for Future Study

Despite utilizing the advanced finite element model for the analysis of tire-pavement interaction and pavement responses in this study, in order to better design long-lasting pavements, the following tasks are recommended in future studies:

1) This study considers pavement surface as a rigid flat surface for the prediction of tire-pavement contact stresses. Deformable road surfaces should be considered in future studies to simulate the coupled tire-pavement interaction behavior. The irregularities (texture) of pavement surfaces should also be considered. This would be especially important when detailed tire-pavement interaction conditions are studied; including rolling resistance, tire wear, and noise. This will allow considering pavement durability, safety, and quietness.
2) Only one specific tire with one type of tread pattern was simulated in this study. It is expected that the 3-D tire contact stress distributions depend on the tire geometry, structure, and tread configuration. It is recommended that various tire types including wide-base tires with different tread patterns should be modeled in

future studies and a large database of contact stresses should be created. This database can be used not only for design of new pavements and overlays, but also for setting reasonable axle load or pressure regulations for trucking operation. On the other hand, this database would be beneficial for tire manufacturers to design "pavement-friendly" tires.

3) Although the finite element method can consider many important aspects in pavement modeling, it requires significant computation time and resource. For pavement design purpose, a convenient and reliable method is desired to consider the effects of tire-pavement interaction on pavement responses and damage prediction. Therefore, a large database of pavement responses should be built considering various loading conditions, environmental conditions, and pavement structure characteristics. This database can be used to develop design monographs or Artificial Neuro Network (ANN) for pavement design purpose.
4) Many studies have been conducted to characterize the fatigue behavior of asphalt mixtures under the pure tension or bending stress states. The analysis results presented in this dissertation clearly show that the shear effect can not be neglected in the formation of near-surface cracking. Therefore, a laboratory testing method that better simulates the material failure at multi-axial stress states need to be developed and verified. Furthermore, a performance prediction model should be developed for considering near-surface cracking mechanism in the mechanistic-empirical pavement design. This model could be based on continuum damage theory or fracture mechanics method and the effect of binder aging and healing should be considered.

REFERENCES

AASHTO (1999) *Standard Method of Test for Determining the Resilient Modulus of Soils and Aggregate Materials*, AASHTO T307, Washington, D.C.

AASHTO (2003) *Standard Method of Test for Determining the Creep Compliance and Strength of Hot-Mix Asphalt (HMA) Using the Indirect Tensile Test Device*, AASHTO T322, Washington, D.C.

ABAQUS (2007) *ABAQUS Analysis User's Manual*, Version 6.7, Habbit, Karlsson & Sorenson, Inc, Pawtucket, RI.

Adu-Osei, A., Little, D.N. and Lytton, R.L. (2001) "Cross-anisotropic Characterization of Unbound Granular Materials," *Transportation Research Record*, No.1757, TRB, Washington, D.C., pp. 82-91.

Al-Qadi, I.L., Loulizi, A., Janajreh, I., and Freeman, T.E. (2002) "Pavement Response to Dual Tires and New Wide-Base Tires at Same Tire Pressure," *Transportation Research Record,* No. 1806, TRB, Washington, D.C., pp. 38-47.

Al-Qadi, I.L., Elseifi, M.A. and Yoo, P.J. (2005) "Characterization of Pavement Damage Due to Different Tire Configurations," *Journal of the Association of Asphalt Paving Technologists*, Vol. 84, AAPT, pp. 921-962.

Al-Qadi, I.L., and Elseifi, M.A. (2007) "State-of-the-Practice of the New Generation of Wide-Base Tire and Its Impact on Trucking Operations," *Transportation Research Record,* No. 2008, TRB, Washington, D.C., pp. 100-109.

Al-Qadi, I.L., Tutumluer, E., Dessouky, S.H., Kwon, J. (2007) *Effectiveness of Geogrid-Reinforcement in Flexible Pavements: A Full-Scale Testing*, Final Report to Tensar Earth Technologies, Inc., University of Illinois, Urbana-Champaign, IL.

Al-Qadi, I.L. and Yoo, P.J. (2007) "Effect of Surface Tangential Contact Stress on Flexible Pavement Response," *Journal of the Association of Asphalt Pavement Technologist*, Vol. 76, AAPT, pp. 663-692.

Al-Qadi, I.L., Wang, H., Yoo, P.J., and Dessouky, S.H. (2008) “Dynamic Analysis and In-Situ Validation of Perpetual Pavement Response to Vehicular Loading,” *Transportation Research Record*, No. 2087, TRB, Washington, D.C., pp. 29-39.

Al-Qadi, I.L., and Wang, H. (2009) “Full-depth Pavement Responses under Various Tire Configurations: Accelerated Pavement Testing and Finite Element Modeling,” *Journal of the Association of Asphalt Paving Technologists*, Vol. 78, AAPT, pp. 645-680.

Ameri-Gaznon, M., and Little, D.N. (1990) “Octahedral Shear Stress Analyses of an ACP Overlay on a Rigid Base,” *Journal of the Association of Asphalt Paving Technologists*, Vol. 59, AAPT, pp. 443-476.

ARA, Inc., ERES Division, (2004) *Guide for Mechanistic-Empirical Design of New and Rehabilitated Pavement Structures*, NCHRP 1-37A Final Report, TRB, Washington, D.C.

Asphalt Institute, (1982) *Research and Development of the Asphalt Institute’s Thickness Design Manual (MS-1)*, Research Report 82-1, 9th ed., College Park, MD.

Baladi, G.Y., Michael, S., and Svasdisant, T. (2002) *Determining the Causes of Top-down Cracking in Bituminous Pavements*, Final Report, Michigan State University, East Lansing, MI.

Bathe, K.J. (1982) *Finite Element Procedures in Engineering Analysis*, Prentice-Hall, NJ.

Bensalem, A., Broen, A.J., Nunn, M.E., Merrill, D.B., and Lloyd, W.G. (2002) “Finite Element Modeling of Fully Flexible Pavements: Surface Cracking and Wheel Interaction,” *Proceedings of the 2nd International Symposium on 3D Finite Element for Pavement Analysis, Design, and Research*, Charleston, WV, pp. 103-121.

Buttlar, W. and Roque, R. (1994) “Development and Evaluation of the Strategic Highway Research Program Measurement and Analysis System for Indirect Tensile Testing at Low Temperatures,” *Transportation Research Record*, No. 1454, TRB, Washington, D.C., pp. 163-171.

Carpenter S.H. (2008) *Extended Life Hot-Mix Asphalt Pavement (ELHMAP) Test Sections at ATREL*, Research Report FHWA-ICT-08-017, Illinois Center for Transportation, University of Illinois, Urbana-Champaign, IL.

Carpenter, S.H., Ghuzlan, K.A., and Shen, S. (2003) "Fatigue Endurance Limit for Highway and Airport Pavements," *Transportation Research Record*, No. 1832, TRB, Washington, D.C., pp. 29-39.

Center for Research and Contract Standardization in Civil and Traffic Engineering (CROW) (1990) *Surface Cracking in Asphalt Layer*, Report of the Working Group, CROW, Netherlands.

Chabot, A., Tamagny, P., Duhamel, D., and Poché, D. (2006) "Visco-elastic Modeling for Asphalt Pavements – Software ViscoRoute," *Proceedings of the 10th International Conference on Asphalt Pavements*, Québec, Canada, Vol. 2, pp. 5-14.

Chopra, A.K. (2001) *Dynamics of Structures*, 2nd ed., Prentice Hall, Upper Saddle River, NJ.

Chou, Y.T., and Larew, H.G. (1969) "Stresses and Displacements in Viscoelastic Pavement Systems under a Moving Load," *Highway Research Record*, No. 282, HRB, Washington, D.C., pp. 24-40.

COST 334 (2001) *Effects of Wide Single Tires and Dual Tires*, European Cooperation in the Field of Scientific and Technical Research, Brussels, Belgium.

Daniel, J.S. and Kim, Y.R. (2002) "Development of a Simplified Fatigue Test and Analysis Procedure Using a Viscoelastic Continuum Damage Model," *Journal of the Association of Asphalt Paving Technologists*, Vol. 71, AAPT, pp. 619-650.

Darestani, M.Y., David, P.T., Andreas, N., and Daksh, B. (2006) "Dynamic Response of Concrete Pavements under Vehicular Loads," *Proceedings of IABSE Symposium - Response to Tomorrow's Challenges in Structural Engineering*, Budapest, Hungary, pp. 104-105.

Deacon, J.A., Harvey, J.T., Guada, I., Popescu, L., and Monismith, C.L. (2002) "Analytically Based Approach to Rutting Prediction," *Transportation Research Record*, No. 1806, TRB, Washington, D.C., pp. 9-18.

De Beer, M., Fisher, C., and Jooste, F.J. (1997) "Determination of Pneumatic Tire pavement Interface Contact Stresses Under Moving Loads and Some Effects on Pavements with Thin Asphalt Surfacing Layers," *Proceedings of 8th International Conference on Asphalt Pavements (Volume I)*, Seattle, WA, pp 179-227.

De Beer, M., Fisher, C., and Jooste, F.J. (2002) "Evaluation of Non-uniform Tire Contact Stresses on Thin Asphalt Pavements," *Proceedings of 9th International Conference on Asphalt Pavements (ICAP 2002)*, Copenhagen, Denmark.

Douglas, R.A., Woodward, W.D.H., and Woodside, A.R. (2000) "Road Contact Stresses and Forces under Tires with Low Inflation Pressure," *Canadian Journal of Civil Engineering*, Vol. 27, pp. 1248-1258.

Doweling, N.E. (1999) *Mechanical Behavior of Materials*, 2nd ed., Prentice Hall, Upper Saddle River, NJ.

Duncan, J.M., Monismith, C.L., and Wilson, E.L. (1968) "Finite Element Analyses of Pavements," *Highway Research Record*, No. 228, TRB, Washington, D.C., pp. 18-33.

Elseifi, M. A., Al-Qadi, I.L., and Yoo, P.J. (2006) "Viscoelastic Modeling and Field Validation of Flexible Pavements," *Journal of Engineering Mechanics*, Vol. 132, No. 2, ASCE, pp. 172-178.

Elliott, J.F., and Moavenzadeh, F. (1971) "Analysis of Stresses and Displacements in Three layer Viscoelastic Systems," *Highway Research Record*, No. 345, HRB, Washington, D.C., 45-57.

Faria, L.O., Oden, J.T., Yavari, B., Tworzydlo, W.W., Bass, J.M., and Becker, E.B. (1992) "Tire Modeling by Finite Element," *Tire Science and Technology*, TSTCA, Vol. 20, No.1, pp. 33-56.

Ferry, J.D. (1980) *Viscoelastic Properties of Polymers*, 3rd ed., John Wiley & Sons, Hoboken, NJ.

Ford, T.L. and Yap, P. (1990) "Truck Tire/Pavement Interface," *The Promise of New Technology in the Automotive Industry*: XXIII FISITA Congress, Torino, Italy, pp.333-340.

Freeman, T.J. and Carpenter, S.H. (1986) "Characterizing Permanent Deformation in Asphalt Concrete Placed over Portland Cement Concrete Pavements," *Transportation Research Record,* No.1070, TRB, Washington, D.C., pp. 342-387.

Ghoreishy, M.H.R., Malekzadeh, M., and Rahimi, H. (2007) "A Parametric Study on the Steady State Rolling Behavior of a Steel-Belted Radial Tire," *Iranian Polymer Journal,* No.16, pp. 539-548.

Greene, J., Toros, U., Kim, S., Byron, T., and Choubane, B. (2010) "Impact of Wide-Base Tires on Pavement Damage," *Transportation Research Record,* No. 2155, TRB, Washington, D.C., pp. 82-90.

Gillespie, T.D., Karimihas, S.M., Cebon, D., Sayers, M.W., Nasim, M.A., Hansen, W., and Ehsan, N. (1993) *Effects of Heavy-Vehicle Characteristics on Pavement Response and Performance,* NCHRP Report 353, TRB, Washington, D.C.

Gokhale, S., Anderson, D., Christensen, D. and Bonaquist, R. (2005) "Simplified Protocol for Triaxial Testing of Hot-Mix Asphalt Concrete," *Journal of the Association of Asphalt Paving Technologists*, Vol. 74E, AAPT.

Gonz´alez, J.A. and Abascal, R. (2004) "Linear Vscoelastic Boundary Element Formulation for Steady State Moving Loads," *Engineering Analysis with Boundary Elements*, 28(7), pp. 815-823.

Groenendijk, J. (1998) *Accelerated Testing and Surface Cracking of Asphaltic Concrete Pavements*, PhD dissertation, Delft University of Technology, Delft, Netherlands.

Hajj, E.Y., Siddharthan, R.V., Sebaaly, P.E., and Weitzel, D. (2007) "Hot-Mix Asphalt Mixtures for Nevada's Intersections," *Transportation Research Record,* No. 2001, TRB, Washington, D.C., pp. 73-83.

Hambleton, J.P., and Drescher, A. (2007) "Modeling Test Rolling on Cohesive Subgrades," *Proceedings of the International Conference on Advanced Characterization of Pavement and Soil Engineering Materials,* Athens, Greece, pp. 359-368.

Hambleton, J.P., and Drescher, A. (2009) "Modeling wheel-induced rutting in soils: Rolling," *Journal of Terramechanics*, No. 46, pp. 35-47.

Hardy, M.S.A., and Cebon, D. (1993) "Response of Continuous Pavements to Moving Dynamic Loads," *Journal of Engineering Mechanics*, Vol. 119, No. 9, ASCE, pp. 1762-1780.

Hicks, R.G. and Monismith, C.L. (1971) "Factors Influencing the Resilient Properties of Granular Material," *Highway Research Record*, No. 345, TRB, Washington, D.C., pp. 15-31.

Hjelmstad, K.D., and Taciroglu, E. (2000) "Analysis and Implementation of Resilient Modulus Models for Granular Solids," *Journal of Engineering Mechanics*, Vo1 26, No.8, ASCE, pp. 821-830.

Huang, Y.H. (1973) "Stresses and Strains in Viscoelastic Multilayer Systems Subjected to Moving Loads," *Highway Research Record,* No. 457, HRB, Washington, D.C., pp. 60-71.

Huang, Y.H. (1993) *Pavement Analysis and Design*, 1st ed., Prentice Hall, Upper Saddle River, NJ.

Hughes, T.J.R., Liu, W.K., and Zimmermann, T.K. (1981) "Lagrangian–Eulerian Finite Element Formulation for Incompressible Viscous Flows," *Computer Methods in Applied Mechanics and Engineering*, No. 29, pp. 329-349.

Hugo, F and Kennedy, T.W. (1985) “Surface cracking of asphalt mixtures in southern Africa,” *Proceeding of the Association of Asphalt Paving Technologists*, Vol. 54, AAPT, pp. 454-501.

Hopman, P.C. (1996) “VEROAD: A Viscoelastic Multilayer Computer Program,” *Transportation Research Record,* No. 1539, TRB, Washington, D.C., pp. 72-80.

Jooste, F.J. and Lourens, J.P. (1998) *Appropriate Models for Estimating Stresses and Strains in Asphalt Layers*, Technical Report CR-98/060, Division for Roads and Transport Technology, CSIR, Pretoria, South Africa.

Kim, M., Tutumluer, E., and Kwon, J. (2009) “Nonlinear Pavement Foundation Modeling for Three-Dimensional Finite-Element Analysis of Flexible Pavements,” *International Journal of Geomechanics,* Vol. 9, No. 5, pp. 195-208.

Kim, J., Roque, R. and Byron, T. (2009) “Viscoelastic Analysis of Flexible Pavements and Its Effects on Top-Down Cracking,” *Journal of Material in Civil Engineering*, Vol. 21, No. 7, ASCE, pp. 324-332.

Kim, I.T., and Tutumluer, E. (2005) “Unbound Aggregate Rutting Models for Stress Rotations and Effects of Moving Wheel Loads,” *Transportation Research Record,* No. 1913, TRB, Washington, D.C., pp. 41-49.

Knothe, K., Wille, R., Zastrau, B.W. (2001) “Advanced Contact Mechanics – Road and Rail,” *Vehicle System Dynamics*, Volume 35, Numbers 4-5, pp. 361-407.

Kwon, J., Tutumluer, E., and Al-Qadi, I.L. (2009) “Validated Mechanistic Model for Geogrid Base Reinforced Flexible Pavements,” *Journal of Transportation Engineering*, Vol. 135, No. 12, ASCE, pp. 915-926.

Kuai, H., Lee, H.J., Zi, G., and Mun, S. (2009) “Application of Generalized J -Integral to Crack Propagation Modeling of Asphalt Concrete Under Repeated Loading,” *Transportation Research Record*, No. 2127, TRB, Washington, D.C., pp. 72-81.

Laursen A. and Stanciulescu, I. (2006) "An Algorithm for Incorporation of Frictional Sliding Conditions within a Steady State Rolling Framework," *Communications in Numerical Methods in Engineering*, No. 22, pp. 301-318.

Lourens, J.P. (1992) *Nonlinear Dynamic Analysis and Design of Road Pavements*, RR 90/030, Department of Transport, Pretoria, South Africa.

Lytton, R.L. (1993) *Development and Validation of Performance Prediction Models and Specifications for Asphalt Binders and Paving Mixes*, SHRP-A-357 Report, TRB, Washington, D.C.

Lysmer, J. and Kuhlemeyer, R.L. (1969) "Finite Dynamic Model for Infinite Media," *Journal of Engineering Mechanics*, ASCE, Vol. 95, No. 4, pp. 859-877.

Marshek, K.M., Chen, H.H., Conell, R.B., and Hudson, R.W. (1986) "Experimental Determination of Pressure Distribution of Truck Tire-Pavement Contact," *Transportation Research Record*, No. 1070, TRB, Washington, D.C., pp. 9-14.

Mamlouk, M.S., and Davis, T.G. (1984) "Elasto-Dynamic Analysis of Pavement Deflections," *Journal of Transportation Engineering*, ASCE, Vol. 110, Issue 6, pp. 536-550.

Masad, E., Tashman, L., Little, D.N., and Zbib, H. (2005) "Viscoplastic Modeling of Asphalt Mixes with the Effects of Anisotropy, Damage, and Aggregate Characteristics," Journal of Mechanics of Materials, No. 37, pp. 1242-1256.

Masad, S., Little, D.N. and Masad, E. (2006) "Analysis of Flexible Pavement Response and Performance using Isotropic and Anisotropic Material Properties," *Journal of Transportation Engineering*, ASCE, Vol. 132, Issue 4, pp. 342-349.

Mastuno, S., and Nishizawa, T. (1992) "Mechanism of Longitudinal Surface Cracking in Asphalt Pavements," *Proceedings of the 7th International Conference on Structural Design of Asphalt Pavements*, Vol. 2, Nottingham, U.K., pp. 277-291.

Meng, L. (2002) *Truck Tire/Pavement Interaction Analysis by the Finite Element Method*, Ph.D. Dissertation, Michigan State University, East Lansing, MI.

Merrill, D. (2000) *Investigating the Causes of Surface Cracking in Flexible Pavements Using Improved Mathematical Models*, Ph.D. Dissertation, University of Wales, Swansea, U.K.

Monismith C.L., Hicks, R.G., Finn, F.N., Sousa, J., Harvey, J., Weissman, S., Deacon, J., Coplantz, J., and Paulsen, G. (1994) *Permanent Deformation Response of Asphalt Aggregate Mix,* SHRP-A-415 Report, TRB, Washington, D.C.

Monismith C.L., Popescu, L., and Harvey, J.T. (2006) "Rut Depth Estimation for Mechanistic-Empirical Pavement Design Using Simple Shear Test Results," *Journal of Association of Asphalt Paving Technologists*, AAPT, Vol. 75.

Myers, L., Roque, R., and Ruth, B. (1998) "Mechanisms of Surface-Initiated Longitudinal Wheel Path Cracks in High-type Bituminous Pavements," *Journal of Association of Asphalt Paving Technologists*, AAPT, Vol. 67, pp. 401-419.

Myers, L.A., Roque, R., Ruth, B.E., and Drakos, C. (1999) "Measurement of Contact Stresses for Different Truck Tire Types to Evaluate Their Influence on Near-Surface Cracking and Rutting," *Transportation Research Record*, No. 1655, TRB, Washington, D.C., pp. 175-184.

Nackenhorst, U. (2004) "The ALE-Formulation of Bodies in Rolling Contact - Theoretical Foundations and Finite Element Approach," *Computation Methods in Applied Mechanics and Engineering*, Vol. 193, pp. 4299-4322.

Newcomb, D.E., Buncher, M., and Huddleston, I.J. (2001) "Concepts of Perpetual Pavement," *Transportation Research Circular*, No. 503, *Perpetual Bituminous Pavements*, TRB, Washington, D.C., pp. 4-11.

Oh, J-H, Lytton, R.L., and Fernando, E.G. (2006) "Modeling of Pavement Response Using Nonlinear Cross-Anisotropy Approach," *Journal of Transportation Engineering*, ASCE, Vol. 132, No. 6, pp. 458-468.

Organization for Economic Co-Operation and Development (OECD) (1992) *Dynamic Loading of Pavements*, OECD report, OECD, Paris, France.

Pan, G. and Atluri, S.N. (1995) “Dynamic Response of Finite Sized Runway Subjected to Moving Loads: a Coupled BEM/FEM Method,” *International Journal for Numerical Methods in Engineering*, Vol. 38, No. 18, pp. 3143-3166.

Papagiannakis, A.T., Amoah, N., and Taha, R. (1996) “Formulation for Viscoelastic Response of Pavements Under Moving Dynamic Loads,” *Journal of Transportation Engineering*, Vol. 122, No. 2, ASCE, pp. 140-145.

Park, D, Fernando, E. and Leidy, J. (2005) “Evaluation of Predicted Pavement Response with Measured Tire Contact Stresses,” *Transportation Research Record*, No. 1919, TRB, Washington, D.C., pp 160-170.

Park, S.W. and Kim, Y.R. (1999) “Interconversion between Relaxation Modulus and Creep Compliance for Viscoelastic Solids,” *Journal of Materials in Civil Engineering*, Vol. 11, No. 1, ASCE, pp. 76-82.

Park, S.W. and Lytton, R.L. (2004) “Effect of Stress-Dependent Modulus and Poisson's Ratio on Structural Responses in Thin Asphalt Pavements,” *Journal of Transportation Engineering*, Vol. 130, No. 3, ASCE, pp. 387-394.

Pierre, P., Dore, G. and Vagile, L. (2003) *Characterization and Evaluation of Tire-Roadway Interface Stresses*, GCT-03-03, Ministry of Transport, University of Laval, Quebec, Canada.

Pottinger, M.G. (1992) “Three-Dimensional Contact Patch Stress Field of Solid and Pneumatic Tires,” *Tire Science and Technology*, Vol. 20, No. 1, pp. 3-32.

Priest, A. and Timm, D. (2006) “Mechanistic Comparison of Wide-Base Single Versus Standard Dual Tire Configurations,” *Transportation Research Record*, No. 1949, TRB, Washington, D.C., pp. 155-163.

Prozzi, J. A. and Luo, R. (2005) “Quantification of the Joint Effect of Wheel Load and Tire Inflation Pressure on Pavement Response,” *Transportation Research Record*, No. 1919, TRB, Washington, D.C., pp. 134-141.

Romanoschi, S.A. and Metcalf, J.B. (2001) “Effects of Interface Condition and Horizontal Wheel Loads on the Life of Flexible Pavement Structures,” *Transportation Research Record*, No. 1778, TRB, Washington D.C., pp. 123-131.

Roque, R., Myers, L. and Ruth, B. (2000) “Evaluating Measured Tire Contact Stresses to Predict Pavement Response and Performance,” *Transportation Research Record*, No. 1716, TRB, Washington, D.C., pp. 73-81.

Roque, R., Zou, J., Kim, Y.R., Baek, C., Thirunavukkarasu, S., Underwood, B.S., Guddati, M.N. (2010) *Top-Down Cracking of Hot-Mix Asphalt Layers: Models for Initiation and Propagation*, NCHRP Project 1-42A Report, TRB, Washington, D.C.

Saad, B., Mitri, H., and Poorooshasb, H. (2005) “Three-Dimensional Dynamic Analysis of Flexible Conventional Pavement Foundation,” *Journal of Transportation Engineering*, Vol. 131, No. 6, ASCE, pp. 460-469.

Schwartz, C.W. (2002) “Effect of Stress-dependent Base Layer on the Superposition of Flexible Pavement Solutions,” *International Journal Geomechanics*, ASCE, Vol.2, No.3, pp.331-352.

Seyhan, U., Tutumluer, E., and Yesilyurt, H. (2005) “Anisotropic Aggregate Base Inputs for Mechanistic Pavement Analysis Considering Effects of Moving Wheel Loads,” *Journal of Materials in Civil Engineering*, Vol. 17, No. 5, pp. 505-512.

Shen, W. and Kirkner, D.J. (2001) “Non-Linear Finite-Element Analysis to Predict Permanent Deformations in Pavement Structures under Moving Loads,” *International Journal of Pavement Engineering*, 2(3), pp. 187-199.

Shen, S. and Carpenter, S.H. (2007) “Development of an Asphalt Fatigue Model Based on Energy Principles,” *Journal of the Association of Asphalt Paving Technologists*, Vol. 76, AAPT, pp. 525-573.

Shoop, S.A. (2001) *Finite Element Modeling of Tire-Terrain Interaction*, Ph.D. Dissertation, University of Michigan, Ann Arbor, MI.

Siddharthan, R.V., Krishnamenon, N., El-Mously, M., and Sebaaly, P.E. (2002) “Investigation of Tire Contact Stress Distributions on Pavement Response,” *Journal of Transportation Engineering*, vol. 128, no. 2, ASCE, pp. 136-144.

Siddharthan, R.V., Yao, J., and Sebaaly, P.E. (1998) “Pavement Strain from Moving Dynamic 3D Load Distribution,” *Journal of Transportation Engineering*, Vol. 124, No. 6, ASCE, pp. 557-566.

Song, J. and Pellinen, T. (2007) “Dilation Behavior of Hot Mix Asphalt Under Triaxial Loading-A Mechanism of Permanent Deformation Generation,” *International Journal of Road Materials and Pavement Design*, Vol. 8, No. 1, pp. 103-125.

Soon, S.C., Drescher, A., and Stolarski, H. (2003) “Tire-induced Surface Stresses in Flexible Pavement,” *Transportation Research Record*, No. 1896, TRB, Washington, D.C., pp. 170-176.

Sousa, J.B., Lysmer, J., Chen, S.S., and Monismith, C.L. (1988) “Effects of Dynamic Loads on Performance of Asphalt Concrete Pavements,” *Transportation Research Record*, No. 1207, TRB, Washington, D.C., pp. 145-168.

Sousa J.B., Pais, J.C., Way, G.B. (2005) “A Mechanistic-Empirical Based Overlay Design Method for Reflective Cracking,” *Road Material and Pavement Design*, Vol. 6, No. 3, pp. 339-363.

Svasdisant, T., Schorsch, M., Baladi G.Y., and Pinyosunun, S. (2002) “Mechanistic Analysis of Top-Down Cracks in Asphalt Pavements,” *Transportation Research Record*, No. 1809, TRB, Washington, D.C., pp. 126-136.

Tan, S.A., Low, B.H., and Fwa, T.F. (1994) “Behavior of Asphalt Concrete Mixtures in Triaxial Compression,” *Journal of Testing and Evaluation*, ASTM, Vol. 22, No. 3, pp. 195-203.

Tielking, J.T. and Roberts, F.L. (1987) “Tire Contact Pressure and Its Effect on Pavement Strain,” *Journal of Transportation Engineering*, Vol. 113, No. 1, ASCE, pp. 56-71.

Tielking, J.T., and Abraham, M.A. (1994) "Measurement of Truck Tire Footprint Pressures," *Transportation Research Record,* No. 1435, TRB, Washington, D.C., pp. 92-99.

Theyse, H.L., De Beer, M., Rust, F.C. (1996) "Overview of the South African Mechanistic Pavement Design Analysis Method," *Transportation Research Record*, No. 1539, TRB, Washington, D.C. pp. 6-17.

Thom, N.H. (2003) *How Long Does a Long-Life Pavement Last*, Technical Report NCPE 03/1, University of Nottingham, Nottingham, UK.

Thompson, M.R. and Elliott, R.P. (1985) "ILLI_PAVE-Based Response Algorithms for Design of Conventional Flexible Pavements," *Transportation Research Record,* No. 1043, TRB, Washington, D.C. pp. 50-57.

Thompson, M.R., and Robnett, Q.L (1979) "Resilient Properties of Subgrade Soils," *Journal of Transportation Engineering*, ASCE, Vol.105, No.1, pp. 71-89.

Thompson, M.R., Gomez-Ramirez, E.G., and Roginski, M. (2006) "Concepts for Developing a Mechanistic-Empirical Based ACN Procedure for New Generation Aircraft," *Proceeding of 10th International Conference on Asphalt Pavement*, Quebec, Canada.

Tutumluer, E. (1995) *Predicting Behavior of Flexible Pavements with Granular Bases*, Ph.D. Dissertation, Georgia Institute of Technology, Atlanta, GA.

Tutumluer, E., and Thompson, M.R. (1997) "Anisotropic Modeling of Granular Bases in Flexible Pavements," *Transportation Research Record,* No. 1577, TRB, Washington, D.C., pp. 18-26.

Tutumluer, E., and Seyhan, U. (1999) "Laboratory Determination of Anisotropic Aggregate Resilient Moduli Using an Innovative Test Device," *Transportation Research Record,* No. 1687, TRB, Washington, D.C., pp. 13-21.

Tutumluer, E., Little, D.N.. and Kim, S.H. (2003) "Validated Model for Predicting Field Performance of Aggregate Base Courses," *Transportation Research Record,* No.

1837, TRB, Washington, D.C., 2003, pp. 41-49.

Tutumluer, E., (2008) “State of the Art: Anisotropic Characterization of Unbound Aggregate Layers in Flexible Pavements,” Pavements and Materials: Modeling, Testing, and Performance (GSP 184): *Proceedings of the Symposium on Pavement Mechanics and Materials*, ASCE, Minneapolis, MN, pp. 1-16.

Uddin, W., Zhang, D., and Fernandez, F. (1994) “Finite Element Simulation of Pavement Discontinuities and Dynamic Load Response,” *Transportation Research Record,* No. 1448, TRB, Washington, D.C., pp. 100-106.

Uddin, W. and Garza, S. (2003) “3D-FE Modeling and Simulation of Airfield Pavements Subjected to FWD Impact Load Pulse and Wheel Loads,” *Proceedings of 2003 Airfield Pavement Specialty Conference*, ASCE, Las Vegas, NV, pp. 304-315.

Uhlmeyer, J.S., Willoughby, K., Pierce, L.M., and Mahoney, J.P. (2000) “Top-Down Cracking in Washington State Asphalt Concrete Wearing Courses,” *Transportation Research Record,* No. 1730, TRB, Washington, D.C., pp. 110-116.

Uzan, J. (1992) “Resilient Characterization of Pavement Materials,” *International Journal for Numerical and Analytical Methods in Geomechanics*, Vol.16, No.6, ASCE, pp. 435-459.

Wang, H. and Al-Qadi, I.L. (2009) “Combined Effect of Moving Wheel Loading and Three-Dimensional Contact Stresses on Perpetual Pavement Responses,” *Transportation Research Record,* No. 2095, TRB, Washington, D.C., pp. 53-61.

Wang, J., Birgisson, B., and Roque, R. (2006) “Effects of Viscoelastic Stress Redistribution on the Cracking Performance of Asphalt Pavements,” *Journal of the Association of Asphalt Paving Technologists,* Vol. 75, AAPT.

Wang, J., Birgisson, B., and Roque, R. (2007) “Windows-Based Top-Down Cracking Design Tool for Florida: Using Energy Ratio Concept,” *Transportation Research Record,* No. 2037, TRB, Washington, D.C. pp 86-96.

Wang, L.B., Myers, L.A., Mohammad, L.N., and Fu, Y.R. (2003) "Micromechanics Study on Top-Down Cracking," *Transportation Research Record*, No. 1853, TRB, Washington, D.C., pp. 121-133.

Weissman, S.L. (1999) "Influence of Tire–Pavement Contact Stress Distribution on Development of Distress Mechanisms in Pavements," *Transportation Research Record*, No. 1655, TRB, Washington, D.C., pp. 161-167.

Wriggers, P. (2002) *Computational Contact Mechanics*, John Wiley & Sons, Hoboken, NJ.

Yang, Y.B. and Hung, H.H. (2001) "A 2.5D Finite/Infinite Element Approach for Modeling Visco-elastic Bodies Subjected to Moving Loads," *International Journal for Numerical Methods in Engineering*, 51(11), pp. 1317-1336.

Yoo, P.J. and Al-Qadi, I.L. (2007) "Effect of Transient Dynamic Loading on Flexible Pavements," *Transportation Research Record*, No. 1990, TRB, Washington, D.C., pp. 129-140.

Yoo, P.J. and Al-Qadi, I.L. (2008) "Truth and Myth of Fatigue Cracking Potential in Hot-Mix Asphalt: Numerical Analysis and Validation," *Journal of Association of Asphalt Paving Technologists*, Vol. 77, AAPT, pp. 549-590.

Zaghloul, S. and White, T. (1993) "Use of a Three-Dimensional Dynamic Finite Element Program for Analysis of Flexible Pavement," *Transportation Research Record*, No. 1388, TRB, Washington, D.C., pp. 60-69.

Zhang, X. (2001) *Nonlinear Finite Element Modeling and Incremental Analysis of A Composite Truck Tire Structure*, Ph.D. Dissertation, Concordia University, Montreal, Canada.

Zhong, X.Z., Zeng, X., and Rose, J.G. (2002) "Shear Modulus and Damping Ratio of Rubber-modified Asphalt Mixes and Unsaturated Subgrade Soils," *Journal of Materials in Civil Engineering*, Vol. 14, No. 6, ASCE, pp. 496-502.

Zienkiewicz, O.C., and Taylor, R.L. (2000) *Finite Element Method*, Butterworth-Heinemann, Oxford, UK.